Title
Interrogation of Neural Circuits of the Basal Forebrain and Midbrain for Sleep-Wake Regulation

Author
Do, Phong H.

Publication Date
2017

Peer reviewed|Thesis/dissertation

Interrogation of Neural Circuits of the Basal Forebrain and Midbrain for Sleep-Wake Regulation

By

Phong H. Do

A dissertation submitted in partial satisfaction of the

requirements for the degree of

Doctor of Philosophy

in

Molecular and Cell Biology

in the

Graduate Division

of the

University of California, Berkeley

Committee in charge:

Professor Yang Dan, Chair
Professor Hillel Adesnik
Professor Ehud Isacoff
Professor Lance Kriegsfeld

Spring 2017

Abstract

Interrogation of Neural Circuits of the Basal Forebrain and Midbrain for Sleep-Wake Regulation

By

Phong H. Do

Doctor of Philosophy in Molecular and Cell Biology

University of California, Berkeley

Professor Yang Dan, Chair

In mammals, sleep is comprised of two distinct stages, rapid eye movement (REM) and non-REM (NREM) sleep. The regulation of the sleep-wake cycle involves many brains regions that influence the probability of each state. Since many brain regions contain a mixed population of wake-promoting and sleep-promoting neurons, it remains a challenge to dissect and interrogate the neural circuits of sleep-wake regulation.

In Chapter 2, I describe the mapping of neural circuits of the basal forebrain (BF) known to regulate wake and NREM sleep. The BF contains a spatially intermingled diverse population of neurons that plays key roles in multiple brain functions, including sleep-wake regulation, attention, and learning/memory. For sleep-wake regulation, the cholinergic, glutamatergic, and parvalbumin-expressing (PV) GABAergic neurons have been shown to promote wakefulness, whereas the somatostatin-expressing (SOM) GABAergic neurons promote NREM sleep. To better understand the functional specialization of these cell types, we performed whole-brain mapping of both inputs and outputs of these four BF cell types in the mouse brain. Using rabies virus-mediated monosynaptic retrograde tracing to label the inputs and adeno-associated virus to trace axonal projections, we identified numerous brain areas connected to the BF. The inputs to different cell types were qualitatively similar, but the output projections showed marked differences. The connections to glutamatergic and SOM+ neurons were strongly reciprocal, while those to cholinergic and PV+ neurons were more unidirectional. These results reveal the long-range wiring diagram of the BF circuit with highly convergent inputs and divergent outputs and point to both functional commonality and specialization of different BF cell types.

In Chapter 3, I describe the interrogation of the midbrain ventrolateral periaqueductal gray (vlPAG), known to be important for gating REM sleep. We demonstrated that activating vlPAG GABAergic neurons in mice suppressed the initiation and maintenance of REM sleep while consolidating NREM sleep, partly through their projection to the dorsolateral pons. Cell-type-specific recording and calcium imaging showed that most vlPAG GABAergic neurons are strongly suppressed at REM sleep onset and activated at its termination. In addition to the rapid changes at brain state transitions, their activity decreases gradually between REM sleep and is reset by each REM episode in a duration-dependent manner, mirroring the accumulation and dissipation of REM sleep pressure. Thus, vlPAG GABAergic neurons powerfully gate REM sleep, and their firing rate modulation may contribute to the ultradian rhythm of REM/NREM alternation.

Dedications

I am grateful to have had the opportunity to pursue a doctorate degree at UC Berkeley. It has been an enlightening experience to partake in the process of science to validate and expand the source of human knowledge. The scientific journey has been challenging but rewarding, and would not have been the same without the following individuals:

Thank you to my thesis advisor, Yang Dan, for generously offering her time and resources to mentor and shape me into a better scientist. Her intelligence, dedication to science, and ability to manage many projects at a high level is admirable and are traits that I aspire to.

Thank you to my thesis committee members: Hillel Adesnik, Ehud Isacoff, and Lance Kriegsfeld, for the valuable feedback, support, and encouragement. It has been a true privilege to interact with such great scientists.

To the past and present members of the Dan lab: thank you for the valuable discussion and support throughout the years. I would especially like to thank my collaborators, Min Xu and Seung-Hee Lee. Thanks to Chenyan Ma, for her generosity and willingness to always help. Thanks to Shinjae Chung for all of the valuable candid advice. Thanks to Julia Cox for teaching me the fundamentals of calcium imaging experiments, and for all of the scientific discussion and non-scientific conversation and support. Special thanks to my neighbor and collaborator, Franz Weber, who I have learned immensely from and who has a great scientific career ahead of him.

My experience would not have been the same without the company of my fellow MCB classmates and the larger neuroscience community at UC Berkeley. Thank you for all of the scientific discussion and for making my experience rewarding and fun. Special thanks to my buddy Dan Bliss, for being a great friend and always keepin' in real.

There are tons of logistics in a graduate program, but I was largely able to focus on the science thanks to the dedicated support of the past and present members of the MCB Graduate Affairs Office, including: Berta Parra, Tanya Sullivan, Mona Su, Sarah Hamilton, and Eric Buhlis.

Most importantly, thank you to my family for always supporting me to follow my dreams. I am incredibly lucky to have you all in my life and would not be where I am without you:

To my brother, you have brought great joy to my life and I am looking forward to sharing more adventures together. To my mother, for all of her love and sacrifice so that I could have a good life. To my sisters, thank you for enriching my life with your presence, compassion, and love, and always making the tough times better. You have all shaped me into a better person.

Thank you to cô Hong for the love, encouragement, and support. I wouldn't have survived the rigorous doctoral program without my father, who taught me the value of

hard-work by embodying his principles. Thank you for your dedication and sacrifice to support me and the family, and for teaching me the fundamentals of how to be a good, respectful person while always remembering the most important things in life.

To the Cheung family, thank you for your constant love and support. To my father-in-law, Benny Cheung, your spirit is alive in our memories, in our words, and in our actions. To my fiancée, Samantha, it has been an incredible journey with you. Thank you for 2am science discussions, for always giving me the confidence that I can achieve anything I set my mind to, and for always being by my side through both the good and the tough times. I'm looking forward to our future together.

Acknowledgements

The work of Chapter 2, "Cell type-specific long range connections of basal forebrain circuit", would not have been possible without the collaboration with the following individuals:

Authors: Johnny Phong Do[+], Min Xu[+], Seung-Hee Lee[+], Wei-Cheng Chang, Siyu Zhang, Shinjae Chung, Tyler J. Yung, Jiang Lan Fan, Kazunari Miyamichi, Liqun Luo, and Yang Dan ([+] These authors contributed equally to this work)

Author Contributions: J.D., M.X., and S.-H. L. conceived and designed the experiments and analyses. J.D., M.X., S.-H. L., W.-C. C., S.C., S.Z., T.J. Y., and J.L.F. performed the experiments. M.X. wrote the software for data analyses, K.M. and L.L. provided crucial reagents and technical assistance for RV production. J.D., M.X., S.-H. L., and Y.D. wrote the manuscript.

Additional Acknowledgements: We thank Kai-Siang Chen, T. Lei, D. Jeong for the help with histological processing and data analysis, and B. Lim and E. Callaway for viral vectors and cell lines.

The work of Chapter 3, "Regulation of REM & Non-REM sleep by periaqueductal GABAergic neurons", would not have been possible without the collaboration with the following individuals:

Authors: Franz Weber [+], Johnny Phong Hoang Do[+], Shinjae Chung, Kevin T. Beier, Mohammad S. Doost, Mike Bikov, Yang Dan ([+] These authors contributed equally to this work)

Author Contributions: F.W, J.P.H.D, and Y.D. conceived and designed the experiments. F.W. and J.P.H.D. performed optogenetic activation experiments. F.W. performed optrode recordings and pro-Caspase 3-mediated lesion experiments. J.P.H.D. performed calcium imaging experiments and trans-synaptic viral tracing. S.C. performed in situ hybridization and fluorescence microscopy. M.B. performed histology and immunohistochemistry experiments. K.T.B. provided viral reagents for rabies-mediated trans-synaptic experiments. F.W. and J.P.H.P. analyzed the data. F.W, J.P.H.D, and Y.D. wrote the manuscript.

Additional Acknowledgements: We thank Zhe Zhang, Nikolai Hörmann, and Andrei Popescu for technical help. We are grateful to Liqun Luo for providing viral reagents for trans-synaptic tracing. This work was supported by a Human Frontier Science Program (HFSP) postdoctoral fellowship (to. F.W.).

TABLE OF CONTENTS

CHAPTER 1
Introduction

Introduction

The Importance of Sleep

Sleep is an essential biological process that has been observed in wide range of animals such fruit flies, birds, reptiles, and mammals[1,2]. The importance of sleep is evident by observing the effects of sleep deprivation, which causes cognitive impairments that decrease alertness and reaction time[3,4], impair information processing and problem-solving[5,6], and negatively influence mood and stress[7,8]. As a result, acute sleep deprivation significantly increases the risk of work-related and motor vehicle-related accidents[9]. Longer-term or chronic sleep deprivation can result in serious disruptions to metabolism, increasing the risk of diabetes and cardiovascular disease[10,11], is associated with mental health conditions[12], and can even lead to death[13]. While the biological changes that occur during sleep are not fully understood, research has identified some crucial roles of the sleep process for maintaining the physical and mental health of animals, including promoting the clearing of biological waste products from the cerebrospinal fluid (CSF)[14], changes in brain plasticity associated with learning and mental health[6,15,16], and an influence on immune function[17,18]. Given the fundamental role of sleep in the life of an animal, it remains an important task to understand how the dynamic process of sleep itself is regulated in the brain.

Measurements of Sleep States

The process of behavioral sleep involves sustained periods of complete immobility that is accompanied by a reversible, reduced response to external stimuli[2]. In mammals and reptiles, two distinct stages of sleep called non-rapid eye movement (NREM) and rapid eye movement (REM) sleep can be distinguished using a measure of brain activity called electroencephalogram (EEG) recordings and a measure of muscle tone called electromyogram (EMG)[19,20] recordings. Wakefulness is characterized by low amplitude and high frequency activity in the EEG and high muscle tone, NREM is characterized by high amplitude and low frequency (0.5–4.5 Hz) activity in the EEG and lower muscle tone, while REM sleep is characterized by low amplitude and high frequency activity in the EEG that resembles the wake state, with very prominent theta oscillations in rodents, and a paralysis of postural muscles called muscle atonia.

NREM Sleep Regulation

Sleep is not simply a passive process where the brain shuts down in environments with low sensory stimulation, but rather it involves the active engagement of distinct neural circuits in the brain. The preoptic area of the forebrain plays an important role in the regulation of NREM sleep based on evidence from human patients with damage to the preoptic area, and from targeted lesions in experimental rodents, both revealing a difficulty or inability to sleep called insomnia[21,22]. Such lesion experiments are similar to genetic loss-of-function experiments, where the damage to a brain region that might promote a particular behavioral phenotype results in a decrease or absence of that phenotype. A subregion of the preoptic area has been implicated in sleep regulation; c-fos immunostaining following sleep episodes identified a population of sleep-active neurons in the ventrolateral preoptic area (VLPO)[23], and their role in promoting sleep is supported by lesion experiments that impair sleep[3]. GABAergic VLPO neurons projects to a wide range of wake-promoting neurons such as the histaminergic tuberomammillary nucleus

(TMN), the noradrenergic locus coeruleus (LC), the serotonergic dorsal raphe (DR) and median raphe (MR), and the orexin neurons in the hypothalamus, and the inhibition of these regions may be a mechanism to promote sleep[24]. Microdialysis measurements in the wake-promoting LC, DR, and the posterior hypothalamus, reveal an elevated extracellular GABA concentration during sleep, suggesting that the source of the GABA may the inhibitory projections from the VLPO sleep-active neurons[25,26]. In addition, many of these wake-promoting neurons also project to the preoptic area, supporting the "flip-flop" model between sleep and wake states, where transitions are regulated by reciprocal inhibition between wake and sleep-promoting brain regions[27,28].

Brain regions outside of the hypothalamus have also been identified to regulate NREM sleep. Neurons in the parafacial zone (PZ), located dorsolateral to the facial nucleus in the medulla are mostly sleep-active[29], and chemogenetic activation of the vesicular GABA transporter-expressing (VGAT) inhibitory neurons promoted NREM sleep[30]. In contrast, impairing inhibitory neurotransmission by deleting the VGAT gene or by lesioning the PZ, increased wakefulness. Neuronal population in the midbrain have also been found to regulate NREM sleep; either the optogenetic or chemogenetic activation of inhibitory neurons in the vlPAG[31], the adjacent deep mesencephalic reticular nucleus (DpMe), or developmentally labeled glutamatergic neurons in the region of the dorsolateral pons, promote NREM sleep[32].

REM Sleep Regulation

Distinct neural circuits have also been identified in the regulation of REM sleep. Pharmacological activation of the dorsolateral pons induced a REM-like activity in the EEG and EMG[33]. In contrast, loss-of-function of the dorsolateral pons by lesion decreased REM sleep frequency, and knockdown of VGLUT caused REM sleep fragmentation[34,35]. Calcium imaging experiments revealed that the majority of glutamatergic neurons in the dorsolateral pons are most active during REM, whereas the majority of GABAergic neurons are most active during wake[36]. Together, these experiments support the notion that the REM-active glutamatergic neurons in the dorsolateral pons are important in REM sleep regulation.

Early transection studies suggested that the brainstem also plays a critical role in REM sleep generation[37]. cfos immunohistochemistry has revealed a population of REM-active neurons in the medulla[38]. Recent studies demonstrated that the optogenetic activation of the GABAergic neurons in the ventral medulla strongly promoted the initiation of REM sleep from NREM sleep, and the maintenance of REM sleep[31]. Consistent with their role in initiating REM sleep, these GABAergic neurons also increase their firing rate before the onset of REM sleep.

A few other brain regions have been further identified to influence REM sleep, including the initiation and maintenance of REM sleep by MCH neurons in the lateral hypothalamus[39,40], and initiation of REM sleep by the cholinergic neurons in the LDT/PPT[41].

The Regulation of Wake States

Transections of the brains of cats at the mid-collicular level resulted in sleep-like behavior and activity recorded in the EEG[42]. The existence of both sleep and wake states did not

seem to be dependent on input from the spinal cord because transection at the level of the brainstem and spinal cord did not disrupt the sleep-wake alternation. Together, these experiments suggested the existence of a brain region between the spinal cord and collicular region that played a strong role in arousal. Subsequent electrical stimulation experiments in anesthetized animal identified a wake-promoting brain area residing in the midbrain reticular nucleus that led to the concept of the ascending arousal system, a network of fibers from the brainstem with dense rostral projections that promote arousal[43].

The ARAS has further been divided into an ascending and descending pathway. The ascending pathway includes regions of the midbrain, pontine, medullary reticular formation, PPT/LDT, and has dense projections to the thalamocortical system. The ventral pathway includes the fibers from the medial forebrain bundle with ascending projections from the brain stem parabrachial neurons, noradrenergic LC, serotonergic DR/MR, and dopaminergic PAG neurons. These neurons innervate the glutamatergic, histaminergic, and orexinergic neurons of the posterior and lateral hypothalamus, the cholinergic, glutamatergic, and GABAergic neurons of the basal forebrain[20].

The wake-promoting effects of some of these neuronal populations in the ARAS pathway have been supported by optogenetic manipulations. Tonic 3 Hz or phasic 10 Hz optogenetic stimulation of LC neurons, or chemogenetic activation of VGAT+ neurons in the lateral hypothalamus promoted behavioral arousal[44,45]. In contrast, the suppression of these neurons decreased the percentage of time spent in wakefulness, with a concomitant increase in NREM sleep. These results also support the notion that the inhibition of these neurons may be a natural mechanism in the brain to promote sleep, and GABAergic sleep-active neurons, such as those from the preoptic area, may play such a role in antagonizing the wake-promoting neurons to encourage a state transition.

Homeostatic and Circadian Regulation of Sleep-Wake

An important challenge remains to understand how these brain regions interact to regulate the switching between brain states. Circadian influence on sleep promotes a ~24 hour sleep-wake cycle that is entrained by light in which diurnal animals like humans sleep primarily during the nighttime and nocturnal animals such as mice to sleep more during the daytime[46]. The circadian influence on daily sleep-wake rhythm is critically dependent on the suprachiasmatic nucleus (SCN) of the hypothalamus, the master pacemaker[47,48]. However, lesion of the SCN eliminates the daily rhythm of sleep but does not have significant effect on the duration of sleep, suggesting that other homeostatic sleep pressures play a role in the alternation between sleep and wake[49,50].

Chemical homoeostatic factors, also called somnogens, are molecules that may accumulate during wakefulness to promote sleep after prolonged wakefulness. Evidence for the existence of somnogens come from studies in the early 1900s demonstrating that CSF from a sleep-deprived dog transfused into a non-sleep deprived dog triggered sleep behavior[51,52]. Some of the identified molecules that have characteristics of somnogens include adenosine, prostaglandin D2, nitric oxide, GHRH, and other cytokines[20]. Adenosine, which is well-known for having its adenosine receptors inhibited by caffeine, has been a strong candidate in the regulation of sleep

homeostasis[53]; adenosine increases concentration during wake in both the basal forebrain and cortex, suggesting that it may increase sleep pressure with prolonged wakefulness, and conversely decreases in concentration during sleep, suggesting a dissipation in the pressure to sleep when sleep occurs[54,55]. Furthermore, injection of adenosine into the wake-promoting TMN or the LDT has been demonstrated to promote NREM sleep[56,57].

Changes in the ionic composition of the cerebrospinal fluid may also act as a homoeostatic factor for sleep pressure. Prolonged wakefulness was associated with AMPA receptor-independent elevations of extracellular [K+], and decreases in extracellular [Ca2+], [Mg2+], [H+][58]. These changes were reversed during sleep or anesthesia, which may reflect a dissipation of sleep pressure with the occurrence of sleep. In addition, infusing an artificial CSF cocktail either mimicking the ionic composition during the sleep or wake state into the cisterna magna was sufficient to cause the respective behavioral state measured by EEG and EMG.

Dissecting the Intermingled Neuronal Populations of the Basal Forebrain

The basal forebrain receives input from the ascending reticular activating system and is well-known to contain populations of cholinergic neurons that regulate arousal in addition to having more well-defined specialized function related to attention, cortical processing, learning, and plasticity[59–64]. However, the basal forebrain also contains a diverse population of spatially intermingled neurons, including cholinergic neurons, glutamatergic, and PV+ GABAergic neurons that are more active during REM and wake states, and promote wakefulness when optogenetically activated[65]. In contrast, the SOM+ GABAergic population consists of a majority of neurons more active during NREM, and their optogenetic activation promotes NREM sleep. Locally, ChR2-assisted circuit mapping brain slices revealed that SOM+ GABAergic neurons inhibit all wake-promoting neuronal identities, including the glutamatergic, cholinergic, and PV+ GABAergic BF neurons, which may mediate its sleep-promoting effect.

It interesting to consider how does each cell-type in the intermingled population of neurons differently contribute to sleep-wake regulation. Neurons in the same brain region may have unique functional roles based on their how they are differently influenced by neuromodulators/neuropeptides, paracrine factors, and neurotransmitters based on their expressed receptors, and their intrinsic physiological properties such as resting membrane potential that influences their excitability. In addition to these molecular properties, it is important to examine any potential differences in projection pattern and the brain regions that provide input to the neurons. While the local connections have been examined, the long-range inputs and outputs of each cell-type have not been comprehensively examined.

In Chapter 2, I describe the comprehensive mapping of the input and output of these four genetically defined cell types in the basal forebrain: glutamatergic, cholinergic, PV+ GABAergic, and SOM+ GABAergic neurons, to better understand anatomical specialization among these cell types.

Diversity of periaqueductal gray (PAG) neurons

The vlPAG is one of the inputs the basal forebrain. Electrical and chemical activation, and lesion experiments of subregions around that PAG have identified subregions that are associated with different behavioral functions, including innate and conditioned freezing, defensive behaviors, pain modulation, and sleep[31,66,67]. These different subregions around the PAG have been shown to have distinct projections patterns that may mediate different functions[68]. While the dorsolateral region has been implicated in defensive-like behaviors, such as howling/hissing or flight behavior, the ventrolateral region is associated with decreases in movement or freezing behavior[69]. More recent studies have implicated a role of the vlPAG in the regulation of both REM and NREM sleep, suggesting that it may play a role in the ultradian alternation between NREM and REM sleep[31]. Given the diversity of identified functions of the vlPAG, it is interesting to consider whether these neurons play multi-faceted roles to promote physiological changes that are common to different behavioral functions. For example, there is evidence that the vlPAG plays a role in both nociception and in sleep. Is the decrease in the threshold to pain sensation from nociception a similar neural mechanism to the decrease in responsiveness to external stimuli during sleep? Seemingly unrelated overlap have been observed for other sleep related neurons, such as the GABAergic neurons of the ventral medulla, whose activation during NREM can strongly initiate and maintain REM sleep, but whose activation during wake promotes feeding behavior[31].

Regulation of REM and NREM Sleep by GABAergic vlPAG neurons

During the sleep phase, there exists an alternation between NREM and REM sleep that lasts ~90-120 min in humans[70]. In rodents the alternation is much shorter, at ~10-20 min[70]. Such regular alternation suggests that there may be some kind of ultradian homeostatic mechanisms that operate at a timescale of less than 24 hours to regulate the NREM/REM alternation during sleep. Examining the reciprocal inhibitory interactions, or antagonism, between REM and NREM-promoting neurons may be the key to understanding the neural circuits that modulate the homeostasis of NREM/REM alternation.

The vlPAG is a one candidate region to modulate NREM/REM alternation because anatomical studies have suggested that the vlPAG receives and sends input to REM-promoting regions[34,71]. In addition, optogenetic studies have demonstrated that the activity of the GABAergic vlPAG neurons can both suppress REM sleep, and promote NREM sleep[31].

In Chapter 3, I describe a series of experiments taking advantages of recently developed tools in neuroscience to specifically manipulate the GABAergic vlPAG neurons or their projections across the sleep-wake cycle, and record their physiological activity during the sleep-wake cycle to elucidate the role of the vlPAG in modulating the rapid transitions between brains states, and its relation to sleep pressure associated with NREM/REM alternation.

CHAPTER 2:

Cell type-specific long range connections of basal forebrain circuit

Summary

The basal forebrain (BF) plays key roles in multiple brain functions, including sleep-wake regulation, attention, and learning/memory, but the long-range connections mediating these functions remain poorly characterized. Here we performed whole-brain mapping of both inputs and outputs of four BF cell types – cholinergic, glutamatergic, and parvalbumin-positive (PV+) and somatostatin-positive (SOM+) GABAergic neurons – in the mouse brain. Using rabies virus -mediated monosynaptic retrograde tracing to label the inputs and adeno-associated virus to trace axonal projections, we identified numerous brain areas connected to the BF. The inputs to different cell types were qualitatively similar, but the output projections showed marked differences. The connections to glutamatergic and SOM+ neurons were strongly reciprocal, while those to cholinergic and PV+ neurons were more unidirectional. These results reveal the long-range wiring diagram of the BF circuit with highly convergent inputs and divergent outputs and point to both functional commonality and specialization of different BF cell types.

Introduction

The BF has been implicated in a variety of brain functions such as arousal, attention, and plasticity[28,59–61,63,72–74]. The dysfunction or loss of BF cholinergic neurons is an important feature of Alzheimer's disease associated with cognitive impairment[75,76]. In addition to forming extensive local synapses[65,77,78], BF neurons receive inputs[79–87] and send outputs[88–92] to many other brain areas[93,94]. However, how these long-range connections contribute to BF functions remains unclear.

An important challenge in understanding the function of the BF circuit is its neuronal heterogeneity. There are three major cell types spatially intermingled in the BF: cholinergic, glutamatergic, and GABAergic[94,95]. Selective lesion or pharmacological manipulation of the cholinergic system is well known to affect multiple brain functions[96]. For example, 192-IgG-saporin-mediated lesion of cholinergic neurons impaired the ability of rats to discriminate between signal and non-signal visual events in an attention task[97] and disrupted training-induced cortical map reorganization associated with motor learning [98]. Glutamatergic and GABAergic BF neurons are also likely to serve important functions[74]. For example, in recent studies the activity of non-cholinergic BF neurons was found to correlate with sustained attention[99] or to encode reward and motivational salience information[100–102], and optogenetic activation of PV+ GABAergic neurons was shown to regulate cortical gamma oscillations[103]. In a study on sleep-wake control, cholinergic, glutamatergic, and PV+ neuron activity was found to promote wakefulness, while SOM+ neurons promoted sleep; these four cell types form extensive but highly specific local connections with each other for brain-state regulation[65]. Thus, to understand the BF circuit function it is crucial to map its inputs and outputs with cell-type specificity.

Most of the previous studies of BF long-range connections focused on specific regions connected to the BF, making it difficult to assess their whole-brain distribution. Recent advances in virus-assisted circuit tracing[104,105] and high-throughput imaging have greatly facilitated whole-brain mapping of long-range connectivity in a cell-type-specific manner[106,107]. In this study, we traced the long-range inputs and outputs of four genetically defined BF cell types. While the input distributions were similar across cell types, their output patterns showed striking differences. Our quantitative analysis of the whole-brain distributions of inputs and outputs for each BF cell type can serve as an anatomical blueprint for future studies of inter-regional pathways mediating BF functions.

Results

Four Cre mouse lines were used to target different BF subpopulations for virus-mediated circuit tracing: choline acetyltransferase (ChAT)-Cre for cholinergic neurons, vesicular glutamate transporter 2 (VGLUT2)-Cre for glutamatergic neurons, and PV-Cre and SOM-Cre mice for two subtypes of GABAergic neurons. These four Cre lines have been shown to label largely non-overlapping BF neuron populations with high-specificity[65].

To identify the long-range inputs to each cell type, we used RV-mediated transsynaptic retrograde tracing, which has been shown to label monosynaptic inputs to selected starter cells with high specificity[108–111]. First, we expressed avian-specific retroviral receptor (TVA), enhanced green fluorescent protein (eGFP), and rabies glycoprotein (RG) specifically in each cell type by injecting two Cre-inducible AAV vectors (AAV2-EF1α-FLEX-eGFP-2a-TVA and AAV2-EF1α-FLEX-RG) into the BF of ChAT-, VGLUT2-, PV-, or SOM-Cre mice (Figure 1A). The expression of RG was highly cell type specific and not detected in wild-type mice not expressing Cre recombinase (Figure 1 – figure supplement 1). Two to three weeks later, we injected a modified RV (rabiesΔG-tdTomato+EnvA) that only infects cells expressing TVA, requires RG to spread retrogradely to presynaptic cells (Figure 1 – figure supplement 2), and contains the tdTomato transgene. After histological sectioning and fluorescence imaging, each sample was aligned to a reference atlas (Allen Mouse Brain Atlas, see Materials and Methods) to facilitate 3D whole-brain visualization and quantitative comparison across brain samples (Figure 1C). The starter cells (expressing both tdTomato and eGFP) and the transsynaptically labeled presynaptic neurons (expressing tdTomato only) were identified manually, and their locations were registered in the reference atlas (Figure 1 – figure supplement 3).

Brain samples were excluded from the analyses if very few input neurons (<200) were labeled in the whole brain. As noted in previous studies, due to the extremely efficient interaction between TVA and EnvA-pseudotyped rabies virus, the very low-level expression of TVA in non-Cre-expressing cells (not detectable based on fluorescent protein markers) allows the rabies virus to infect and label these cells with tdTomato at the injection site, independent of synaptic connections with starter cells[109,110,112–115]. However, this local contamination does not compromise the mapping of long-range inputs because RG (required for transsynaptic spread of RV) is not expressed in any non-Cre-expressing cells at sufficient levels for trans-complementation of rabiesΔG to allow transsynaptic spread of RV[104,113]. To determine the spatial extent of the local contamination, we performed control experiments in the absence of RG and found very few non-specific labeling at >850 μm from the injection center (Figure 1 – figure supplement 2D). Thus, presynaptic neurons were counted only in coronal sections outside of this range. While this procedure precludes identification of local inputs, synaptic interactions of the four cell types within the BF have been characterized electrophysiologically in a recent study[65]. Another technical limitation of the study is that when the brain was removed for histological processing, the olfactory bulb was often damaged, which led to a significant underestimation of labeling (both the input neurons and axon projections) in the olfactory bulb.

We found 900 – 14,631 (median 7002) tdTomato-labeled presynaptic neurons in each brain (n = 17), and the convergence index (ratio between the number of input cells and starter cells) ranged between 4.3 and 77.7 (Figure 1– figure supplement 4). Such variability is comparable to that

found in other studies using similar methods[116,117]. The presynaptic neurons were predominantly ipsilateral to the starter population (<5% contralateral) but were distributed in a large number of brain areas (Figure 2, Figure 3, Video 1). Since the number of labeled neurons varied across brain samples, and there was no significant difference among the four cell types ($P = 0.27$, one-way ANOVA), we normalized the data in each area by the total number of labeled neurons in each brain. When the brain was divided into 12 major regions (Figure 3A), the striatum and hypothalamus provided the highest numbers of inputs, while few labeled neurons were found in the medulla or cerebellum (Figure 3A).

To facilitate data visualization at different levels of detail, we also used an interactive sunburst diagram (adapted from Allen Mouse Brain Atlas, http://www.brain-map.org/api/examples/examples/sunburst/) to represent the whole-brain distribution of inputs to each cell type (http://sleepcircuits.org/bf/). The brain structures are arranged hierarchically from inner to outer circles, and the size of each sector represents the percentage of input from the corresponding structure. The name of each structure and its input percentage can be read out by pointing the cursor, and each region of interest can be expanded with a mouse click.

When the input distribution was analyzed at a finer spatial scale (e.g., the 6th ring of the sunburst plot), the nucleus accumbens[87,92], lateral hypothalamus[89,92,118], and central nucleus of the amygdala[89,91] were among the structures containing the highest numbers of input neurons (Figure 2). Interestingly, many close neighbors of these densely labeled structures (e.g., the basolateral nucleus of the amygdala, immediately adjacent to the central nucleus) showed very sparse or no labeling, indicating high spatial specificity of the long-range inputs. On the other hand, the input distributions were qualitatively similar among cell types, although with quantitative differences. For example, glutamatergic neurons received significantly more inputs from the lateral hypothalamus than the other cell types (P = 0.001, VGLUT2 vs. ChAT; P = 0.001, VGLUT2 vs. PV; P = 0.001, VGLUT2 vs. SOM;, one-way ANOVA and post-hoc Tukey's test), and PV+ neurons received more inputs from the nucleus accumbens (ACB) (P = 0.004, PV vs. ChAT; P = 0.003, PV vs. VGLUT2; P = 0.001, PV vs. SOM; one-way ANOVA and post-hoc Tukey's test).

To further verify the inputs revealed by RV-mediated retrograde tracing, we optogenetically tested the synaptic connections from the prefrontal cortex (PFC) and ACB (Figure 4). To verify the innervation from PFC to BF cholinergic neurons, we injected AAV (AAV-DJ-CaMKIIα-hChR2-eYFP) expressing the mammalian codon-optimized channelrhodopsin-2 (hChR2) fused with enhanced yellow fluorescent protein (eYFP) in the orbital and agranular insular areas of the PFC (Figure 4 – figure supplement 1) in ChAT-eGFP mice and made whole-cell voltage-clamp recordings from eGFP-labeled cholinergic neurons in acute BF slices (Figure 4A). Activating the ChR2-expressing axon terminals with blue light evoked excitatory responses in all recorded BF cholinergic neurons ($n = 9$, Figure 4B and 4C), confirming the input revealed with RV tracing. To confirm the innervation from ACB, we injected Cre-inducible AAV (AAV-DJ-EF1α-FLEX-ChR2-eYFP) expressing ChR2-eYFP in ACB of GAD2-Cre mice, made whole-cell current-clamp recordings from unlabeled postsynaptic BF neurons, and used single cell reverse-transcription PCR (RT-PCR) to identify the cell type. We found that all four BF cell types received inhibitory responses from the ACB (Figure 4D and 4E; ChAT+: 2 out 5 showed significant responses; VGLUT2+: 2/4; PV+: 3/3; SOM+: 4/8), which is consistent with the finding of an electron microscopic double-immunolabeling study performed in rats[87].

We next mapped the output of each BF cell type. To label the axonal projections, we injected AAV with Cre-dependent expression of mCherry (Figure 1B) into the BF of ChAT-, VGLUT2-, PV- or SOM-Cre mice. Two to three weeks after injection, the brain tissues were processed, images were registered to the reference atlas, and labeled axons were detected (Figure 1C, see Materials and Methods). After the injection site (identified by the existence of labeled cell bodies) and locations with known major fiber tracks were excluded, the projection to each brain area was quantified by the number of pixels occupied by the detected axons[106] (see Materials and Methods).

Parallel to the broad distribution of inputs (Figure 3), we found that each BF cell type also projected to a large number of brain areas (Figure 5, Figure 6, Video 2, http://sleepcircuits.org/bf/, >95% ipsilateral). Among the 12 major brain subdivisions (Figure 6A), the hypothalamus, pallidum, and striatum received the heaviest BF projections[81,82], while very few axons were detected in the medulla or cerebellum (Figure 6A). Analysis at finer scales revealed high spatial specificity of the projections. For example, while several cell types projected strongly to the lateral habenula (Figure 5), few axons were detected in the immediately adjacent but anatomically distinct medial habenula[119]. In addition to providing extensive inputs to the BF (Figure 2), the lateral hypothalamus was also a major recipient of BF projections (Figure 5), indicating a strong BF-hypothalamus loop that may be important for brain-state regulation[20,28,63]. Importantly, whereas the input distributions were generally similar across BF cell types (Figure 2, Figure 3), the output patterns showed striking differences. For example, compared to the other cell types, the projection from cholinergic neurons was much stronger in the basolateral amygdala, hippocampus, and visual cortex but much weaker in the lateral hypothalamus, lateral habenula, and the ventral tegmental area (Figure 5). The different projection patterns among cell types are also apparent in the 3D whole-brain view (Figure 6B, Figure 6 – source data 1).

To further compare the inputs and outputs among cell types, we averaged the spatial distributions across brain samples of each cell type and computed the correlation coefficient (CC) between cell types. For input distribution, the CCs between all cell types were high (Figure 7A), confirming their overall similarity observed earlier (Figure 2, Figure 3). On the other hand, when we computed the CCs between individual brain samples, we found higher CCs between samples of the same cell type (0.81 ± 0.04, s.e.m.) than of different cell types (0.70 ± 0.02, $P = 0.01$, *t*-test; Figure 7 – figure supplement 1A). This indicates that despite the overall similarity, there were genuine differences among cell types that were beyond experimental variability.

For output distribution, the CCs between individual samples of the same cell type were also high (0.86 ± 0.05; Figure 7 – figure supplement 1B), indicating reproducibility of the mapping. However, most of the CCs between cell types (Figure 7B, computed after averaging across samples of the same cell type) were much lower than those for input distribution. The two lowest CCs (ChAT+ vs. VGLUT2+ and PV+ neurons) reflect the fact that while the cholinergic neurons project strongly to structures within the cerebral cortex (including olfactory areas, isocortex, hippocampus, and cortical subplate) and weakly to the brain stem structures (thalamus, hypothalamus, and midbrain), glutamatergic and PV+ neurons (with output distributions highly similar to each other) showed complementary projection patterns (Figure 6).

Finally, we computed the CC between the input and output distributions of each cell type (Figure 7C). The highest CC was found for SOM+ neurons, reflecting their strong reciprocal connections with a number of brain structures, including the hypothalamus, striatum, pallidum, and olfactory areas (Figure 7D, lower right, Figure 7 – source data 1). For glutamatergic neurons, the high CC reflects their strong reciprocal connections with the hypothalamus and striatum (Figure 7D, upper right). For cholinergic and PV+ GABAergic neurons, the CCs between input and output distributions were much lower, reflecting the facts that while both cell types receive strong input from the striatum, cholinergic neurons project strongly to the cerebral cortex, and PV+ neurons to the pallidum and hypothalamus (Figure 7D, upper and lower left).

Discussion

Using virus-mediated circuit mapping, we have characterized the whole-brain distributions of BF long-range connections, available in an open-access online database (http://sleepcircuits.org/bf/). Our experiments confirmed many previously demonstrated connections, but with cell-type specificity and quantitative analyses at multiple spatial scales. For example, we found that cortical inputs[92,93] to all four BF cell types originate primarily from the agranular insular and orbital areas of the prefrontal cortex (Figure 2). While a previous ultrastructural study failed to detect convincing synaptic contact between prefrontal axons and BF cholinergic neurons[120], our RV-mediated transsynaptic tracing demonstrated extensive monosynaptic innervation, which was also validated by electrophysiological recordings (Figure 4B and C). These findings have important implications on how the prefrontal cortex may exert top-down control of neural processing through its projection to the BF[121]. A recent study showed that cholinergic neurons in the BF are strongly activated by reinforcement signals during an auditory detection task[99]. Our whole-brain mapping of their inputs provides a list of candidate neurons through which the reinforcement signals are conveyed to the BF cholinergic neurons.

Regarding the outputs, we found striking differences across cell types (Figure 6). A recent study has shown that cholinergic, glutamatergic, and PV+ neurons all promote wakefulness, while SOM+ neurons promote sleep[65]. The distinct projection patterns between cholinergic and glutamatergic/PV+ neurons (Figure 6) suggest that they preferentially regulate different brain functions during wakeful states. In a recent study, optogenetic activation of BF PV+ neurons was shown to enhance cortical gamma band oscillations[103]. In addition to direct projections to the cortex, our study showed extensive subcortical projections of PV neurons, which may also contribute to the regulation of cortical gamma oscillations. The output distribution of SOM+ neurons, on the other hand, was highly correlated with the input distributions of all BF cell types (Figure 7C, bottom row); the broad GABAergic inhibition of these input areas by SOM+ neurons may be important for the sleep-promoting effect. Thus, while the highly convergent inputs from multiple brain areas allow a variety of sensory, motor, cognitive, and emotional signals to be integrated within the BF, the distinct projections by different cell types may enhance the versatility of the BF in coordinating diverse functions of multiple brain networks.

Materials and Methods

Virus preparation.

Transsynaptic retrograde tracing.

To construct AAV2-EF1α-FLEX-eGFP-2a-TVA and AAV2-EF1α-FLEX-RG, TVA and eGFP linked by the 2A 'self-cleaving' peptide or rabies glycoprotein was respectively cloned into pAAV-MCS (Stratagene, La Jolla CA) in an antisense direction flanked by a pair of canonical loxP sites and a pair of lox2272 sites. AAV particles (AAV2/2) were produced by co-transfection of packaging plasmids into HEK293T cells, and cell lysates were fractionated by iodixanol gradient ultracentrifugation. Viral particles were further purified from the crude fraction by heparin affinity column (HiTrap Heparin HP Columns; GE Healthcare, Pittsburgh, PA), desalted and concentrated with Amicon Ultra Centrifugal Filter (100K, Millipore, Bellerica, MA). The genomic titer of AAV2-EF1α-FLEX-eGFP-2a-TVA (4.4×10^{13} gc/ml) and AAV2-EF1α-FLEX-RG (2.2×10^{12} gc/ml) was estimated by quantitative PCR. eGFP-2a-TVA and rabies glycoprotein were subcloned from the AAV-TRE-HTG plasmid from L. Luo.

RV-ΔG-tdTomato was amplified in B7GG cells and pseudotyped using BHK-EnvA cells. EnvA pseudotyped rabies virus was titered (1.5×10^9 IU/ml) by infecting the 293T-TVA8000 (Narayan et al., 2003) cell line with serial dilutions of the stock virus. RV-ΔG-tdTomato was a gift from B. Lim. B7GG cells, BHK-EnvA cells (Wickersham et al., 2007), and 293T-TVA8000 cells were gifts from E. Callaway.

Anterograde axon tracing.

AAV2-EF1α-FLEX-mCherry was purchased from the UNC Vector Core (Chapel Hill, NC) and the titer was estimated to be ~10^{12} gc/ml.

Surgery and viral injections.

All experimental procedures were approved by the Animal Care and Use Committee at the University of California, Berkeley. For the current study, we targeted the caudal portion of the BF (including the horizontal limb of the diagonal band of Broca, magnocellular preoptic nucleus, and substantia innominata) rather than the rostral nuclei (medial septum and the vertical limb of the diagonal band of Broca). For virus injection, adult (> P40) *Chat*$^{\text{tm2(cre)Lowl}}$ (ChAT-Cre, JAX#006410), *Slc17a6*$^{\text{tm2(cre)Lowl}}$ (Vglut2-Cre, JAX#016963), *Pvalb*$^{\text{tm1(cre)Arbr}}$ (PV-Cre, JAX#008069), and *Sst*$^{\text{tm2.1(cre)Zjh}}$ (SOM-Cre, JAX#013044) mice were anesthetized with 1.5% isoflurane in oxygen (flow rate of 0.5 - 1L/min). A craniotomy (~0.5 mm diameter) was made at 0.1 mm posterior to bregma, 1.3 mm lateral to midline. For anterograde axon tracing, 300-400 nL of AAV (serotype 2) expressing Cre-dependent mCherry (AAV2-EF1α-FLEX-mCherry) was stereotactically injected into the BF (5.2 mm from brain surface) using Nanoject II (Drummond Scientific, Broomall, PA) via a micro pipette. The following steps were taken to minimize virus leaking into the injection track: (1) The pipette opening was minimized (< 20 μm); (2) The injector was mounted onto a motorized manipulator to ensure slow and smooth retraction; (3) The injection started 5 min after pipette insertion, and multiple 23 or 40 nl injections (13 nl/s) were made at 15-30 s intervals. The pipette was retracted 10 min after injection.

For transsynaptic retrograde tracing, 200-300 nl of helper AAV (AAV2-EF1α-FLEX-eGFP-2a-TVA and AAV2-EF1α-FLEX-RG mixed at 1:1 ratio of viral particles) was injected into the BF using the same procedure as described above. Two to three weeks after helper AAV injection, RVΔG-tdTomato+EnvA was injected into the same location. To further ensure localized virus expression, the helper AAV injection pipette was tilted at 20 degrees from vertical while RV injection pipette was inserted vertically in the majority of experiments.

Tissue processing.

Brain tissue was processed according to standard procedures. In brief, two to three weeks after AAV injection (for anterograde tracing) or one week after RV injection (for retrograde tracing), mice were deeply anesthetized with isoflurane and immediately perfused intracardially with ~15 ml of phosphate-buffered saline (PBS) (pH 7.2) followed by ~15 ml of 4% paraformaldehyde (PFA) in PBS. Brain tissue was carefully removed, post-fixed in 4% PFA in PBS at 4 °C overnight, dehydrated in 30% sucrose in PBS for 48 hr, and embedded in Tissue Freezing Medium (Triangle Biomedical Sciences, Cincinnati, OH, Waltham, MA). Brains were cut in 30 or 50 µm coronal sections using a cryostat (Thermo Scientific) and mounted with VECTASHIELD® mounting medium with DAPI (Vector Laboratories, Burlingame, CA) or DAPI Fluoromount-G (Southern Biotech, Birmingham, AL). One out of every three sections were imaged using 20X/0.75 objective in a high-throughput slide scanner (Nanozoomer-2.0RS, Hamamatsu, Japan) for further processing. We also imaged selected brain regions (Figures 2 and 3) using a Zeiss (Germany) inverted AxioObserver Z1 fully motorized microscope with LSM 710 confocal scanhead, 10X/0.3 EC Plan Neofluar M277 objective or a 20X/0.8 Plan Apochromat M27 objective.

Immunostaining.

To check for cell-type specific expression of rabies glycoprotein, tdTomato transgenic reporter mice (JAX#007914) were crossed to Cre-transgenic mice for each cell type and double transgenic offspring were injected with AAV2-EF1a-FLEX-RG. Alternatively, Cre-transgenic mice were injected with AAV2-EF1a-FLEX-mCherry and AAV2-EF1a-FLEX-RG. After making coronal sections, brain slices were washed in PBS (3 x 10 min., room temperature), blocked with mouse IgG blocking reagent (Mouse on Mouse (M.O.M.) Kit, Vector Laboratories, Burlingame, CA) for 2 hr at room temperature, incubated with mouse anti-rabies glycoprotein (clone 24-3F-10, EMD Millipore, Billerica, MA) with M.O.M. protein concentrate in PBST (PBS + 0.3% Triton-X100) for 18 hours at room temperature, washed in PBST (3 x 20 min., room temperature), incubated with Alexa-Fluor 488 or 647 donkey anti-mouse (ThermoFisher Scientific, Waltham, MA) with M.O.M protein concentrate in PBST for 3 hours at room temperature, and finally washed in PBST (3 x 10 min, room temperature) prior to mounting the slides.

3D reconstruction and quantification.

A software package was developed in Matlab to analyze the digitized brain images. The analysis software consists of three modules: image registration, signal detection, and quantification/visualization.

Registration module

The registration module is a reference point-based image alignment software used to align images of brain sections to the Allen Mouse Brain Atlas for further quantification and 3D reconstruction. First, we manually selected a set of reference points in both the atlas and the brain image. The module then applied several geometric transformations (translation, rotation and scaling) of the brain section to optimize the match of the reference points between the brain image and the atlas. Since histological sectioning can sometimes cause tissue compression, we allowed the scaling factors along the dorsal-ventral and medial-lateral axes to be optimized independently. Following the transformation, the match between the image and the atlas was inspected, and further adjustments were made manually if necessary. The main purpose of the manual adjustment was to correct errors generated by the registration procedure due the imperfect brain slice preparations, and it was mostly performed by research assistants not involved in the research design and unaware of the final conclusion of the study.

Detection module

The detection module has two independent sub-modules designed for counting RV-labeled cells and detecting axons, respectively. The cell counting module records the position of manually identified tdTomato-labeled neurons in each digitized brain sections image.

For axon detection, the ridge detection method was used (http://en.wikipedia.org/wiki/Ridge_detection). The following steps were taken to maximize the detection accuracy: (1) Image ridges were computed across multiple scales to extract all possible axon-like signals from each image. In the resulting binary 'ridge image', the number of pixels occupied by each detected axon depends on the length but not the thickness of the axon. In addition to valid axons, the ridge image also contains many noise pixels. (2) To remove the noise pixels due to the general background in the fluorescence image, we set a threshold based on the intensity distribution of the original image, and use this as a mask to remove the noise pixels in the ridge image obtained from step (1). (3) To remove the discrete noise pixels with fluorescence intensities higher than the general background (thus not removed by step 2), we first identified pixels that are spatially contiguous in the ridge image, computed the size of each contiguous region, and removed the regions below a threshold size. Steps 2 and 3 were repeated until satisfactory detection results were achieved. (4) The results were then visually inspected and the remaining noise pixels, which were mostly artifacts introduced during brain tissue processing, were rejected manually.

Quantification/visualization module

After detection and registration, signals were quantified across the whole brain and projected to the 3D reference atlas for better visualization. The 3D viewer plug-in of the ImageJ software was used to animate the final 3D model.

The atlas, 3D reference mouse brain, quantification ontology, and layouts for sunburst plot were obtained from the open online resource of Allen Institute for Brain Science, licensed under the Apache License (Version 2.0). Since the number of labeled neurons or axons varied across brains, the input from each region was quantified by dividing the number of labeled neurons found in that region by the total number of labeled neurons detected >850 μm from the injection

site (see Figure 1 – figure supplement 2). The output (axon projection) to each region was quantified as the number of pixels occupied by detected axons in the cleaned ridge image[106] (see Detection module above) divided by the total number of axon-occupied pixels found in the entire brain (after excluding the injection site and locations with known major fiber tracks).

Starter cell mapping.

Starter cells were manually identified from the colocalization of tdTomato and eGFP signals using Nanozoomer images scanned at multiple focal planes. The starter cells were marked using the Cell Counter ImageJ plug-in, and registered to the Allen Brain Reference Atlas as described above. A starter cell heat map was generated in Python by calculating the normalized starter cell density for all samples from each cell type and applying bicubic interpolation. For each coronal section image, the cell density was binned from an anterior-posterior range of 0.24 mm, centered at the listed brain slice coordinate (Figure 1 – figure supplement 3).

Slice recording.

To validate the synaptic input from the prefrontal cortex to BF cholinergic neurons (as shown by RV-mediated input tracing), ChR2 was expressed in excitatory neurons in the prefrontal cortex of ChAT-eGFP mice (JAX#007902, P16-P18) by injecting ~500 nl of AAV-DJ-CaMKIIα-hChR2-eYFP (~10^{13} gc/ml, Stanford Gene Vector and Virus Core, Stanford, CA) into the orbital and agranular insular areas of the PFC (2.0 mm anterior to bregma, 1.5 mm lateral, 2.0 mm from brain surface) and recording from eGFP+ BF neurons. To validate the synaptic input from ACB, Cre-inducible ChR2-eYFP was expressed in GAD2-Cre mice (JAX#010802, P16-P18) by injecting 300-400 nl of AAV-DJ-EF1α-FLEX-ChR2-eYFP (~10^{13} gc/ml, Stanford Gene Vector and Virus Core, Stanford, CA) into the ACB (1.5 mm anterior to bregma, 0.8 mm lateral, 3.6 mm from brain surface) and recordings were made (one week after virus injection) from unlabeled BF neurons, which were identified after each recording via single-cell gene-expression analysis. Slice preparation, recording procedure, and single-cell gene-expression analysis were the same as described in a recent study[65].

Figure Legends

Figure 1: **Experimental and analysis procedures for cell-type-specific circuit tracing. A)** RV-mediated transsynaptic retrograde tracing of BF inputs. Upper panel, viral vectors and injection procedure. Lower panel, fluorescence images of BF in the region of the NDB (red box in coronal diagram) in ChAT-, VGLUT2-, PV-, and SOM-Cre mice. Scale bar, 200 µm. Inset, enlarged view of the region in white box showing starter cells (yellow, expressing both eGFP and tdTomato, indicated by white arrowheads). Scale bar, 50 µm. NDB, diagonal band nucleus; SIB, substantia innominata, basal part; MCPO, magnocellular preoptic nucleus; VP, ventral pallidum; LPO, lateral preoptic area. **B)** Viral vector and injection procedure for tracing BF axonal projections. **C)** Flow chart showing the main steps in data generation and processing.

Figure 2: Inputs to each BF cell type from selected brain regions. Examples of RV-labeled input neurons to each of the four BF cell types in seven selected brain structures (black box in each coronal diagram). Scale bar, 200 µm. In each coronal diagram, RV-labeled neurons detected in all four brain samples are indicated by red dots. Bottom panel, mean percentage of input neurons in each brain structure for the four BF cell types. Error bar, ± s.e.m. Bar color indicates which of the 12 regions the given brain structure belongs to as depicted in Figure 3. ac, anterior commissure; aq, cerebral aqueduct; BLA, basolateral amygdalar nucleus; DMH, dorsomedial nucleus of the hypothalamus; DR, dorsal nucleus raphe; IPN, interpeduncular nucleus; opt, optic tract; scp, superior cerebellar peduncles; SNr, substantia nigra reticularis; VMH, ventromedial hypothalamic nucleus.

Figure 3: Whole-brain distributions of inputs to the four BF cell types.

A) Percentages of retrogradely labeled input neurons in 53 brain areas (ChAT, n = 5 mice; VGLUT2, n = 5; PV, n = 3; SOM, n = 4). Brain areas are grouped into 12 generalized, color-coded brain structures. HPF, hippocampal formation. Abbreviations of the 53 brain areas and their percentages of inputs are listed in Figure 3 – source data 1. Error bar, ± s.e.m. Since labeled neurons in coronal sections near the injection site were excluded from analysis (see Figure 1 – figure supplement 2), inputs from the pallidum are likely to be underestimated. **B)** Whole-brain 3D reconstruction of the inputs to the four BF cell types. The blue-shaded area denotes the region excluded for analysis due to potential local contamination (see Figure 1 – figure supplement 2)

Figure 4: Optogenetic characterization of monosynaptic inputs to the BF from PFC and ACB. A) Schematic of experiment. ChR2 was expressed in excitatory neurons in the prefrontal cortex of ChAT-eGFP mice by injecting AAV-DJ-CaMKIIα-hChR2-eYFP. Coronal slices of the BF were used for recording experiments. **B)** Excitatory postsynaptic potentials recorded from ChAT+ neurons (under whole-cell current clamp) evoked by blue-light activation of the prefrontal cortical axons. Upper, response to a single light pulse (5 ms) in an example ChAT+ neuron; lower, responses to 10 pulses at 10 Hz recorded from a different ChAT+ neuron. **C)** Summary of the peak amplitude of the response to a single light pulse. Each circle represents data from one BF ChAT+ neuron (n = 9 neurons from 2 mice). Bar, mean ± s.e.m. **D)** Diagram illustrates virus injection site in the ACB and recording site in the BF. AAV-DJ-EF1α-FLEX-

ChR2-eYFP was injected into the ACB of GAD2-Cre mice and whole-cell voltage-clamp recordings (clamped at 0 volts) were made from BF neurons. Single-cell gene-expression analysis was performed after each recording session to identify the cell type of each recorded neuron. **E)** Example traces of laser-evoked responses in the four BF cell types. **F)** Summary of the peak current amplitude of each neuron's response (ChAT+, n = 5 neurons from 5 mice; VGLUT2+, n = 4 neurons from 4 mice; PV+, n = 3 neurons from 3 mice; SOM+, n = 8 neurons from 4 mice). Gray indicates no significant response.

Figure 5: Axon projections of each BF cell type to selected brain regions. Examples of axon projections from each of the four BF cell types to seven selected brain structures (black box in each coronal diagram). Scale bar, 250 µm. DMH, dorsomedial nucleus of the hypothalamus; IPN, interpeduncular nucleus; MH, medial habenula; SNr, substantia nigra reticularis; VMH, ventromedial hypothalamic nucleus.

Figure 6: Whole-brain distributions of axonal projections from the four BF cell types. A) Percentages of labeled axons in 53 brain areas (ChAT, n = 3 mice; VGLUT2, n = 3; PV, n = 3; SOM, n = 3). Error bar, ± s.e.m. Abbreviations of the 53 brain areas and their percentages of inputs are listed in Figure 6 – source data 1. **B)** Whole-brain 3D reconstruction of axon projections from each of the four BF cell types. Note that although VGLUT2+ and PV+ neuron projections showed the similar spatial distribution, there were fewer labeled axons from PV+ than VGLUT2+ neurons.

Figure 7: Comparison of input and output distributions. A) Matrix of correlation coefficients (CCs) between input distributions of each pair of cell types. **B)** Similar to **A**, for output distributions. **C)** CCs between input and output distributions. All CCs were computed at the spatial scale of the 12 major brain subdivisions (Figure 7 – source data 1). **D)** Percentage of input vs. percentage of output in each region, for each of the four BF cell types. Filled circles, strongly connected brain regions contributing to the high CCs for glutamatergic and SOM+ neurons and low CCs for cholinergic and PV+ neurons in **C**.

Figures

Figure 1.

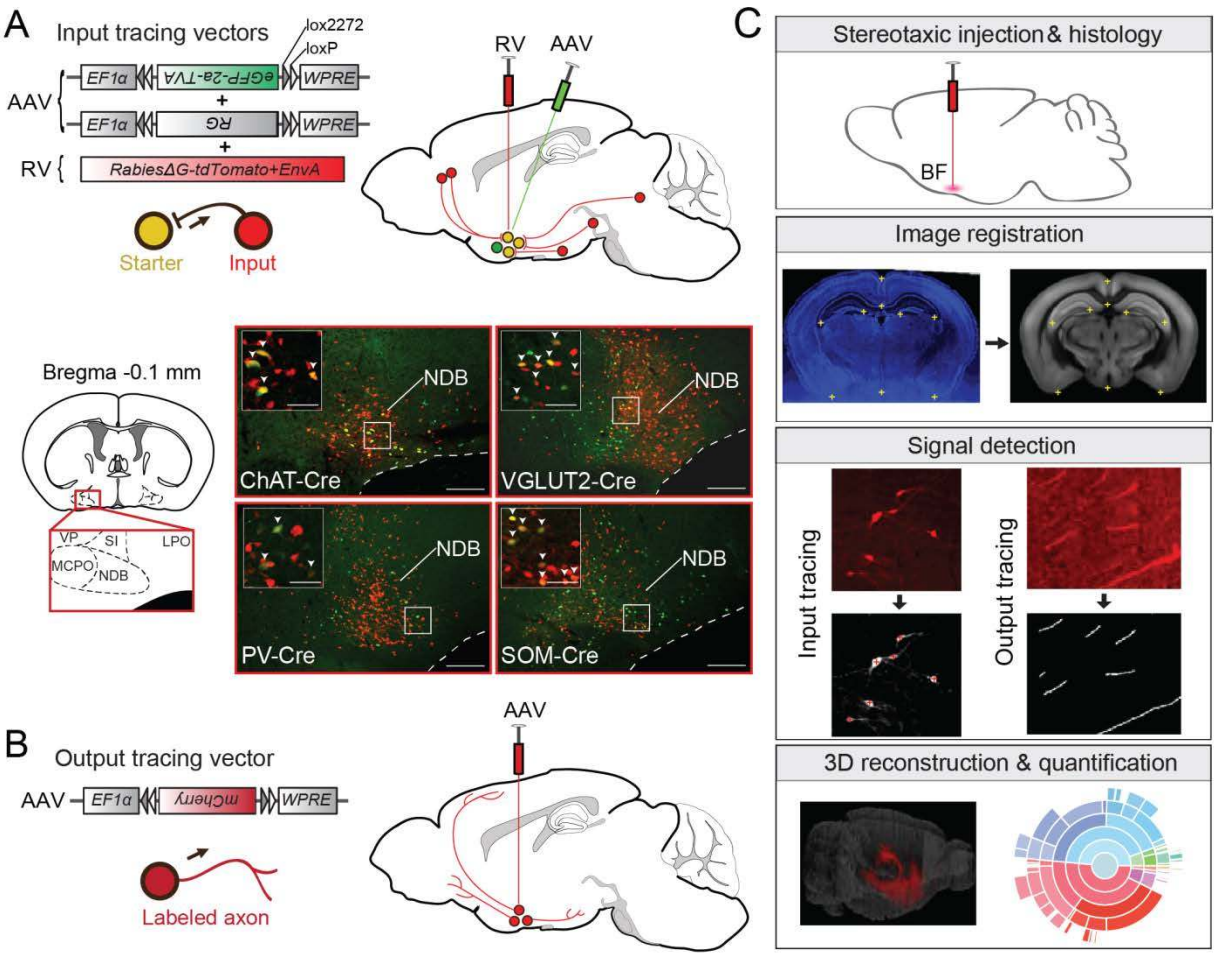

Figure 2.

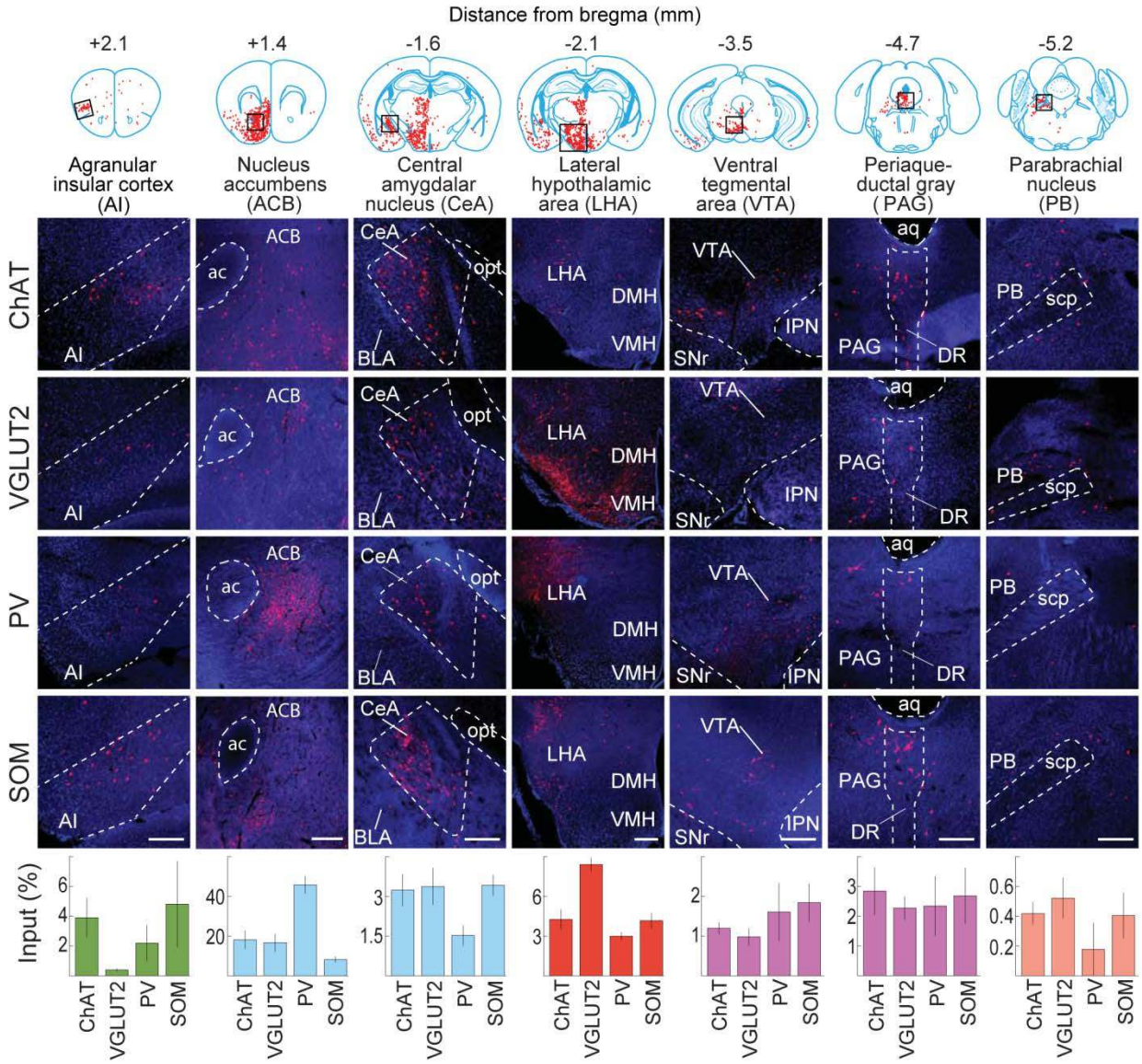
Distance from bregma (mm)
+2.1
+1.4
-1.6
-2.1
-3.5
-4.7
-5.2
Agranular insular cortex (AI)
Nucleus accumbens (ACB)
Central amygdalar nucleus (CeA)
Lateral hypothalamic area (LHA)
Ventral tegmental area (VTA)
Periaque-ductal gray (PAG)
Parabrachial nucleus (PB)
ChAT
VGLUT2
PV
SOM
AI
ACB
ac
CeA
opt
BLA
LHA
DMH
VMH
VTA
SNr
IPN
aq
PAG
DR
PB
scp
Input (%)
ChAT
VGLUT2
PV
SOM

Figure 3.

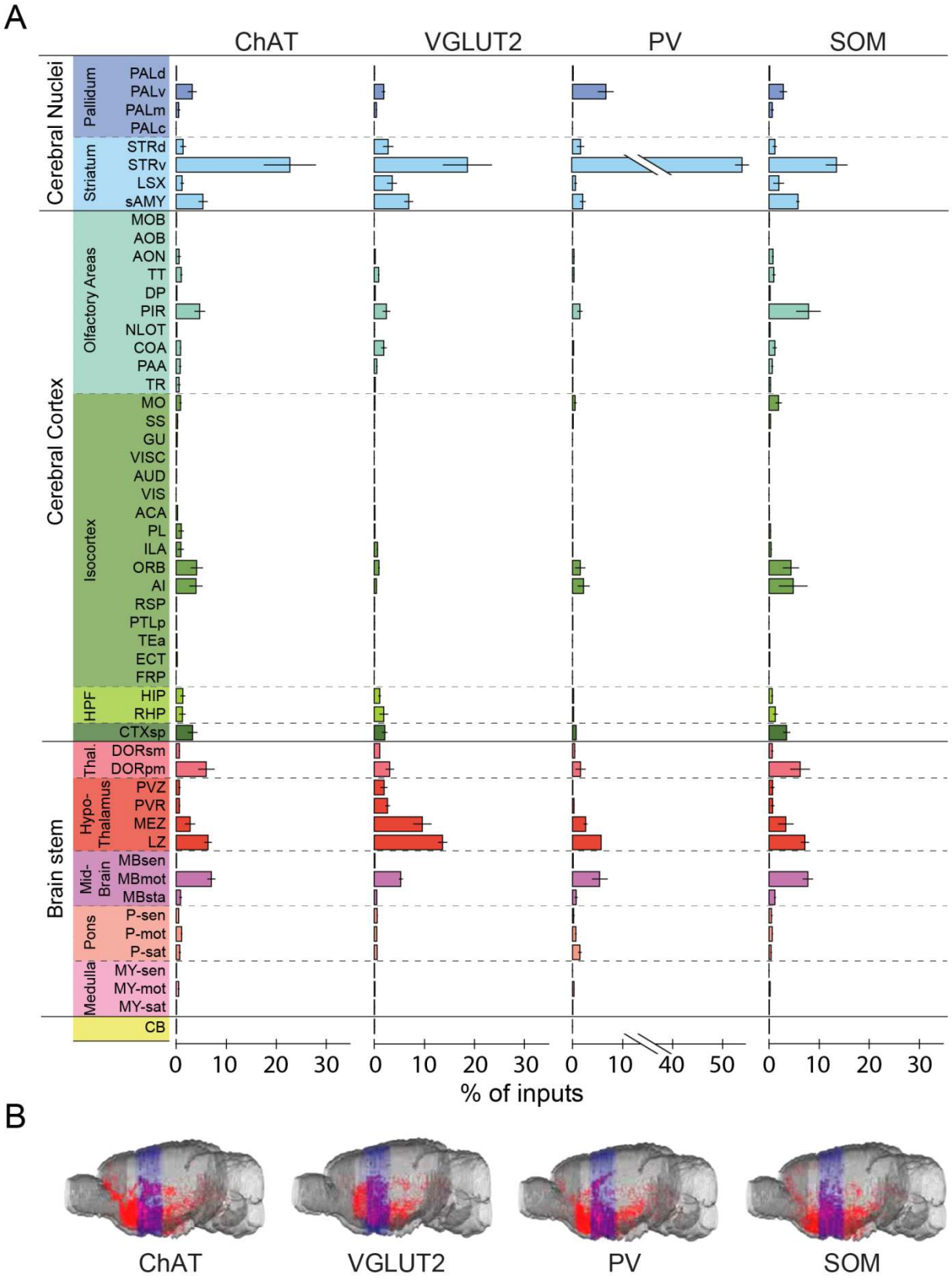
A
ChAT
VGLUT2
PV
SOM
Cerebral Nuclei
Pallidum
PALd
PALv
PALm
PALc
Striatum
STRd
STRv
LSX
sAMY
Cerebral Cortex
Olfactory Areas
MOB
AOB
AON
TT
DP
PIR
NLOT
COA
PAA
TR
Isocortex
MO
SS
GU
VISC
AUD
VIS
ACA
PL
ILA
ORB
AI
RSP
PTLp
TEa
ECT
FRP
HPF
HIP
RHP
CTXsp
Brain stem
Thal.
DORsm
DORpm
Hypo-Thalamus
PVZ
PVR
MEZ
LZ
Mid-Brain
MBsen
MBmot
MBsta
Pons
P-sen
P-mot
P-sat
Medulla
MY-sen
MY-mot
MY-sat
CB
0 10 20 30
0 10 20 30
0 10 40 50
0 10 20 30
% of inputs
B
ChAT
VGLUT2
PV
SOM

Figure 4.

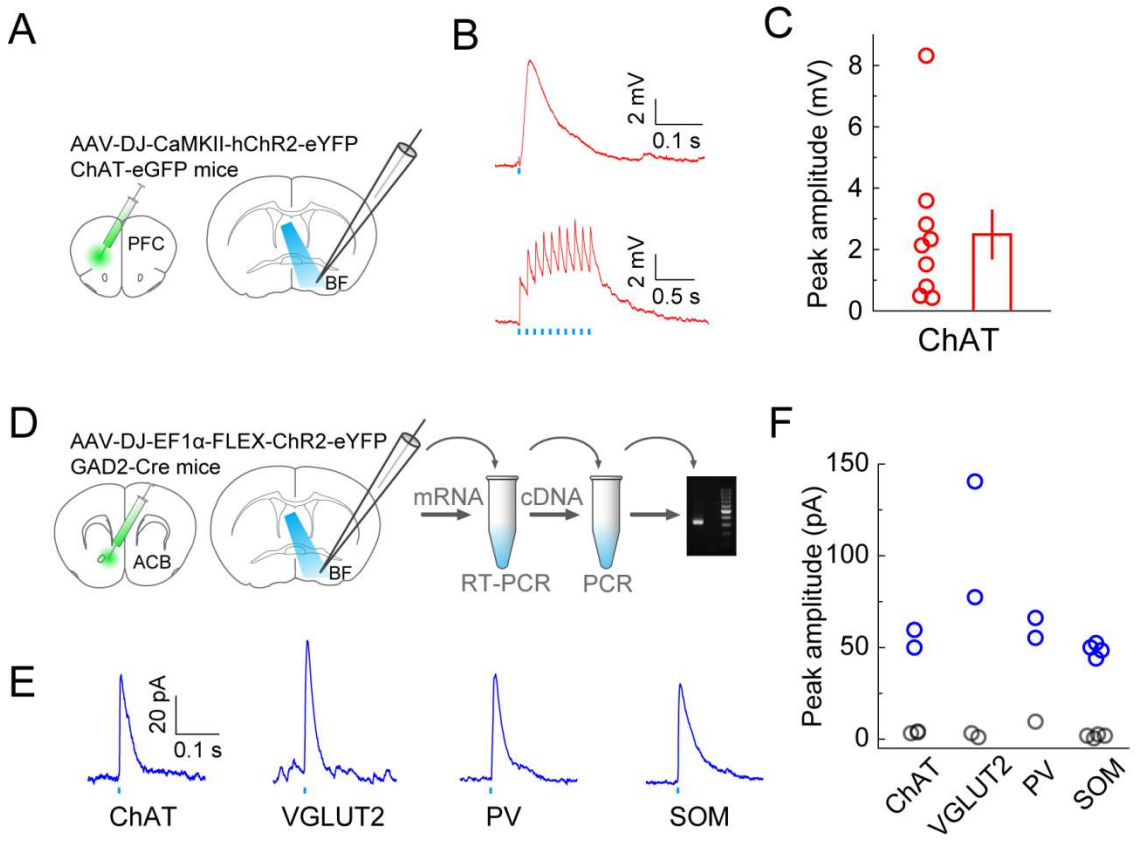
A
AAV-DJ-CaMKII-hChR2-eYFP
ChAT-eGFP mice
PFC
BF
B
2 mV
0.1 s
2 mV
0.5 s
C
Peak amplitude (mV)
8
6
4
2
0
ChAT
D
AAV-DJ-EF1α-FLEX-ChR2-eYFP
GAD2-Cre mice
ACB
BF
mRNA
cDNA
RT-PCR
PCR
E
20 pA
0.1 s
ChAT
VGLUT2
PV
SOM
F
Peak amplitude (pA)
150
100
50
0
ChAT
VGLUT2
PV
SOM

Figure 5.

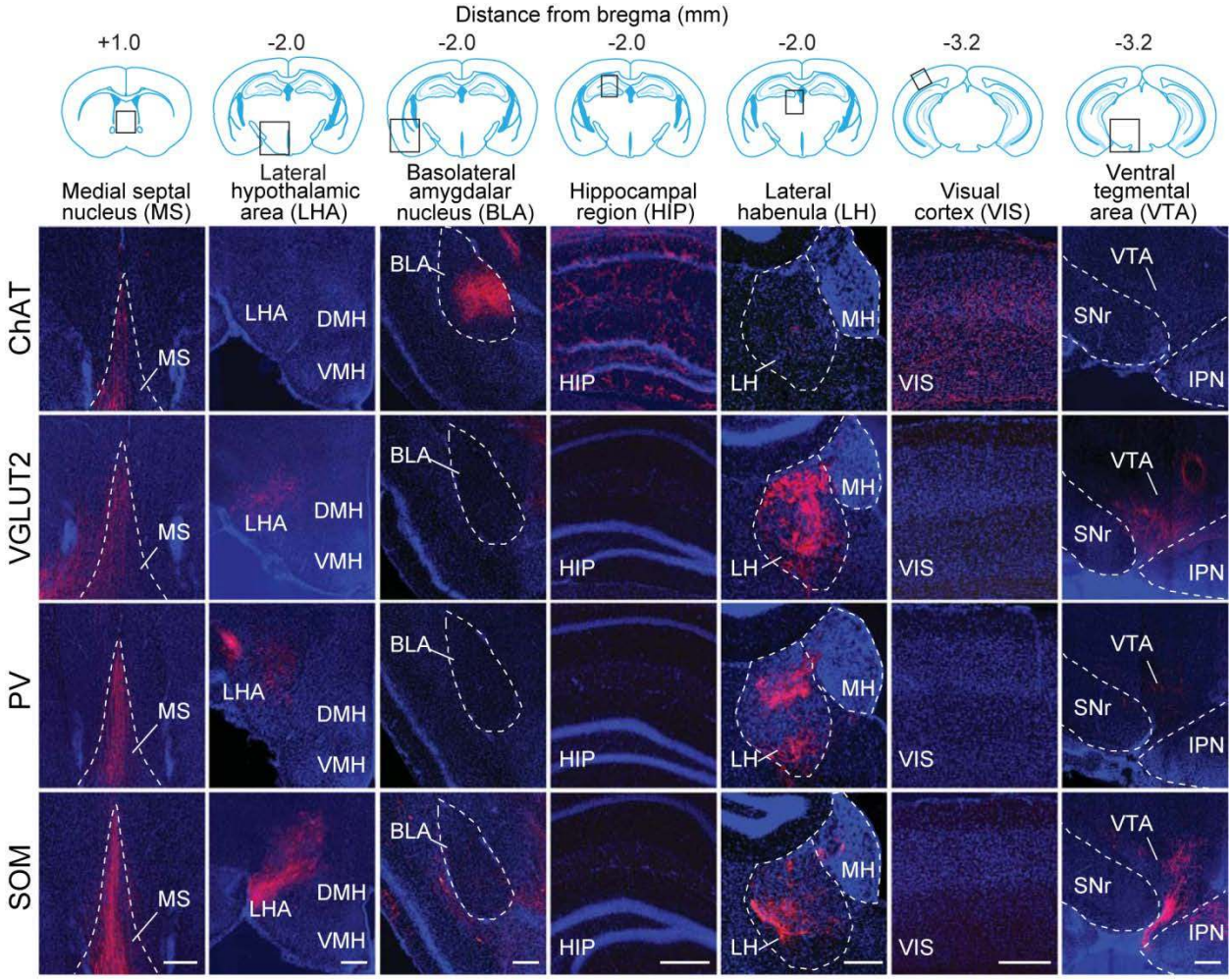
Distance from bregma (mm)
+1.0
-2.0
-2.0
-2.0
-2.0
-3.2
-3.2
Medial septal nucleus (MS)
Lateral hypothalamic area (LHA)
Basolateral amygdalar nucleus (BLA)
Hippocampal region (HIP)
Lateral habenula (LH)
Visual cortex (VIS)
Ventral tegmental area (VTA)
ChAT
VGLUT2
PV
SOM
MS
LHA
DMH
VMH
BLA
HIP
MH
LH
VIS
VTA
SNr
IPN

Figure 6.

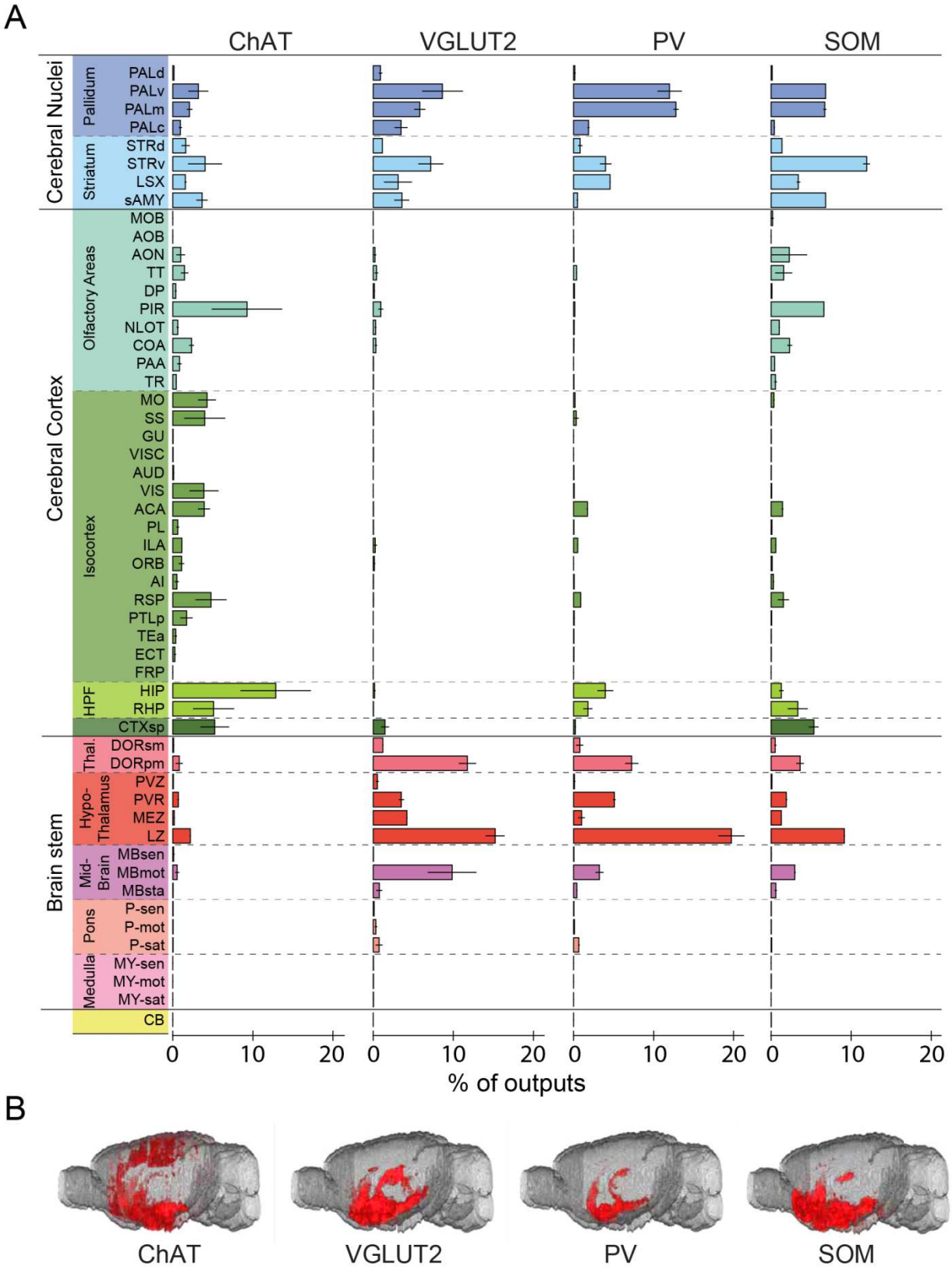
A
ChAT
VGLUT2
PV
SOM
Cerebral Nuclei
Pallidum
PALd
PALv
PALm
PALc
Striatum
STRd
STRv
LSX
sAMY
Cerebral Cortex
Olfactory Areas
MOB
AOB
AON
TT
DP
PIR
NLOT
COA
PAA
TR
Isocortex
MO
SS
GU
VISC
AUD
VIS
ACA
PL
ILA
ORB
AI
RSP
PTLp
TEa
ECT
FRP
HPF
HIP
RHP
CTXsp
Brain stem
Thal.
DORsm
DORpm
Hypo-Thalamus
PVZ
PVR
MEZ
LZ
Mid-Brain
MBsen
MBmot
MBsta
Pons
P-sen
P-mot
P-sat
Medulla
MY-sen
MY-mot
MY-sat
CB
0
10
20
% of outputs
B
ChAT
VGLUT2
PV
SOM

Figure 7.

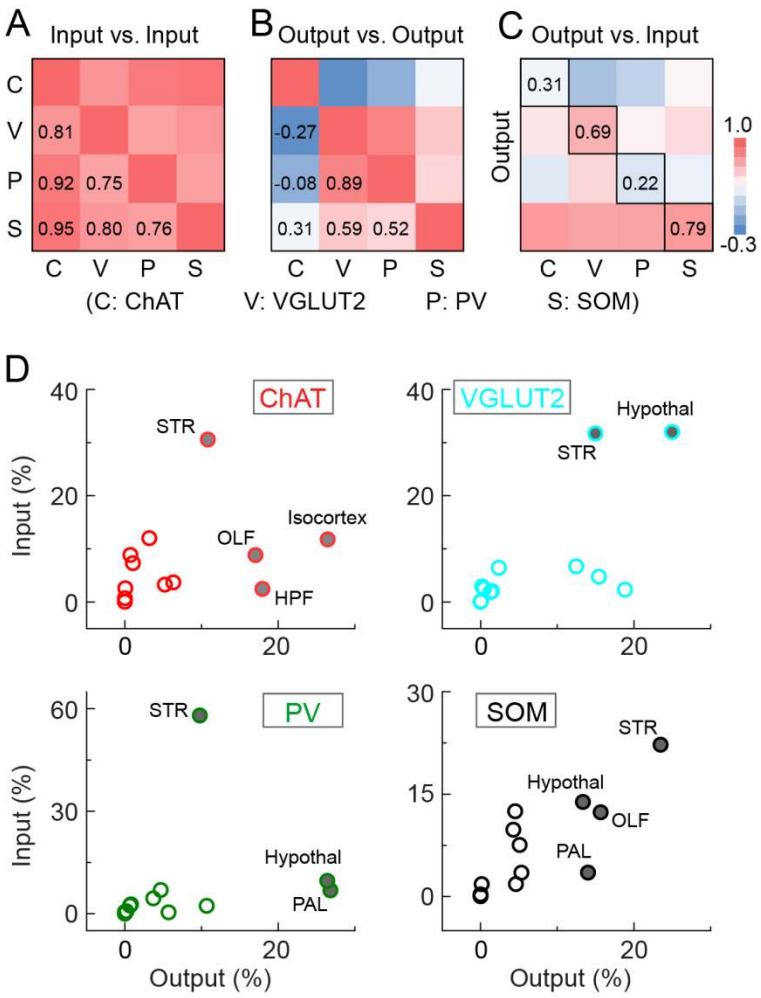
A Input vs. Input
B Output vs. Output
C Output vs. Input
C
V
P
S
0.81
0.92 0.75
0.95 0.80 0.76
-0.27
-0.08 0.89
0.31 0.59 0.52
0.31
0.69
0.22
0.79
Output
1.0
-0.3
C V P S
(C: ChAT V: VGLUT2 P: PV S: SOM)
D
ChAT
VGLUT2
PV
SOM
STR
Isocortex
OLF
HPF
Hypothal
PAL
Input (%)
Output (%)
0
20
40
60
30
15

Supplemental Figure Legends

Figure 1 – figure supplement 1: Cell-type specificity of Cre-dependent rabies glycoprotein expression. A) Colocalization of rabies glycoprotein immunostaining with Cre expression (indicated by tdTomato or mCherry reporters) in each of the four Cre lines. White arrowheads indicate cells with colocalization. No rabies glycoprotein expression was detected when injected into wild type mice. **B)** Percentage of rabies glycoprotein expressing cells that are positive for tdTomato or mCherry, averaged across brain samples. Error bar, ± standard deviation (91 ChAT cells; 89 VGLUT2 cells; 70 PV cells; 100 SOM cells; n = 2 mice per line).

Figure 1 – figure supplement 2: **Control experiments for RV tracing of inputs. A)** Injection of RV without prior AAV injection resulted in no tdTomato-labeled neurons, indicating dependence of the RV infection on AAV-induced expression of TVA. **B)** Injection of AAV2-EF1α-FLEX-eGFP-2a-TVA and AAV2-EF1α-FLEX-RG followed by RV injection in the BF of wild-type mice not expressing Cre led to no eGFP expression, indicating Cre-dependence of the AAV vector. However, tdTomato-labeled neurons were observed at the injection site (radius < 500 μm), most likely due to the leaky expression of a low level of TVA, as previously noted[109,113] **C)** Upper panel, Sagittal view of the experiment shown in B (but a different brain sample), with tdTomato expression near the injection site but not outside of the exclusion zone. Lower panel, enlarged view of the region in the white rectangle. **D)** Sagittal view of brain samples injected with AAV2-EF1α-FLEX-eGFP-2a-TVA followed by RV in the BF of different Cre lines (without AAV2- EF1α-FLEX-RG that enables transsynaptic spread of RV) to determine the spatial extent of the exclusion zone in the RV tracing experiments. After excluding the horizontal limb of the diagonal band of Broca (part of the BF region targeted), we found very few (< 30 per brain) labeled cells beyond 850 μm. Subsequent analyses were thus performed only in coronal sections > 850 μm from the injection site and outside of the horizontal limb of the diagonal band of Broca.

Figure 1 – figure supplement 3: Heat map distribution of starter cells.
Normalized starter cell density across all samples for each cell type. Each brain slice depicts the density accumulated from an anterior-posterior axis range of 0.24 mm.

Figure 1 – figure supplement 4: The relationship between the numbers of starter cells and input cells. A) The total number of starter cells for each brain sample. **B)** The convergence index (input cell count/starter cell count) for each brain sample grouped by cell-type.

Figure 4 – figure supplement 1: Basal forebrain input from the prefrontal cortex.
A) Example fluorescence image of a coronal section at the virus injection site in the prefrontal cortex (PFC). **B)** Example fluorescence image of the PFC axon fibers in the basal forebrain from the same experiment as shown in panel A.

Figure 7 – figure supplement 1: **Correlation coefficients between individual brain samples for input and output distributions. A)** Input. **B)** Output. Note the higher CCs within the boxes

along the diagonal (between samples of the same cell type) than those outside of the boxes (between samples of different cell types). The CCs exactly along the diagonal (each brain sample with itself, CC = 1) were excluded from analysis.

Supplemental Figures

Figure 1 – figure supplement 1.

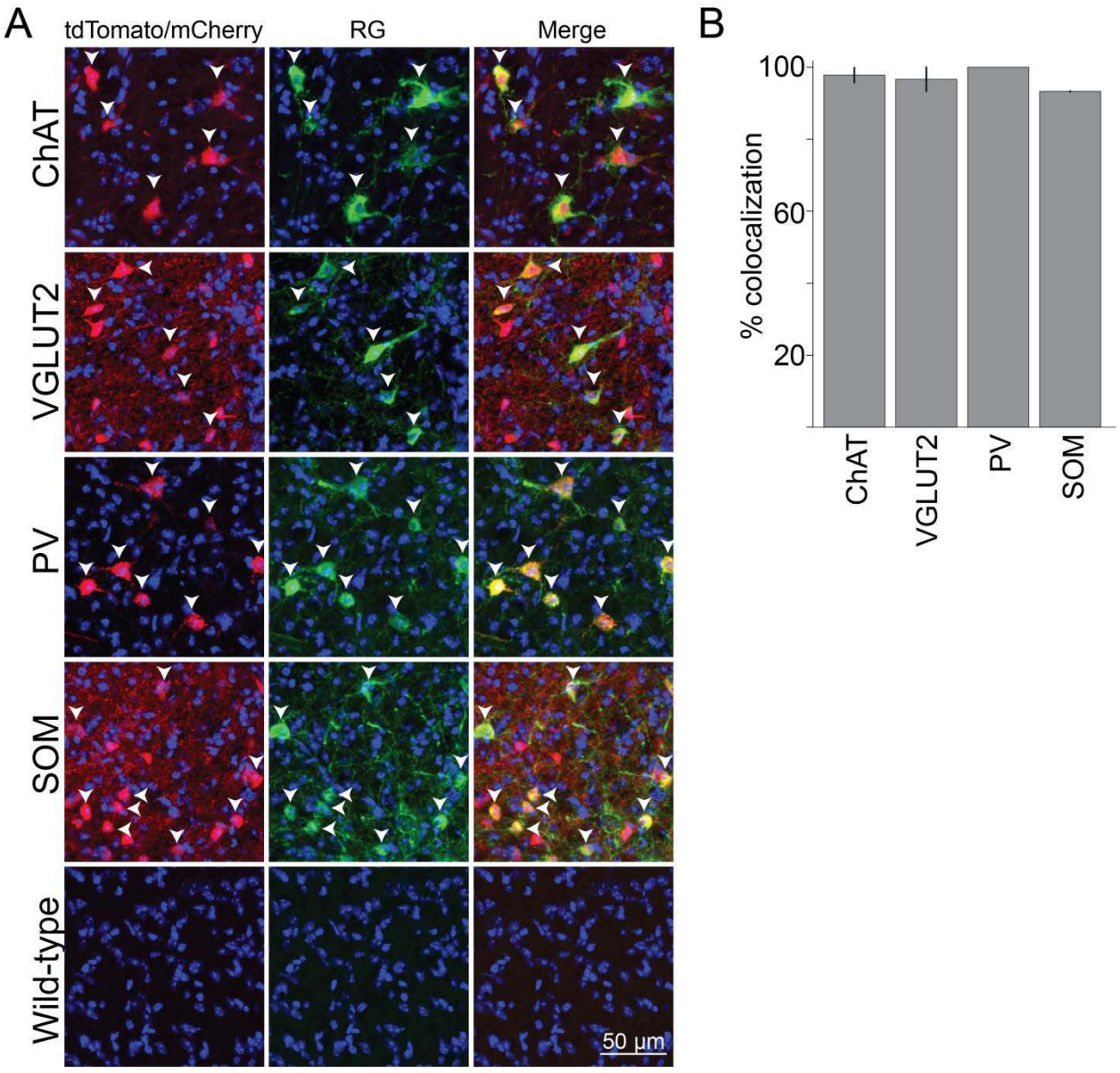

Figure 1 – figure supplement 2.

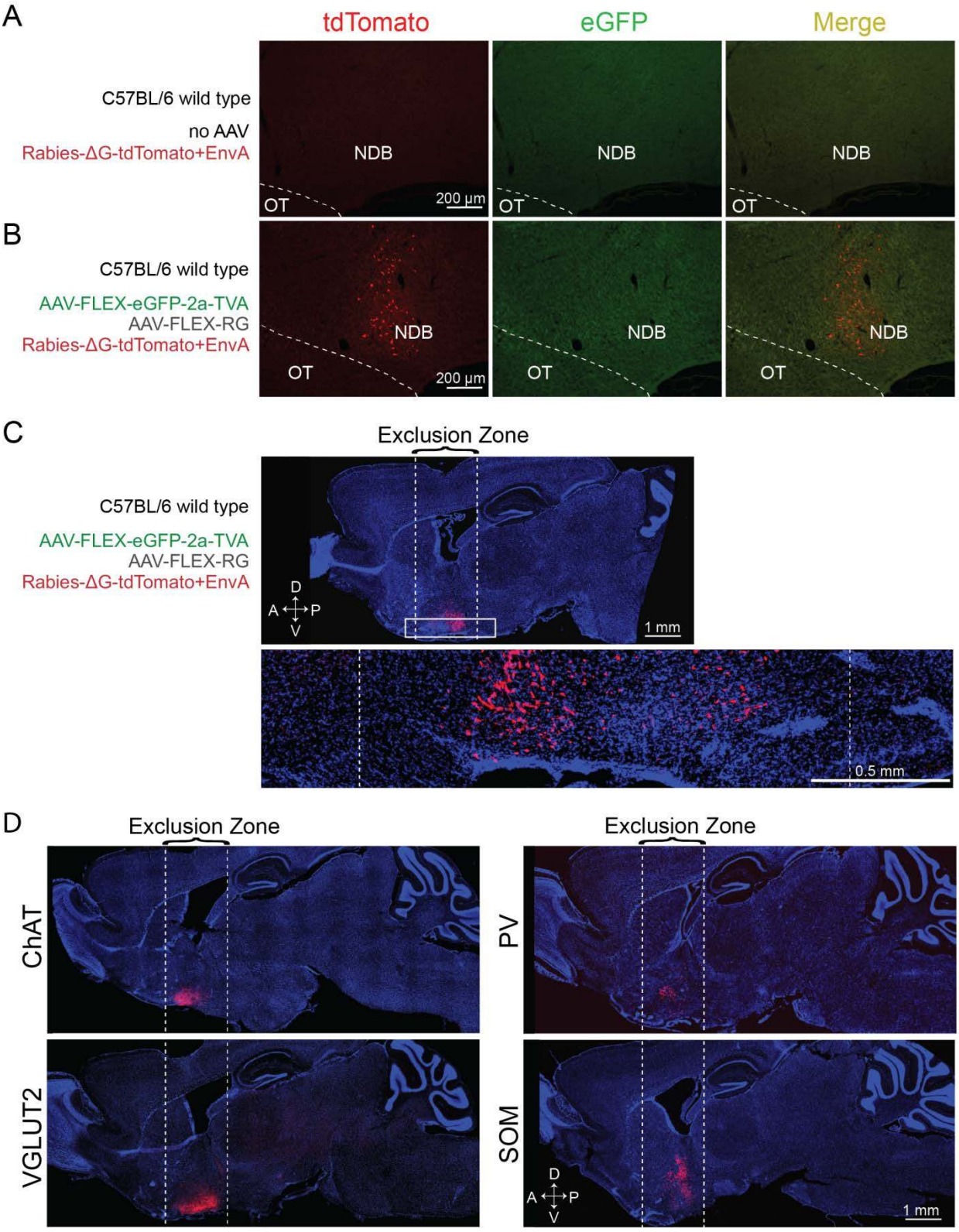

Figure 1 – figure supplement 3.

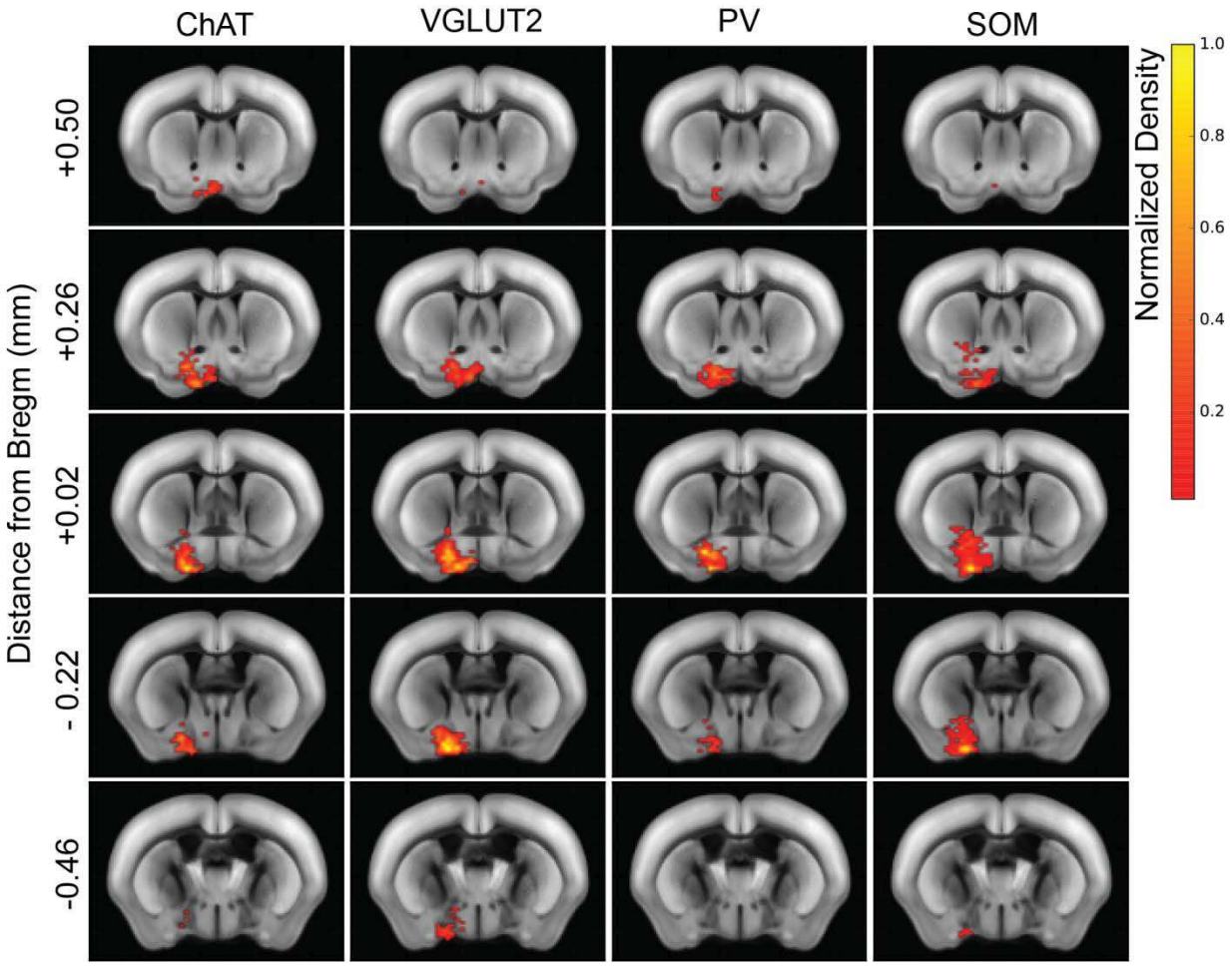

Figure 1 – figure supplement 4.

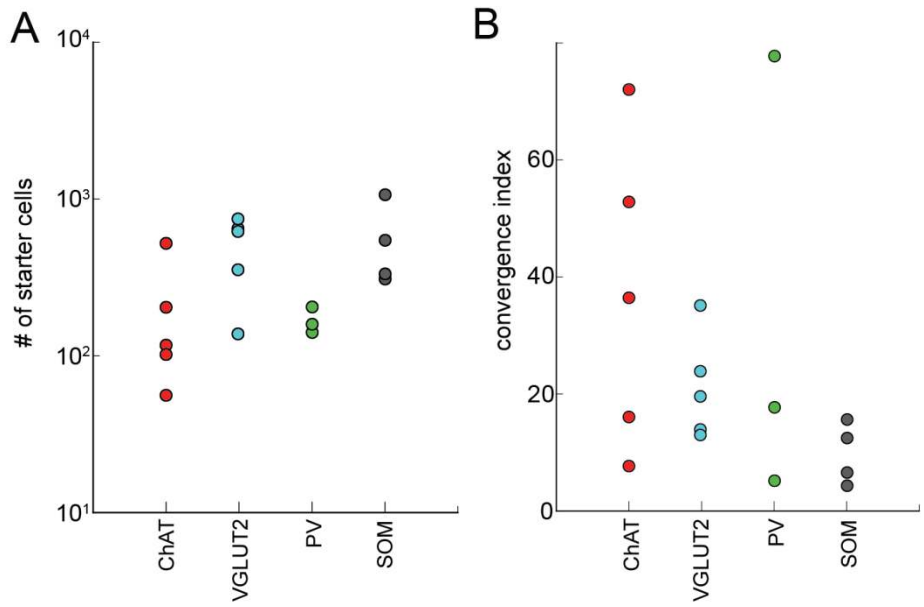

Figure 4 – figure supplement 1.

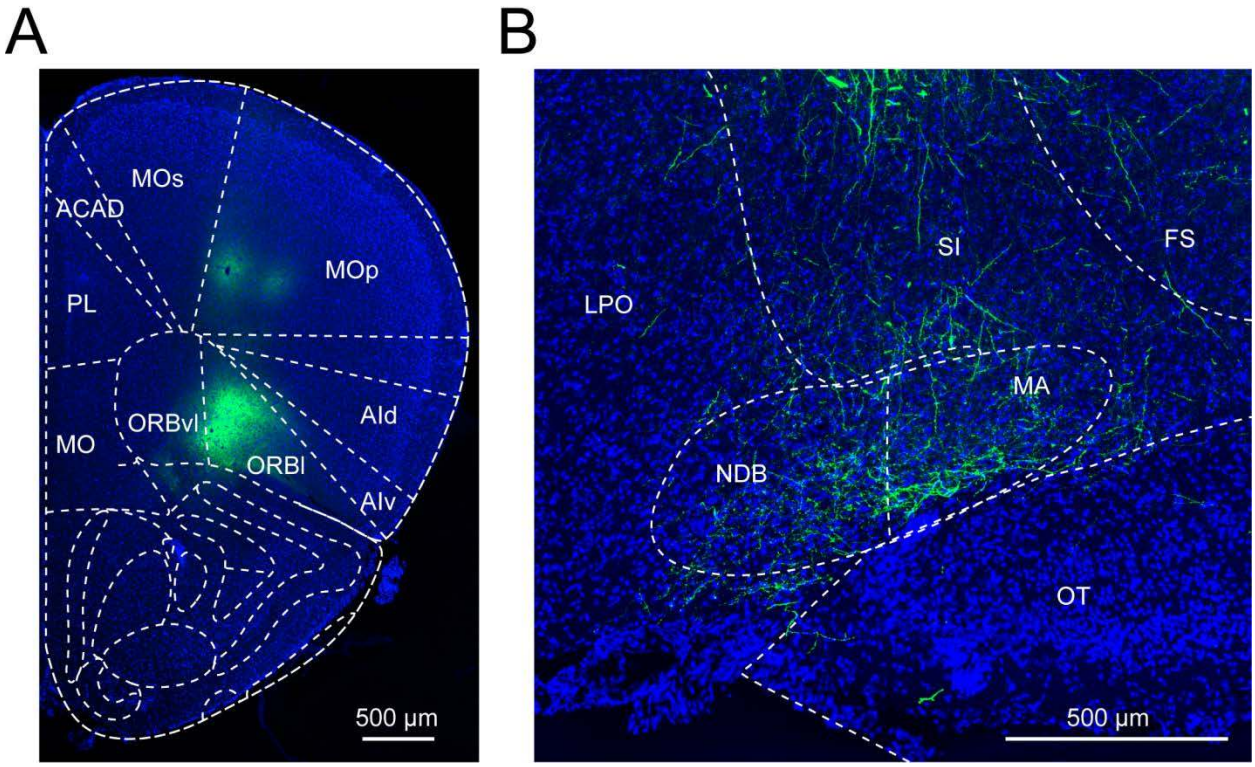

Figure 7 – figure supplement 1.

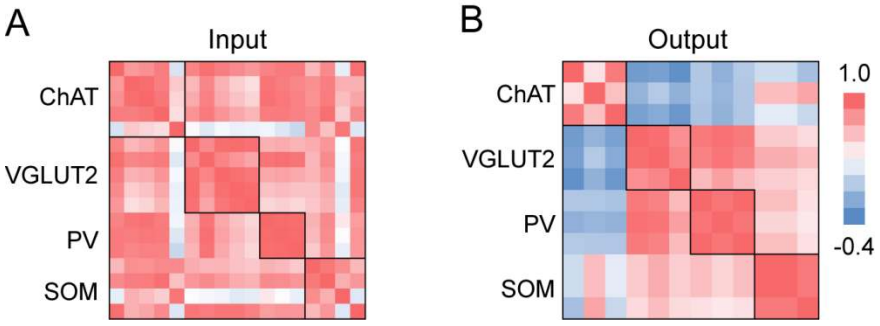

CHAPTER 3:

Regulation of REM and Non-REM Sleep by Periaqueductal GABAergic Neurons

Summary

Mammalian sleep consists of distinct rapid eye movement (REM) and non-REM (NREM) states. The midbrain region ventrolateral periaqueductal gray (vlPAG) is known to be important for gating REM sleep, but the underlying neuronal mechanism is not well understood. Here we show that activating vlPAG GABAergic neurons in mice suppresses the initiation and maintenance of REM sleep while consolidating NREM sleep, partly through their projection to the dorsolateral pons. Cell-type-specific recording and calcium imaging showed that most vlPAG GABAergic neurons are strongly suppressed at REM sleep onset and activated at its termination. In addition to the rapid changes at brain state transitions, their activity decreases gradually between REM sleep and is reset by each REM episode in a duration-dependent manner, mirroring the accumulation and dissipation of REM sleep pressure. Thus, vlPAG GABAergic neurons powerfully gate REM sleep, and their firing rate modulation may contribute to the ultradian rhythm of REM/NREM alternation.

Introduction

During behavioral sleep, the mammalian brain alternates between two distinct states – REM sleep with desynchronized EEG and NREM sleep characterized by large-amplitude slow-wave activity. While the switch between these brain states occurs rapidly within seconds, the recurrence of the NREM/REM cycle follows a much slower ultradian rhythm, on a time scale of minutes in rodents to hours in humans[122]. Understanding the mechanisms controlling sleep requires characterization of the neuronal processes operating on both time scales.

The vlPAG in the midbrain is known to play an important role in gating REM sleep. Inhibition of the vlPAG and the nearby deep mesencephalic reticular nucleus (DpMe) through muscimol injection causes a marked increase in REM sleep[38,123–125], whereas disinhibition of this area with bicuculline decreases REM sleep. Lesion of the vlPAG neurons also increases REM sleep in cats[126], rats[34] and mice[127]. c-Fos immunohistochemistry following REM sleep deprivation identified a large number of REM-off neurons that are GABAergic[38], and recent studies based on optogenetic[31] and pharmacogenetic[32] manipulations demonstrated that activation/inhibition of the vlPAG GABAergic neurons decreases/increases REM sleep.

Although these studies indicate a crucial role of the GABAergic neurons in gating REM sleep, the underlying circuit mechanism is not well understood. Anatomical tracing revealed a strong vlPAG projection to the dorsolateral pons[71], an important REM-promoting area[33–35,128,129], but the functional contribution of this projection in gating REM sleep remains to be assessed. The onset and termination of each REM sleep episode occur rapidly on a time scale of seconds. Although vlPAG GABAergic neurons have been shown to express c-fos after REM sleep deprivation[38], the slow time course of c-fos expression obscures their firing rate changes associated with brain state transitions. Furthermore, the REM/NREM alternation is known to follow an ultradian rhythm on a time scale of minutes, but the mechanism controlling the ultradian timing is poorly understood. Given the crucial role of vlPAG GABAergic neurons in gating REM sleep, an interesting question is whether their activity is modulated on a time scale of minutes, and whether such slow modulation could influence the ultradian timing of REM sleep.

In this study, we characterized the activity of vlPAG GABAergic neurons on both fast and slow time scales and assessed their roles in regulating REM and NREM sleep. We first measured the effects of activating these neurons on brain states. Rabies virus (RV)-mediated trans-synaptic retrograde tracing was used to establish the postsynaptic targets of these neurons in the dorsolateral pons, and the functional contribution of this projection in gating REM sleep was tested optogenetically. We then performed cell-type-specific recording and calcium imaging to characterize the spiking activity of these GABAergic neurons across sleep-wake cycles. Analysis of their firing rate modulation showed that while the rapid activity changes over seconds are directly associated with REM sleep onset and termination, their slow modulations over a time course of minutes closely mirror the accumulation and dissipation of REM sleep pressure, well suited for the ultradian regulation of the REM/NREM alternation. These results clarify the roles of vlPAG GABAergic neurons in both the direct gating and ultradian regulation of REM sleep.

Results

Our previous study showed that channelrhodopsin 2 (ChR2)-mediated optogenetic activation of vlPAG GABAergic neurons (20 Hz laser stimulation, 5 min per trial, applied every 15–25 min) causes a near-complete suppression of REM sleep, a strong reduction of wakefulness, and a marked increase in NREM sleep[31]. We have now confirmed these effects in additional animals (Fig. 1a-c, Supplementary Fig. 1, $P < 0.0001$ for all three brain states; bootstrap, $n = 12$ mice) and showed that they are distinct from the effects of activating vlPAG glutamatergic neurons (Supplementary Fig. 2).

To distinguish whether the laser-induced change in the percentage of time in each brain state is due to a change in the initiation or maintenance of that state, we analyzed the transition probability between each pair of brain states. Laser activation of the vlPAG GABAergic neurons caused marked decreases in NREM→REM and REM→REM transitions (Fig. 1d, e; $P < 0.001$, bootstrap), indicating a suppression of both the initiation and maintenance of REM sleep. Laser stimulation also caused significant increases in NREM→NREM and Wake→NREM transitions ($P < 0.001$). However, as shown in the cumulative transition probability analysis, the increase in the Wake→NREM transition was much weaker compared to the decreases in NREM→Wake and NREM→REM transitions (Fig. 1f), indicating that the increased NREM sleep was primarily due to enhanced maintenance rather than initiation. Consistent with these changes in transition probabilities, the mean duration of REM episodes was shortened ($P = 0.04$, $z = 7.0$, Wilcoxon sign-rank test), and the NREM episodes were prolonged (Fig. 1g; $P = 0.004$, $z = 2.0$). During the baseline period without laser, 22.2% of the NREM episodes transitioned into REM sleep and 77.8% to wakefulness; laser stimulation significantly reduced the proportion of transitions into REM sleep to 7.6% (Fig. 1h; $P = 0.003$, $z = 1.0$, Wilcoxon signed-rank test). Interestingly, the effect of laser stimulation on the initiation of wakefulness depended on the preceding state: while the NREM→Wake transition was reduced ($P < 0.001$), the REM→Wake transition was enhanced (Fig. 1d, e; $P = 0.049$). Thus, unlike the unambiguous suppression of REM sleep by vlPAG GABAergic neurons, their effect on wakefulness is more complex: wakefulness is enhanced relative to REM sleep but suppressed relative to NREM sleep, with an overall reduction in the amount of wakefulness.

Previous studies have shown that lesion of the vlPAG increases REM sleep[34,126,127]. To test the effect of cell-type-specific ablation of GABAergic neurons, we injected into the vlPAG of GAD2-Cre mice Cre-inducible adeno-associated viruses (AAV) expressing pro-Caspase 3 and an enzyme that cleaves pro-Caspase 3 into its active, pro-apoptotic form Caspase 3[130]. Compared to the control GAD2-Cre mice expressing enhanced yellow fluorescent protein (eYFP), the number of GAD2-expressing neurons in the vlPAG was greatly reduced (Supplementary Fig. 3a,b). The amount of REM sleep increased significantly during both the light ($P = 0.009$, $z = 50.0$, Wilcoxon rank-sum test) and dark phases ($P = 0.03$, $z = 0.26$; Supplementary Fig. 3c-i), which was due primarily to an increased frequency of REM sleep episodes (light phase, $P = 0.02$, $z = 0.49$; dark phase, $P = 0.03$, $z = 0.26$; Supplementary Fig. 3f,i). This is consistent with previous lesion studies[34,126,127], and it further supports the role of vlPAG GABAergic neurons in gating REM sleep.

Function of vlPAG projection to dorsolateral pons

The GABAergic projection from the vlPAG to the REM-promoting region in the dorsolateral pons is thought to be important for gating REM sleep[34,71], but its functional contribution has not been tested directly. We injected Cre-inducible AAV expressing ChR2–eYFP into the vlPAG of GAD2-Cre mice and applied laser stimulation in the dorsolateral pons (Fig. 2a). Activation of the vlPAG axons in this region caused a near-complete suppression of REM sleep and strong reduction of wakefulness (Fig. 2b; $P < 0.0001$, bootstrap). The magnitudes of the effects were comparable to those caused by stimulating the vlPAG cell bodies (Fig. 1c), suggesting a strong functional contribution of this projection.

Glutamatergic neurons in the dorsolateral pons are known to be important for REM sleep generation[33–35,128,129]. To test whether these neurons are directly innervated by the vlPAG GABAergic projection, we used RV-mediated trans-synaptic retrograde tracing[108–111,113]. A mutant version of the avian-specific retroviral TVA receptor fused with mCherry (TC^{66t}) and rabies glycoprotein (RG) were expressed by injecting two Cre-inducible AAV vectors (AAV2-*CAG-FLEx-*TC^{66T} and AAV8-*CAG-FLEx-RG*) into the dorsolateral pons of VGLUT2-Cre mice. A modified RV expressing eGFP (RV*dG*-eGFP+EnvA) was injected two weeks later into the same site to infect the cells expressing TC^{66T} and label their presynaptic inputs (Fig. 2c,d). We found a number of eGFP-labeled vlPAG neurons that are GABAergic (Fig. 2h), suggesting that the suppression of REM sleep by vlPAG GABAergic neurons could be partly mediated by their direct inhibition of glutamatergic neurons in the dorsolateral pons.

Since the cholinergic laterodorsal tegmental nucleus (LDT) and noradrenergic locus coeruleus (LC) are also within the projection field of the vlPAG GABAergic neurons, we tested their monosynaptic innervation using RV-mediated retrograde tracing. In both cases, we found eGFP-labeled vlPAG GABAergic neurons (Fig. 2e,i and Fig. 2f,j). Activation of the LDT cholinergic neurons promotes REM sleep[41], while activating the LC noradrenergic neurons promotes wakefulness[44]. Our result suggests that the suppression of REM sleep and wakefulness by vlPAG GABAergic neurons could also be mediated in part by inhibition of the cholinergic and noradrenergic neurons in dorsolateral pons.

Optrode recording from vlPAG GABAergic neurons

To understand how vlPAG GABAergic neurons control the initiation and termination of REM sleep, it is important to characterize their firing rate changes at brain state transitions. Although a powerful method for identifying REM-on and REM-off neurons[34,38,128], c-Fos immunohistochemistry cannot detect activity changes on the time scale of seconds, given the slow time course of c-fos expression. While electrophysiological recordings have been made in the vlPAG previously[125,131,132], it is unclear whether the recorded neurons were GABAergic.

To identify vlPAG GABAergic neurons, we used optogenetic tagging and optrode recording[133]. High-frequency laser pulse trains (15 or 30 Hz, 5-10 ms/pulse, 1 or 0.5 s/train) were applied in the vlPAG of GAD2-Cre mice injected with Cre-inducible AAV expressing ChR2-eYFP. Single units exhibiting reliable laser-evoked spiking with short latencies and high reliability were identified as GABAergic neurons (Fig. 3a and Supplementary Fig. 4; see Methods). The majority

of identified neurons (11/19, 58%) were significantly less active during REM sleep than both NREM sleep and wakefulness ($P < 0.05$, Wilcoxon rank-sum test, post-hoc Bonferroni correction, Fig. 3b-d), consistent with the large number of REM-off GABAergic neurons detected by c-Fos immunohistochemistry[38]. A small number of identified neurons (4/19, 21%) were most active during REM sleep, consistent with the existence of REM-on neurons in this region[38,125,127,132]. Compared to the identified GABAergic neurons, the unidentified cell population contained a lower percentage of REM-off neurons (Supplementary Fig. 5a-d). Interestingly, some neurons in the vlPAG were inhibited by the laser pulses, suggesting that they receive inhibitory inputs from vlPAG GABAergic neurons. This neuronal population contained the highest percentage of REM-on neurons (60%; Supplementary Fig. 5c,d), suggesting that local inhibition of REM-on neurons within the vlPAG also contributes to REM sleep suppression by the GABAergic neurons.

We then analyzed the firing rate changes of these neurons at brain state transitions. The GABAergic REM-off neurons showed a strong firing rate reduction seconds before the onset of REM sleep, which persisted through most of the REM sleep episode (Fig. 3e), suggesting that the silencing of these neurons contributes to natural REM sleep onset and maintenance. In contrast, the REM→wake transition was associated with an abrupt increase in firing rate, consistent with the finding that optogenetic activation of these neurons shortened REM sleep by increasing the transition into wakefulness (Fig. 1d-f). Surprisingly, the NREM→wake transition was also accompanied by a firing rate increase and the wake→NREM transition by a decrease (Fig. 3e, see Discussion). Interestingly, while their firing rates decreased gradually over the course of each NREM sleep episode before the transition to either REM sleep or wakefulness, the overall firing rate was significantly lower during the episodes leading to REM sleep (Fig. 3f; $P = 0.0001$, $T(8) = -7.03$, paired t-test). This is consistent with the finding that NREM episodes with optogenetic activation of the GABAergic neurons were less likely to transition into REM sleep (Fig. 1h); it also indicates that the natural firing rates of vlPAG GABAergic neurons during each NREM episode is predictive of whether the animal will transition into REM sleep or wakefulness. In contrast, the REM-on neurons in the unidentified population showed no firing rate difference between the NREM episodes leading to REM or wakefulness (Supplementary Fig. 5f; $P = 0.31$, $T(10) = 1.06$, paired t-test).

Calcium imaging of vlPAG GABAergic neurons

In addition to optrode recording, we also performed calcium imaging, which allows observation of multiple vlPAG GABAergic neurons simultaneously. AAV was injected into the vlPAG of GAD2-Cre mice for Cre-inducible expression of the calcium indicator GCaMP6f[134]. Imaging was performed in freely moving mice through a gradient refractive index (GRIN) lens coupled to a miniaturized integrated fluorescence microscope[135] (Fig. 4a).

We observed strong variation of the calcium activity across brain states (Fig. 4b). The great majority of imaged neurons exhibited lower activity during REM sleep than NREM sleep or wakefulness (Fig. 4c,d). Analysis at brain state transitions showed a strong activity suppression before the NREM→REM transition and throughout the REM sleep episode, but a rapid increase in activity at wake onset (Fig. 4e). Furthermore, the activity during NREM sleep was significantly lower prior to the transition to REM sleep than to wakefulness (Fig. 4f). Together,

these results confirmed our findings in the optrode recording experiments (Fig. 3), indicating that the great majority of vlPAG GABAergic neurons are REM-off, and the suppression of their activity is closely associated with REM sleep initiation and maintenance.

Slow modulation of vlPAG activity during inter-REM interval

REM sleep in rodents occurs every 10 – 15 min on average in the light phase, following an ultradian rhythm of REM/NREM alternation[122]. Since the vlPAG GABAergic neurons powerfully gate REM sleep, we wondered whether they also play a role in controlling its ultradian timing. Thus, in addition to the rapid activity changes at brain state transitions, we also analyzed their slow modulation during the period between successive REM sleep episodes (inter-REM interval), which consists of both NREM and wake episodes.

First, we temporally compressed each inter-REM interval to unit duration before averaging the vlPAG activity over multiple inter-REM intervals and across multiple REM-off GABAergic neurons. Both optrode recording and calcium imaging revealed a high activity at the beginning of the interval, which decreased slowly but consistently throughout the interval (Fig. 5a, Supplementary Fig. 6a). Interestingly, when we analyzed the activity within NREM and wake states separately during the inter-REM interval, the decrease was significant for NREM (R = -0.48, $P = 2.5 \times 10^{-4}$, $T(53)$ = -3.93, linear regression) but not wake (R = -0.04, P = 0.76, $T(52)$ = -0.29) states (Fig. 5b, Supplementary Fig. 6b). Consistent with this observation, the firing rate was significantly higher in the first than the last NREM episode within each inter-REM interval (Fig. 5c; P = 0.008, $T(10)$ = 3.28, paired t-test; Supplementary Fig. 6c), but no significant difference was found for the wake episodes (Fig. 5d, P = 0.15, $T(10)$ = 1.56; Supplementary Fig. 6d;). Furthermore, when the activity was averaged across all NREM or wake episodes, the decrease was apparent within a single NREM but not wake episode (Fig. 5e; NREM, R = -0.65, $P = 2.8 \times 10^{-15}$, $T(108)$ = -8.77; wake, R = 0.21, P = 0.027, $T(108)$ = 2.24; Supplementary Fig. 6e). These findings suggest that the slow process modulating vlPAG activity during each inter-REM interval operates selectively during NREM sleep. Given the strong REM suppression effect of vlPAG GABAergic neurons (Fig. 1), the slow decrease of their firing rates could gradually enhance the propensity of the next REM episode and thus regulate the ultradian timing of the REM/NREM alternation. In contrast, the REM-on neurons in the unidentified population showed no consistent change in their NREM or wake activity during the inter-REM interval (Supplementary Fig. 7; NREM, R = 0.13, P = 0.33, $T(58)$ = 0.99; wake, R = -0.17, P = 0.19, $T(58)$ = -1.32; linear regression).

Homeostatic regulation of REM sleep and vlPAG activity

The duration of the inter-REM interval is highly variable in rodents, and in the rat it was found to be correlated with the duration of the preceding REM episode[136,137]. Here we found a similar relationship in the mouse (Fig. 6a; R = 0.39, $P = 6.8 \times 10^{-36}$, $T(970)$ = 13.03, linear regression). Such a correlation suggests that the inter-REM interval is under homeostatic regulation, in which REM sleep pressure accumulated during inter-REM intervals is partially dissipated by each REM sleep episode[30,31]; a longer episode causes stronger dissipation of the pressure and thus requires a longer interval for accumulation before the next REM episode.

Consistent with this notion, we found that shortening of REM episode duration by closed-loop optogenetic activation of vlPAG GABAergic neurons (see Methods; $P = 0.002$, $T(5) = 5.88$, paired *t*-test) also led to a significant shortening of the subsequent inter-REM interval, likely due to a reduced dissipation of REM sleep pressure (Fig. 6c; $P = 0.003$, $T(5) = -5.29$, paired *t*-test). We then examined the effect of each REM episode on the NREM activity of vlPAG GABAergic neurons. Compared to the pre-REM activity, the NREM activity following a REM episode was significantly elevated (Fig. 6d; $P = 0.006$, $T(10) = -3.43$, paired *t*-test; Supplementary Fig. 8a), suggesting that a single REM episode can reset the firing rate of vlPAG GABAergic neurons, which has been decreasing slowly during the preceding inter-REM interval. In contrast, we found no significant difference in NREM activity before and after a single wake episode (Fig. 6e; $P = 0.41$, $T(10) = 0.84$, paired *t*-test; Supplementary Fig. 8b), suggesting that the firing rate reset is specific to REM sleep. The post-REM activity of vlPAG GABAergic neurons was higher following long (> 90 s) REM episodes than following short (≤ 90 s) REM episodes (Fig. 6f; $P = 0.03$, $T(22) = -1.80$, paired *t*-test; Supplementary Fig. 8c), and the mean firing rate during the inter-REM interval was significantly correlated with the preceding REM episode duration (Fig. 6g; $P = 0.001$, $T(38) = 3.58$, linear regression; Supplementary Fig. 8d). These results point to a strong parallel between the modulation of vlPAG GABAergic neuron activity and the accumulation and dissipation of REM sleep pressure. Finally, we found a strong correlation between the duration of the inter-REM interval and the vlPAG firing rate during the interval (Fig. 6h; $P = 1.6 \times 10^{-5,}$ $T(38) = 4.95$; Supplementary Fig. 8e). This is consistent with the finding that higher vlPAG activity is associated with lower propensity for REM sleep (Figs. 1d-g, 3c,d, 4a-c), and it suggests that the modulation of vlPAG activity by prior sleep history can mediate homeostatic regulation of REM sleep.

Discussion

Using optogenetic manipulation and caspase 3-mediated cell ablation, we found that vlPAG GABAergic neurons powerfully suppress REM sleep. Activation of these neurons greatly reduced both NREM→REM transitions and REM sleep maintenance while consolidating NREM sleep (Fig. 1), which are likely mediated in part by their projection to the dorsolateral pons (Fig. 2). Optrode recording and calcium imaging showed that their activity was strongly suppressed at the onset of each REM sleep episode and increased abruptly at its termination (Figs. 3, 4), consistent with their functional role in gating REM sleep. In addition to the rapid changes at brain state transitions, their activity was also modulated on a timescale of minutes. The dependence of their firing rates on sleep history closely parallels the accumulation and dissipation of REM sleep pressure (Figs. 5, 6). These results support the notion that REM sleep onset and termination are controlled by fast synaptic inhibition from vlPAG GABAergic neurons to REM-promoting neurons in the pons, whereas the ultradian timing of REM sleep is regulated by a homeostatic process acting through slow modulation of vlPAG GABAergic activity.

The strong suppression of vlPAG activity during REM sleep (Figs. 3e, 4e) could be mediated in part by inhibitory inputs from REM-active neurons. In addition to the small number of REM-on neurons within the vlPAG[38] (Figs. 3c, d, 4c, d, red), which could locally inhibit the REM-off neurons, REM-active GABAergic neurons in the pons, ventral and dorsal medulla, lateral hypothalamus, and preoptic area have all been shown to project to the vlPAG[31,34,138]. In particular, rabies-mediated trans-synaptic retrograde tracing has shown that GABAergic neurons in the ventrolateral medulla, which powerfully promote REM sleep, directly innervate GABAergic vlPAG neurons[31]. Optogenetic activation of these axon projections promoted REM sleep at a magnitude similar to that of activating the medulla neuron cell bodies, suggesting that inhibition of the vlPAG REM-off neurons is a major mechanism promoting REM sleep. Surprisingly, the REM-off vlPAG neurons were most active during wakefulness (Figs. 3, 4), even though their optogenetic activation increased NREM sleep and decreased wakefulness (Figs. 1, 2). One of the excitatory inputs driving their wake activity may be the projection from orexin/hypocretin neurons in the hypothalamus[34], which are most active during wakefulness[139], and vlPAG GABAergic neurons are known to express orexin/hypocretin receptors[127]. Given the power of vlPAG GABAergic neurons in suppressing REM sleep (Fig. 1), this input may effectively prevent unwanted intrusions of REM sleep into wakefulness. Although superficially the high wake activity of vlPAG GABAergic neurons may seem incompatible with the wake-suppressing effect of their optogenetic activation (Fig. 1), we note that the effect was primarily due to an enhanced NREM sleep maintenance. The low efficacy of these neurons in inducing wake→NREM transitions (Fig. 1f) may allow other wake-promoting neurons to counteract the high firing rates of the vlPAG neurons to maintain wakefulness. On the other hand, activation of these neurons was highly effective in reducing NREM→wake transitions (Fig. 1f); the increase in their natural firing rates at this transition indicates that natural awakening from NREM sleep is not due to, but in spite of, the firing rate change of vlPAG GABAergic neurons.

To account for the ultradian alternation between REM and NREM sleep, the first circuit model emphasized reciprocal interactions between cholinergic REM-on and monoaminergic REM-off neurons[140]. Subsequent studies have highlighted the importance of GABAergic inhibition between REM-on and REM-off neurons[31,34,138]. Although fast GABAergic interactions can

account for rapid transitions between brain states, they are insufficient to explain the temporal dynamics of NREM/REM alternation on a time scale of minutes (rodents) to hours (humans); a separate, slow-varying process is required[141,142]. Here, in addition to confirming the correlation between the REM episode duration and subsequent inter-REM interval in mice (Fig. 6a), we found that shortening of REM sleep episodes through an optogenetic manipulation also shortened the subsequent inter-REM interval (Fig. 6c). These findings support the notion that the ultradian timing of REM sleep is strongly regulated by a homeostatic pressure that accumulates on a time scale of minutes and is partially dissipated by each REM sleep episode[137,142,143]. Interestingly, pharmacogenetic manipulations that shortened/prolonged REM sleep duration also decreased/increased the EEG delta power in subsequent NREM sleep[32], suggesting that in addition to dissipating REM sleep pressure, REM sleep also contributes to the accumulation of NREM sleep pressure.

At the neuronal level, we found that vlPAG GABAergic neuron activity decreased gradually during the inter-REM interval (**Fig. 5**) and was reset by each REM episode, the magnitude of which depended on the episode duration (**Fig. 6**). These firing rate modulations mirror the accumulation and dissipation of REM sleep pressure[137,143], and implementation of such slow modulations of REM-off neurons in circuit models can account for the temporal dynamics of REM/NREM alternations[141,142]. Previous studies have shown that REM sleep deprivation for several hours decreased/increased the activity of REM-off/REM-on neurons[144] and increased the expression of brain-derived neurotrophic factor (BDNF) in the pons[145,146]. It would be interesting to know whether these processes also operate on a time scale of minutes, and whether they are causally linked to the firing rate modulations in vlPAG neurons (Figs. 5, 6). Our results suggest that an important mechanism through which the homeostatic process regulates REM sleep timing is the slow modulation of vlPAG GABAergic neurons that powerfully gate REM sleep.

Materials and Methods

Animals

All experimental procedures were approved by the Animal Care and Use Committee at the University of California, Berkeley. Optogenetic manipulation experiments were performed in male or female GAD2-Cre (Jackson Laboratory stock 010702) and VGLUT2-Cre (016963) mice. Optrode recording, calcium imaging, lesion, and rabies-mediated trans-synaptic tracing experiments were all performed in male or female GAD2-Cre, VGLUT2-Cre, TH-Cre(008601), and ChAT-Cre (006410) mice. Animals were housed on a 12-h dark/12-h light cycle (light on between 7:00 and 19:00). Animals with implants for EEG/EMG recordings, optogenetic stimulation, optrode recordings or calcium imaging were housed individually. Mice injected with viruses for trans-synaptic tracing were housed in groups of up to 6 animals.

Surgical Procedures

Adult (6- to 12-week-old) mice were anaesthetized with isoflurane (3% induction, 1.5% maintenance) and placed on a stereotaxic frame. Body temperature was kept stable throughout the procedure by using a heating pad. After asepsis, the skin was incised to expose the skull, and the overlying connective tissue was removed. For access to the vlPAG, a craniotomy (1 mm diameter) was made on top of the right superior colliculus (4.6-4.8 mm posterior to the bregma, 0.6–0.7 mm lateral). AAV2-EF1a-FLEX-ChR2–eYFP, AAV2-EF1a-FLEX–eYFP (produced by University of North Carolina Vector Core), AAV1-Syn-Flex-GCaMP6f (University of Pennsylvania Vector Core), or AAV-DJ-EF1a-FLEX-ChR2–eYFP (University of Stanford Gene Vector and Virus Core) was loaded into a sharp micropipette mounted on a Nanoject II or Nanoject III and injected slowly at a depth of 2.5 mm from the brain surface (300-500 nl, unilateral). An optical fiber (0.2 mm diameter) was inserted with the tip 0.2 mm above the virus injection site. To stimulate axon projections of vlPAG GABAergic neurons in the dorsolateral pons, the optical fiber was implanted within the pons (5.2-5.3 mm posterior to bregma, 0.9 mm lateral, 3.0 mm depth). For cell-type specific lesion experiments, rAAV2-Flex-taCasp3-Tevp (University of North Carolina Vector Core) was injected bilaterally into the vlPAG (200 - 300 nl). For optogenetic experiments, data from animals where the tip of the optical fiber was not within the aimed location were excluded. For lesion experiments, data from animals where virus expression was not restricted to the vlPAG were excluded.

For EEG and EMG recordings, a reference screw was inserted into the skull on top of the left cerebellum. EEG recordings were made from two screws, one on top of hippocampus (about 2 mm posterior to bregma) and one on top of the prefrontal cortex (about 1mm anterior to bregma). Two EMG electrodes were inserted into the left and right neck muscles. For EEG/EMG recordings in differential mode, four screws were fixed on the skull, two posterior and two anterior of bregma. All screws, electrodes, microdrives, connectors and GRIN lenses required for EEG/EMG recordings, optrode recordings and calcium imaging were secured to the skull using dental cement.

Rabies Virus Tracing

For retrograde tracing, AAV-CAG-FLEx^{loxP}-TC^{66T} (1.0×10^{12} gc/mL) and AAV8-CAG-FLEx^{loxP}-RG (1.8×10^{12} gc/mL) was mixed at a 1:1 ratio and stereotaxically injected. For tracing from glutamatergic neurons in the dorsolateral pons, 100 nl was injected into VGLUT2-Cre mice at -5.3 mm AP, 0.8 mm ML, 3.3 mm DV, unilaterally. For tracing from the LDT, 300-500 nl was injected in ChAT-Cre mice at -5.2 mm AP, 0.7 mm ML, 3.2 mm DV, bilaterally. For tracing from the noradrenergic neurons in the LC, 200-300 nl was injected into TH-Cre mice at -5.34 mm AP, 0.8 mm ML, 3.2 mm DV, unilaterally. Two weeks after the AAV injection, 300-400 nl of RV*dG*-eGFP+EnvA (1.0×10^{9} cfu/mL) was injected into the same location. The injection pipette for AAV was tilted at 20 degrees from vertical while the injection pipette for RV was inserted vertically to limit virus coinfection along a common injection tract. We excluded animals with inefficient trans-synaptic labeling indicated by fewer than 30 rabies-GFP labeled cells detected outside of the injection site.

Histology and Immunohistochemistry

Mice were deeply anesthetized and transcardially perfused with 0.1M PBS followed by 4% paraformaldehyde in PBS. After removal, brains stayed overnight in 4% paraformaldehyde. For cryoprotection, brains were stored in 30% sucrose (w/v) in PBS solution for at least one night. Brains were sliced in 30 or 40 μm sections using a cryostat (Leica). For immunohistochemistry, non-specific binding sites were blocked by incubating the brain sections in 2% goat serum (Millipore) in PBST (0.3% Triton X-100 in PBS).

To amplify the fluorescence of axon fibers expressing ChR2-eYFP or eYFP we applied antibodies for GFP (A11122, Life technologies, 1:1000). Brain sections were incubated with the primary antibody diluted in blocking solution for two nights. A species-specific secondary antibody conjugated with green Alexa fluorophore (A11008, Life technologies, 1:1000; goat anti rabbit) was diluted in PBS and applied for 2 hrs. Fluorescence images were taken using a confocal microscope (LSM 710 AxioObserver Inverted 34-Channel Confocal, Zeiss), fluorescence microscope (Keyence, BZ-X710) and Nanozoomer 2.0 RS (Hamamatsu).

Fluorescence In Situ Hybridization

FISH was performed to detect GAD2 mRNA. Brains were embedded and mounted with Tissue-Tek OCT compound (Sakura finetek) and 30 μm sections were cut using a cryostat (Leica). FISH was performed using an RNAscope assay according to the manufacturer's instructions (RNAscope® Fluorescent Multiplex Reagent Kit, Cat # 320850, Advanced cell Diagnostics). Sections were hybridized with a GAD2 probe (Mm-Gad2, 439371) and eGFP probe (EGFP-C3, 400281-C3), and amplification steps were carried out followed by Hoechst staining. Fluorescence images were taken using a confocal microscope (LSM 710 AxioObserver Inverted 34-Channel Confocal, Zeiss) or a fluorescence microscope (BZ-X700, Keyence).

Polysomnographic Recordings

EEG and EMG electrodes were connected to flexible recording cables via a mini-connector, and recordings were made in the animal's home cage placed in a sound-attenuated box. Recordings started after at least 1 h of habituation. The signals were recorded with a TDT RZ5 amplifier (bandpass filter, 1–750 Hz; sampling rate, 1,500 Hz) or an A-M Systems amplifier (sampling rate, 600 Hz). For the recordings using the TDT amplifier, EEG and EMG signals were referenced to a common ground screw, place on top of the cerebellum. Recordings with the A-M Systems amplifier were made in differential mode. We used the difference between the voltage potentials recorded from an anterior (on top of prefrontal cortex) and posterior screw (on top of hippocampus) as EEG signal and the difference between the potentials from the two EMG electrodes as EMG signal.

To determine the brain state from the recorded EEG and EMG signals, we first calculated the power spectrum for the EEG and EMG signals using 5s sliding windows, sequentially shifted by 2.5s increments. Next, we summed the EEG power in the range from 1 to 4 Hz and 6 to 12 Hz, yielding time-dependent delta and theta power. For further analysis, we computed the theta/delta power ratio. We also summed the EMG power in the range 20 - 300 Hz. As a first step, we determined for each time point the brain state using an automated threshold algorithm. We first determined a threshold for the delta power (delta threshold), separating the typically bimodal distribution of the delta power into a lower and higher range. A state was assigned as NREM sleep if the delta power was larger than the delta threshold. A state was classified as REM if (1) the delta power was lower than the delta threshold, (2) the theta/delta ratio was higher than one standard deviation above the mean, and (3) the EMG power was lower than its mean. All remaining states were classified as wake. The wake state thus encompassed states with high EMG power (active awake) or low delta power but without elevated EMG activity or theta/delta ratio (quiet awake). Finally, we manually verified the automatic classification using a custom-built graphical user interface programmed in Matlab.

Optogenetic Stimulation

We performed optogenetic activation experiments 4 to 6 weeks after injection of AAV expressing ChR2. Experiments were performed in the afternoon (12:00 and 19:00) and lasted at least 6 hours. For optogenetic stimulation of GABAergic vlPAG neurons, each trial consisted of a 20 Hz pulse train lasting for 300 s using a blue 473-nm laser (6-8 mW at fiber tip, Shanghai Laser). The inter-trial interval was randomly chosen from a uniform distribution from 15 to 25 min.

To test the role of vlPAG GABAergic neurons in REM sleep maintenance, we applied a closed-loop stimulation protocol. Sleep/wake states were classified based on EEG and EMG in real time. When REM sleep was detected, the laser was turned on with 50% probability, and turned off only when the REM episode ended. This allowed comparison of the REM episode durations and the subsequent inter-REM intervals with and without laser stimulation within the same recording session.

Transition Analysis

To quantify transition probabilities between brain states, we discretized time into 20 s bins and aligned all laser stimulation trials from all *N* mice by the onset of laser stimulation at time 0.

To determine the transition probability from state *X* to *Y* for time bin *i*, $P_i(Y|X)$, we first determined the number of trials (*n*) in which the animal was in brain state *X* during the preceding time bin *i-1*. Next, we identified the subset of these trials (*m*) in which the animal transitioned into state *Y* in the current time bin *i*. The transition probability $P_i(Y|X)$ was computed as *m/n*. In Fig. 1d, each bar represents the transition probability averaged across three consecutive 20 s bins. To compute the baseline transition probabilities, we averaged across all time bins excluding the laser stimulation period and the 2 min period following laser stimulation.

Ablation of vlPAG GABAergic neurons

To test the impact of ablating vlPAG GABAergic neurons, we recorded the EEG and EMG of mice expressing pro-Caspase3 in the vlPAG, two to three weeks after virus injection. Each mouse was habituated for at least one day, and sleep-wake behavior during the light or dark cycle was recorded for at least two days. For control, we recorded from mice expressing eYFP that underwent identical procedures.

Optrode Recording

To record single unit activity from vlPAG GABAergic neurons, we used custom-built optrodes, consisting of 12 - 14 microelectrodes (Stablohm 675, California Wire Company) twisted into stereotrodes or tetrodes and attached to an optic fiber (0.2 mm diameter). The electrodes were inserted into a screw-driven microdrive and soldered to a 2x10 connector. For EEG/EMG recordings two additional wires were attached to the connector. For stability, all components were attached to a custom-designed circuit board (fabricated by oshpark.com). The tips of the electrodes were electro-plated in a gold solution (Sifco 5355) mixed with 0.1% PEG solution (Sigma). Each electrode was plated iteratively, till reaching an impedance of 500-800 kΩ. Neurophysiological signals were recorded using a TDT RZ5 amplifier (Tucker-Davis Technologies) at a sampling rate of 25 kHz and bandpass filtered (0.3-8 kHz). The optrode was slowly lowered in 50 μm steps to search for well-separated, light-responsive units. Recordings were performed during the light cycle and lasted for at least 60 min. For each mouse, recordings were carried out over a period of 1-2 months, starting 3 weeks after virus injection.

Before euthanizing the animal, an electrolytic lesion was made to mark the end of the electrode tract by passing a current (100 μA, 10s) through two electrodes. Based on the location of the lesion and the optrode tract, the anatomical location of each unit was reconstructed. We excluded units whose anatomical location was outside the vlPAG.

Spike Sorting

Spikes were sorted offline based on the waveform energy, the three largest principal components for each spike waveform on each stereotrode or tetrode channel, and a further parameter measuring for each potential unit the distance between spontaneous and laser evoked waveforms (as quantified by the inner product). Single units were identified either manually using the software Klusters (http://neurosuite.sourceforge.net) or automatically using the software KlustaKwik (http://klustakwik.sourceforge.net). Only units with a clear refractory period in the auto-correlogram and satisfying criteria for isolation distance (>20) and L-ratio (<0.15) were included in the data set. The median values of the isolation distance and L-ratio for all units were 36.9 and 0.022. Two units recorded with the same stereotrode or tetrode on different days were counted as the same unit, if their waveforms were similar, their recording depths differed by less than 100 μm, and if their average firing rates were not significantly different.

Optogenetic Tagging

To identify ChR2-expressing vlPAG GABAergic neurons, high-frequency laser pulse trains (15 and 30 Hz with durations of 1 and 0.5 s, respectively) were delivered every minute. In a subset of recordings we presented a 0.2 s long step pulse instead of the 15 Hz pulse train. The recorded units were classified into three categories (identified GABAergic units, laser-inhibited or laser-unmodulated units) using the following approach: First, we tested whether the activity of each unit was significantly modulated by single laser pulses using a previously developed statistical test (SALT)[147]. This method probes whether the distribution of spike patterns (within 30 ms windows) elicited by single laser pulses is different from spontaneous spike patterns. Second, to determine whether a significantly modulated unit was excited or inhibited by laser stimulation, we tested whether the average firing rate during the 30 Hz laser pulse train was significantly increased or decreased relative to the firing rate in the 0.5 s window preceding laser stimulation ($P < 0.05$, Wilcoxon signed-rank test). Finally, among those that are excited by the laser stimulation, we identified units that followed each laser pulse with short first-spike latency (<10 ms) and high reliability (> 0.4) as GABAergic units. We excluded units exhibiting longer latencies or lower reliabilities. Units that were inhibited or not significantly modulated by laser stimulation were summarized as un-identified.

Behavioral Monitoring

To identify the awake behaviors during which vlPAG GABAergic units are activated, we made video recordings (sampling rate of 5Hz) using a camera placed on top of the mouse cage along with the electrophysiological signals. Active behaviors were divided into five categories: Eating, grooming, moving, running and quiet wake. The behavioral scoring was performed manually using a custom written graphical user interface (programmed in MATLAB).

Firing Rate Calculation

After spike sorting, the activity of each unit was represented as a spike train (sequences of 0s and 1s) with 0.67 ms time resolution. For firing rate calculation, spike trains were

downsampled to 2.5 s time bins aligned with the brain state annotation. To reduce noise, spike trains were filtered with an exponential kernel with a time constant of 7.5 s. To quantify the firing rate dynamics during each sleep or wake episode, we normalized the length of each episode by dividing it to a fixed number of bins, allowing us to average the across episodes and neurons.

Calcium Imaging

Calcium imaging experiments were performed 3 to 8 weeks following injection of AAV expressing GCaMP6. Imaging sessions took place during the light cycle in the home cage placed within a sound-attenuated chamber. The animal was briefly anesthetized with isoflurane to secure the microscope to the baseplate and to focus it to a given field of view. The animal was then allowed to recover from anesthesia and habituate in their home cage for at least 30 minutes prior to imaging. Calcium activity was acquired using the nVista hardware and nVista HD software (Inscopix), with a 10 Hz image acquisition rate using 0.2-0.7 mW illumination. An Intan RHA2000 system (Intan Technologies) was used to simultaneously record EEG and EMG activity (bandpass filter , 1–750 Hz; sampling rate, 25 kHz). An output signal (20 Hz) delivered from the Inscopix system to the Intan system throughout the recording session was used to synchronize the timing between the imaging and EEG/EMG recordings. Recording sessions lasted between 40-110 min and were repeated up to 6 times per animal, spanning across 5 different days.

Calcium Imaging Analysis

Imaging data were processed in Python and Matlab (Mathworks). First, the acquired images were spatially downsampled by a factor of 4. To correct for lateral motion of the brain relative to the GRIN lens, we applied an algorithm based on a previous study[148]. We created a high-pass filtered image stack by calculating the difference between the image stack and a spatially lowpass filtered version of the image stack. A high-contrast region of the mean projection of the high-pass filtered image stack was selected as a reference. The spatial shift that maximized the cross-correlation between the reference region and each frame of the high-pass filtered image stack was calculated to obtain the motion corrected images.

Regions of interest (ROIs) were selected using a graphical user interface (programmed in Python) by manually identifying cell-body sized regions with fluorescence activity across time, and defining the coordinates of a polygon that contains the pixels of the ROI. The pixel intensities within each ROI were averaged to create a fluorescence time-series. In cases where the same ROI was identified across imaging sessions, the ROI was grouped together for analysis. To correct for contamination of the fluorescence signal by out-of-focus neuropil, we calculated the neighboring neuropil signal, $F_{neuropil}$, from a bordering concentric ring with 20 μm distance from the perimeter of each ROI, excluding other ROIs, and subtracted $F_{neuropil}$, scaled by a correction factor, cf , from the raw ROI signal, F_{raw} ($F_{neuropil\text{-}subracted} = F_{raw} - cf * F_{neuropil}$). The correction factor for each recording session was estimated by calculating the ratio between the mean pixel intensity of a manually selected blood vessel, $F_{blood\ vessel}$, and a nearby region lacking an ROI signal, $F_{near\ blood\ vessel(no\ ROI)}$, each subtracted by the mean pixel intensity of an off-lens

region, $F_{off\text{-}lens}$ ($cf = [F_{blood\ vessel} - F_{off\text{-}lens}] / [F_{near\ blood\ vessel(no\ ROI)} - F_{off\text{-}lens}]$). In cases where a blood-vessel was not clearly present, the mean value obtained from other animals, $cf = 0.55$, was used. The baseline of each neuropil-subtracted fluorescence time-series was estimated by calculating the best linear fit using periods of low fluorescence activity, represented by the 20th percentile of each recording session. Slope values were typically smaller than zero and thus allowed compensating for a drift in the fluorescence signal due to photobleaching of GCaMP.

Statistics

For optogenetic and ablation experiments, GAD2-Cre mice were randomly assigned to control (injected with AAV expressing eYFP) and experimental groups (injected with AAV expressing ChR2-eYFP or Casp3). No randomization was used for rabies-mediated trans-synaptic tracing. Investigators were not blinded to animal identity and outcome assessment. All statistical tests (paired *t*-test, Wilcoxon rank-sum test, Wilcoxon signed-rank test, bootstrap) were two-sided. For both paired and unpaired tests, we ensured that the variances of the data were similar between the compared groups. For *t*-tests, we verified that the data were normally distributed using Lilliefors test for normality.

The 95% CIs for brain state percentages and transition probabilities (Figs. 1c,d, 2a) were calculated using a bootstrap procedure. For an experimental group of *n* mice, we calculated the CI as follows: we repeatedly resampled the data by randomly drawing for each mouse *p* trials (random sampling with replacement). For each of the *m* iterations, we recalculated the mean brain state percentages or transition probabilities across the *n* mice. The lower and upper CIs were then extracted from the distribution of the *m* resampled mean values. To test whether a given brain state or transition probability was significantly modulated by laser stimulation, we calculated for each bootstrap iteration the difference between the averaged brain state percentages or transition probabilities during laser stimulation and the corresponding baseline values for periods without laser stimulation. From the resulting distribution of difference values, we then calculated a *P* value to assess whether laser stimulation significantly modulated brain states or transitions between brain states.

Sample Sizes

For optogenetic activation experiments, cell-type specific ablation experiments and *in vivo* recordings (optrode recordings and calcium imaging), we continuously increased the number of animals until statistical significance was reached to support our conclusions. For rabies-mediated and anterograde tracing experiments, the selection of the sample size was based on numbers reported in previous studies. For optrode recordings, we first recorded a preliminary data set of 6 units from two mice. Based on analysis of this data set and given the success rate in finding identified GABAergic units, we predicted that about 20 units are sufficient to statistically support our conclusions.

Figure Legends

Figure 1 Optogenetic activation of vlPAG GABAergic neurons suppresses REM sleep and wakefulness while enhancing NREM sleep. (**a**) Schematic of optogenetic experiment. Top, coronal diagram of mouse brain; Bottom, fluorescence image of PAG (dashed box in schematic) in a GAD2-Cre mouse injected with AAV expressing ChR2–eYFP (green). Blue, 49,6-diamidino-2-phenylindole (DAPI). Scale bar, 500 μm. (**b**) Example experiment. Shown are EEG power spectrogram, EMG amplitude, and brain states (color coded). Blue shading, laser stimulation period (20 Hz, 300 s). (**c**) Average EEG spectrogram (top, normalized by the mean power in each frequency band) and percentage of wake, NREM or REM states (bottom) before, during, and after laser stimulation, averaged across all trials from 12 mice. Laser stimulation significantly increased NREM sleep ($P < 0.0001$, bootstrap) and decreased wakefulness ($P < 0.0001$) and REM sleep ($P < 0.0001$). Shading, 95% confidence intervals (CI). Blue stripe, laser stimulation period (20 Hz, 300 s). (**d**) Effect of laser stimulation on transition probability between each pair of brain states. Each bar represents transition probability within each 20 s period. Error bar, 95% CI (bootstrap). Red line and shading, baseline transition probability and 95% CI. N, NREM; R, REM; W, wake. W→R and R→N transitions are omitted because they were rarely detected with or without laser stimulation. (**e**) Diagram summarizing transition probabilities that are significantly increased (magenta) or decreased (cyan) by laser stimulation. (**f**) Cumulative probability of transition between each pair of brains states within 120 s with (blue) or without (gray) laser stimulation. Laser stimulation caused a substantial decrease in NREM→REM ($P < 0.001$, bootstrap) and NREM→wake ($P < 0.001$) transitions, increase in REM→wake transition ($P < 0.001$), and only minor increase in wake→NREM transition ($P = 0.028$). Shading, 95% CI. (**g**) Mean REM (left) and NREM (right) episode duration for episodes overlapping (blue) or non-overlapping (gray) with optogenetic activation of vlPAG GABAergic neurons ($n = 12$ mice). Each line, data from one mouse. *$P < 0.05$, Wilcoxon signed-rank test. Error bar, ±s.d. (**h**) Percentage of NREM episodes followed by REM, in episodes overlapping (blue) or not overlapping (gray) with laser stimulation. *$P < 0.05$, **$P < 0.01$, Wilcoxon singed-rank test. Error bar ±s.d.

Figure 2 Inhibition of dorsolateral pons by vlPAG GABAergic projection suppresses REM sleep and wakefulness while promoting NREM sleep. (**a**) Left, schematic depicting ChR2-mediated activation of GABAergic axons projecting from the vlPAG to the dorsolateral pons. ChR2-eYFP was expressed in the vlPAG of GAD2-Cre mice and an optic fiber was implanted into the dorsolateral pons. Right, coronal diagram of mouse brain at the position indicated by vertical dashed line in the schematic (top) and fluorescence image (bottom) of dorsolateral pons (black box in diagram) in a GAD2-Cre mouse injected with AAV expressing ChR2–eYFP (green) into the vlPAG. Blue bar depicts the placement of the optic fiber. Blue, 49,6-diamidino-2-phenylindole (DAPI). Scale bar, 500 μm. (**b**) Top, normalized EEG spectrogram. Bottom, percentage of REM, NREM or wake states (bottom) before, during, and after laser stimulation of GABAergic axons ($n = 5$). (**c**) Schematic showing rabies-mediated trans-synaptic tracing. TC^{66T}, mutant EnvA receptor fused with mCherry; RG, rabies glycoprotein; RV*dG*, RG-deleted rabies virus. (**d**) Top, fluorescence image of dorsolateral pons in a VGLUT2-Cre mouse. Scale bar, 200 μm. Bottom, enlarged view of region in white box showing starter cells. Yellow, neurons expressing both GFP and mCherry (arrowheads). Scale bar, 20 μm. Scp, superior cerebellar peduncle. (**e**) Top, fluorescence image of the LDT in a ChAT-Cre mouse. Scale bar, 200 μm.

Bottom, enlarged view of region in white box showing starter cells (yellow, arrowheads). Scale bar, 20 μm. (**f**) Top, fluorescence image of dorsolateral pons in a TH-Cre mouse. Scale bar, 200 μm. Bottom, enlarged view of region in white box showing starter cells (yellow, arrowheads). Scale bar, 20 μm. (**g**) Coronal diagram of mouse brain. The vlPAG is indicated by the black box. Aq, aqueduct. (**h**) vlPAG GABAergic (GAD2) neurons innervating glutamatergic (VGLUT2) neurons in the dorsolateral pons. Top, fluorescence image showing rabies-GFP labeled (green) and GAD2 positive neurons in the vlPAG. 41% (317/782) of rabies-labeled cells were GAD2 positive (n = 3 mice). Red, FISH for mRNA encoding GAD2. Blue, DAPI. Scale bar, 200 μm. Bottom, enlarged view of the white box showing GFP-labeled neurons expressing GAD2 (arrowheads). Scale bar, 30 μm. (**i**) Similar to (**h**), for vlPAG GABAergic neurons innervating cholinergic (ChAT) neurons in the LDT. 34% (33/96) of rabies-labeled cells were GAD2 positive (n = 3 mice). (**j**) Similar to (**h**), for vlPAG GABAergic neurons innervating noradrenergic (TH) neurons in the LC. 56% (83/148) of rabies-labeled cells were GAD2 positive (n = 3 mice).

Figure 3 Firing rates of identified vlPAG GABAergic neurons across brain states. (**a**) Example unit. Left, raw trace showing spontaneous and laser-evoked spikes. Blue ticks, laser pulses (15 Hz). Scale bars, 100 ms, 0.5 mV. Middle, comparison between laser-evoked (blue) and averaged spontaneous (red) spike waveforms from this unit. Scale bars, 0.2 ms, 0.5 mV. Right, Spike raster showing multiple trials of laser stimulation at 30 Hz. Scale bar, 100 ms. (**b**) Firing rates of an example vlPAG GABAergic neuron. (**c**) Firing rate modulation of 19 identified units from 6 mice. W, wake; R, REM; N, NREM. Blue, significant REM-off neurons ($P < 0.05$, Wilcoxon rank-sum test, post-hoc Bonferroni correction); red, significant REM-on neurons; gray, other neurons. (**d**) Firing rates of significant REM-off (left) and REM-on (red) neurons during different brain states. Each line shows firing rates of one unit; gray bar, average across units. (**e**) Average EEG spectrogram (upper, normalized by the mean power in each frequency band) and mean firing rate (z-scored) of significant REM-off neurons (lower) at brain state transitions. Shading, ±s.e.m. (**f**) Firing rates during NREM episodes preceding wake were significantly higher than those preceding REM episodes ($P = 0.0001$, $T(8) = -7.03$, paired t-test).

Figure 4 Sleep-wake activity of vlPAG GABAergic neurons measured with calcium imaging. (**a**) Left, schematic of calcium imaging through GRIN lens. Middle, field of view of an example imaging session. Right, pixel-wise activity map of an example imaging session. Red line, four example ROIs. Scale bar: 100 μm. (**b**) EEG power spectrogram, EMG trace, color-coded brain state, and ΔF/F traces of the ROIs outlined in (**a**). (**c**) Activity modulation of 31 ROIs from 3 mice. W, wake; R, REM; N, NREM. Blue, significant REM-off ROIs ($P < 0.05$, Wilcoxon rank-sum test, post-hoc Bonferroni correction); red, significant REM-on ROIs; gray, other neurons. (**d**) Calcium activity of significant REM-off (left) and REM-on (red) ROIs during different brain states. Each line shows activity of one ROI; gray bar, average across ROIs. (**e**) Average EEG spectrogram (upper, normalized by the mean power in each frequency band) and mean calcium activity (ΔF/F, z-scored) of significant REM-off ROIs (lower) at brain state transitions (n = 23). Shading, ± s.e.m. (**f**) The mean calcium activity during NREM episodes preceding wake was significantly higher than those preceding REM episodes ($P = 0.003$, $T(22) = -3.24$, paired t-test).

Figure 5 Slow modulation of vlPAG GABAergic neuron activity during inter-REM interval. (**a**) Average normalized EEG spectrogram (upper) and mean firing rate (z-scored) of significant

REM-off vlPAG GABAergic neurons (lower) during two successive REM episodes and the inter-REM interval. Each REM episode and inter-REM interval was temporally compressed to unit length before the firing rates were averaged over multiple episodes/intervals and across GABAergic REM-off neurons (n = 11). Shading, ±s.e.m. (**b**) Firing rate (FR, z-scored) during NREM (left) and wake (right) episodes within different segments of the inter-REM interval. Each inter-REM interval was divided into 5 equally sized bins, and NREM or wake firing rates were averaged within each bin. Each symbol represents the average NREM or wake firing rate of a unit. The average NREM firing rate decreased during the inter-REM period (R = -0.48, P = 2.5×10^{-4}, $T(53)$ = -3.93, linear regression), while the wake activity showed no significant trend (R = -0.04, P = 0.76, $T(52)$ = -0.29). Black line, average firing rate of each bin. (**c**) Mean firing rates during the first (light gray) and last (dark gray) NREM episodes of each inter-REM interval. Each NREM episode was temporally compressed to unit duration before the z-scored firing rate was averaged over episodes and across cells. The firing rate during the first NREM period was significantly higher than during the last period (n = 11 units, P = 0.008, $T(10)$ = 3.28, paired t-test). Shading, ±s.e.m. (**d**) Mean firing rates during the first (light purple) and last (dark purple) wake episodes of each inter-REM interval. Each wake episode was temporally compressed to unit duration before averaging. (**e**) Mean firing rates during all NREM (gray) and wake (purple) episodes. Note that the firing rate decreased during NREM (R = -0.65, $P = 2.8\times10^{-14}$, $T(108)$ = -8.78) but increased during wake episodes (R = 0.21, P = 0.027, $T(108)$ = 2.24).

Figure 6 Homeostatic modulation of REM sleep and vlPAG GABAergic neuron activity. (**a**) Correlation between REM episode duration and subsequent inter-REM interval. Each dot represents a single episode (n = 972 episodes from 27 mice). Line, linear fit (R = 0.39, $P = 6.8 \times 10^{-36}$, $T(970)$ = 13.03). (**b**) Distribution of inter-REM interval following short (≤ 90 s) and long (> 90 s) REM episodes. The two distributions are significantly different ($P = 2.8 \times 10^{-48}$, z = -14.60, Wilcoxon rank-sum test). (**c**) Effect of closed-loop activation of vlPAG GABAergic neurons on REM sleep duration and subsequent inter-REM interval. Laser stimulation was applied as soon as spontaneous REM sleep onset was detected and lasted until the REM episode ended (only in 50% of randomly selected REM episodes the laser was turned on). Closed-loop stimulation significantly shortened both REM episodes (n = 6 mice, P = 0.002, $T(5)$ = 5.88, paired t-test) and subsequent inter-REM intervals (P = 0.003, $T(5)$ = -5.29). Each line, data from one mouse. Error bar, ±s.d. (**d**) Average normalized EEG spectrogram (upper) and mean firing rate (z-scored) of significant REM-off vlPAG GABAergic neurons (lower) during the NREM→REM→wake→NREM transition sequence. Each REM, wake, or NREM episode was temporally compressed to unit length before the firing rates were averaged over multiple sequences and across neurons. Shading, ±s.e.m. Inset, comparison of firing rates during the NREM episodes preceding ($NREM_{pre}$) and following REM sleep ($NREM_{post}$). Note that the firing rate during NR_{post} was significantly higher than that during NR_{pre} (n = 11 units; P = 0.006, $T(10)$ = -3.43, paired t-test). (**e**) Similar to (**d**), but for the NREM→wake→NREM transition sequence. Note that without the intervening REM episode, the firing rates were similar between NR_{pre} and NR_{post} (P = 0.42, $T(10)$ = 0.84). (**f**) Comparison of vlPAG activity during inter-REM interval following short (≤ 90 s) and long (> 90 s) REM episodes. Following a long REM period, the firing rate is significantly higher than following a short one (P = 0.03, $T(3)$ = -3.78, paired t-test). Shading, ±s.e.m. (**g**) Correlation between REM episode duration and vlPAG firing rate during the subsequent inter-REM interval. Each dot represents the activity of a unit during a single inter-REM interal (n = 40). Line, linear fit (R = 0.50, P = 0.001, $T(38)$ = 3.58). (**h**)

Correlation between vlPAG firing rate during inter-REM interval and duration of the interval. Each dot represents the activity of a unit during a single inter-REM interval ($n = 40$). Line, linear fit ($R = 0.63$, $P = 1.6 \times 10^{-5}$, $T(38) = 4.95$).

Figures

Figure 1.

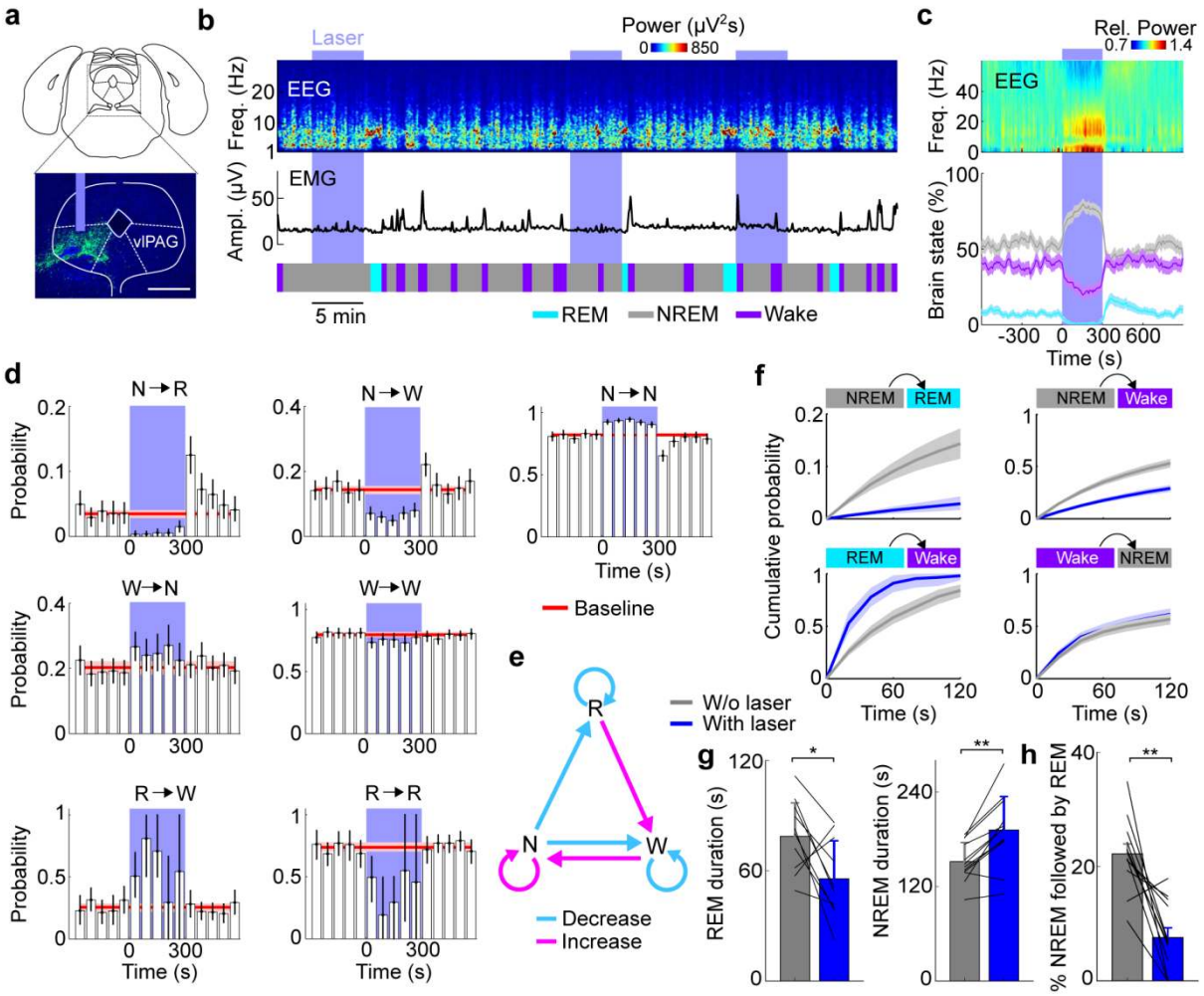

Figure 2.

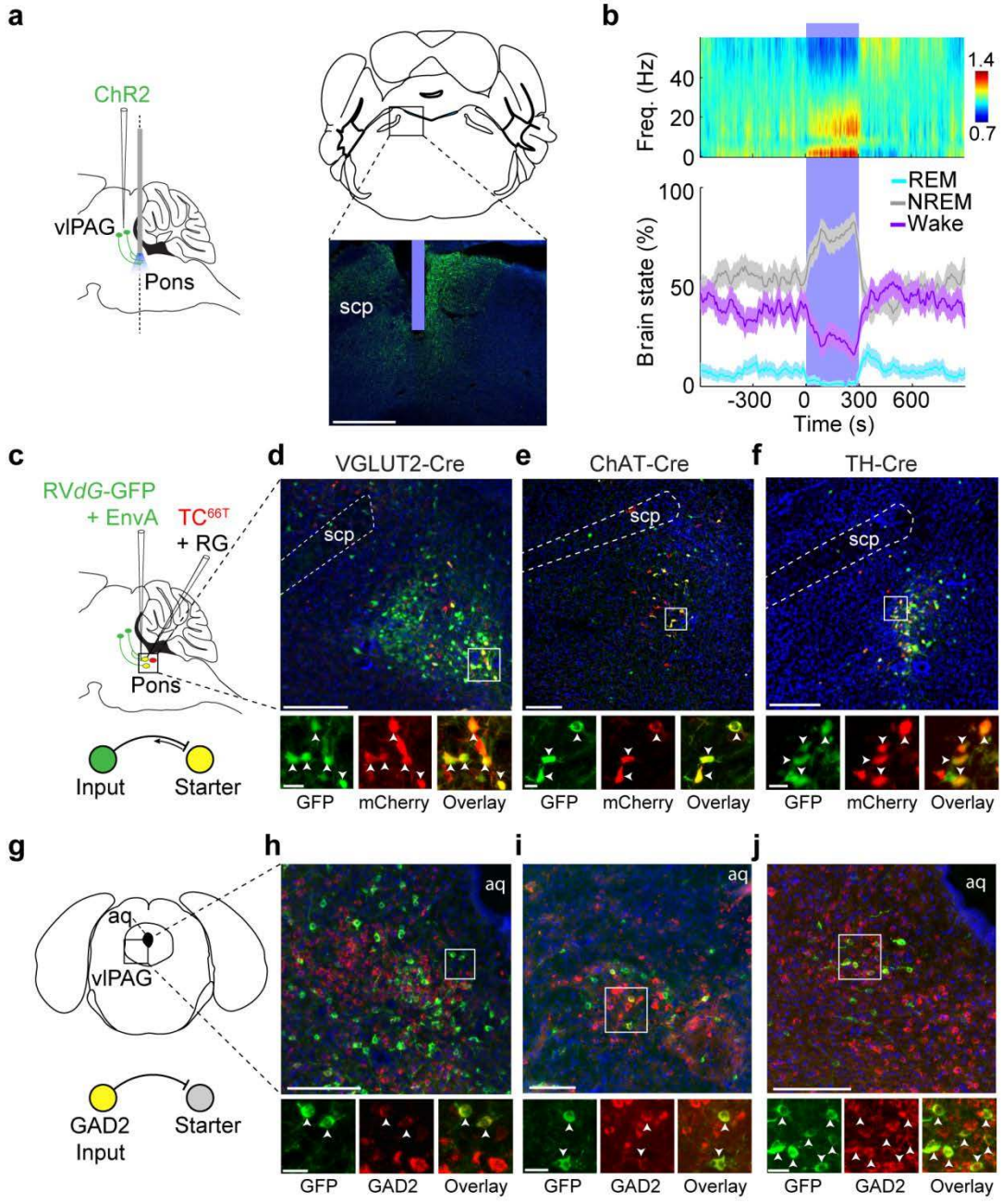
a
ChR2
vlPAG
Pons
scp
b
Freq. (Hz)
40
20
0
1.4
0.7
REM
NREM
Wake
Brain state (%)
100
50
0
-300
0
300
600
Time (s)
c
RVdG-GFP
+ EnvA
TC66T
+ RG
Pons
Input
Starter
d
VGLUT2-Cre
e
ChAT-Cre
f
TH-Cre
scp
GFP
mCherry
Overlay
g
aq
vlPAG
GAD2
Input
Starter
h
i
j
GAD2

Figure 3.

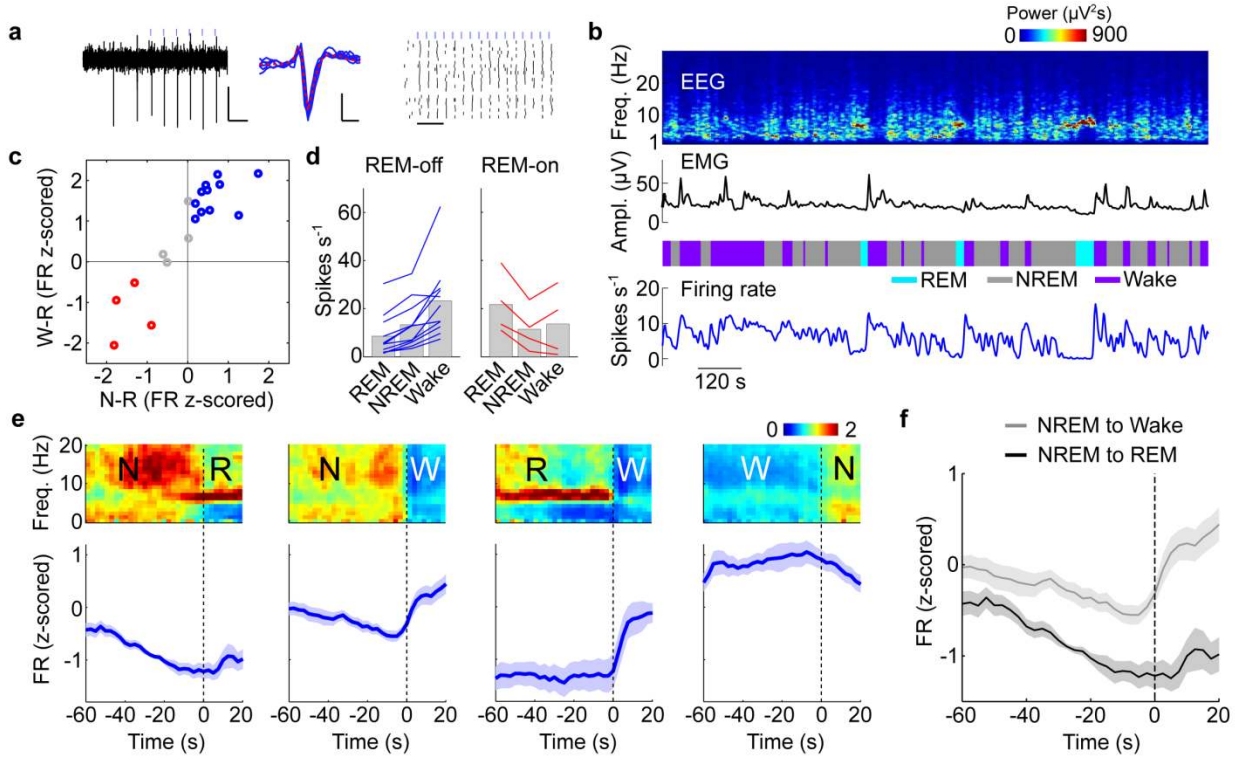
a
b
Power (μV²s)
0
900
EEG
Freq. (Hz)
20
10
1
EMG
Ampl. (μV)
50
0
REM
NREM
Wake
Firing rate
Spikes s⁻¹
120 s
c
W-R (FR z-scored)
N-R (FR z-scored)
d
REM-off
REM-on
Spikes s⁻¹
REM
NREM
Wake
e
N
R
W
0
2
Freq. (Hz)
FR (z-scored)
Time (s)
f
NREM to Wake
NREM to REM
FR (z-scored)
Time (s)

Figure 4.

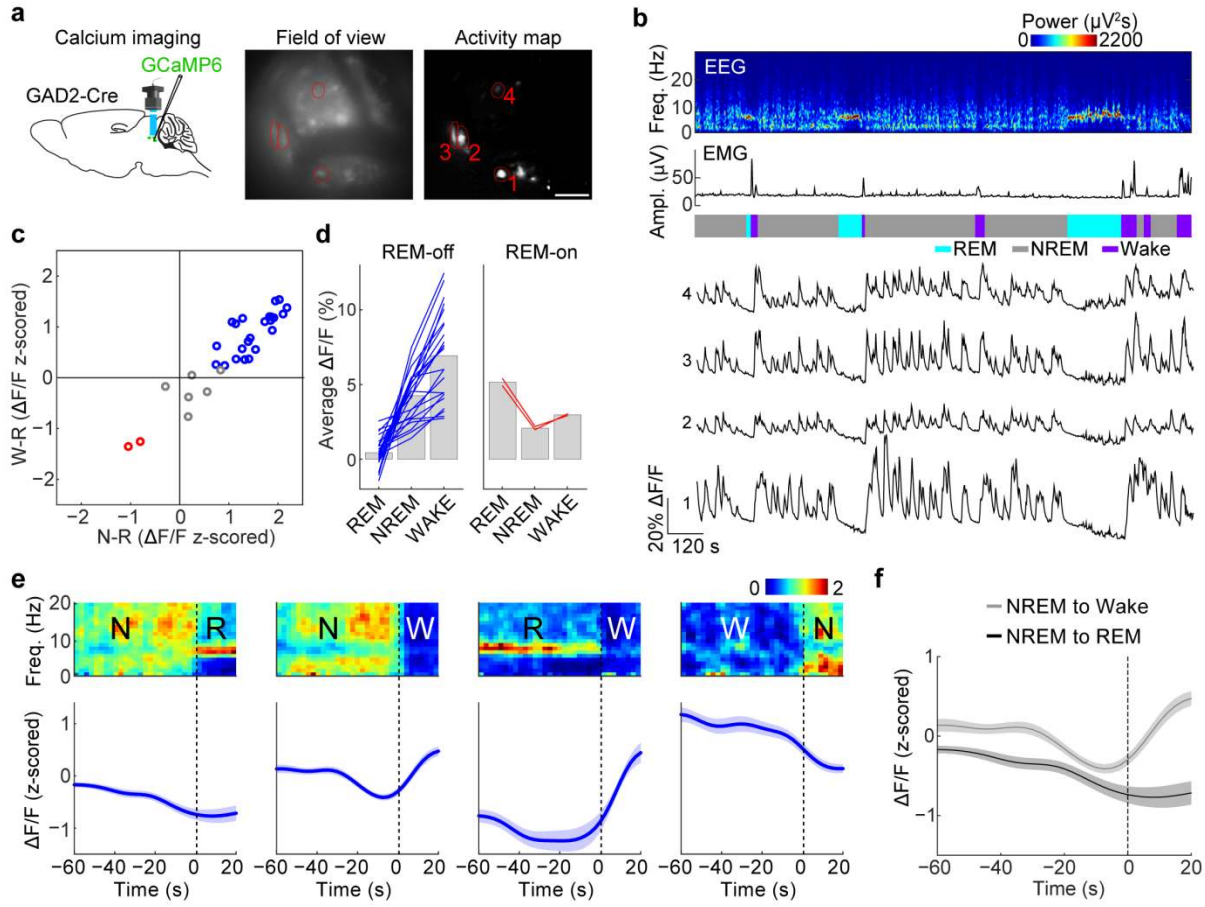

Figure 5.

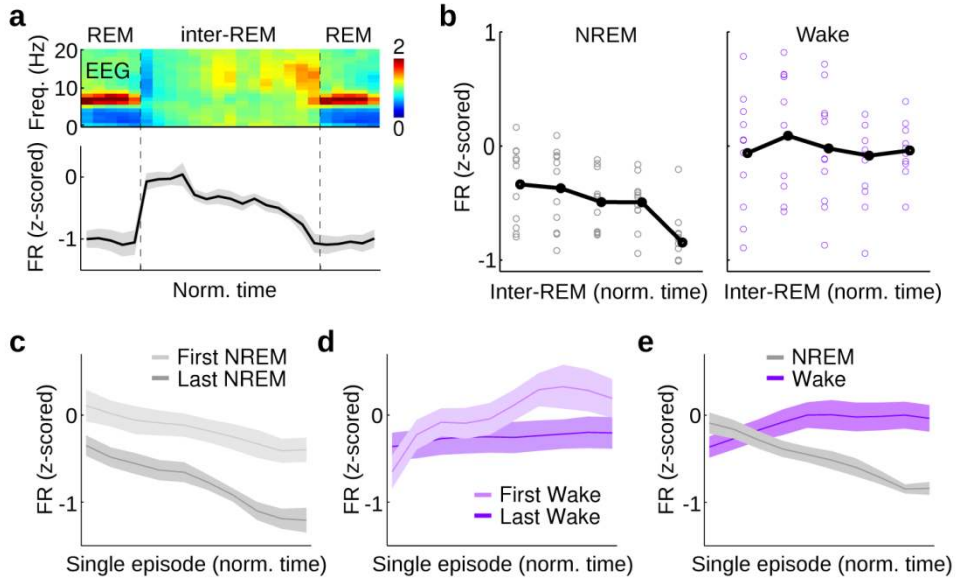

Figure 6.

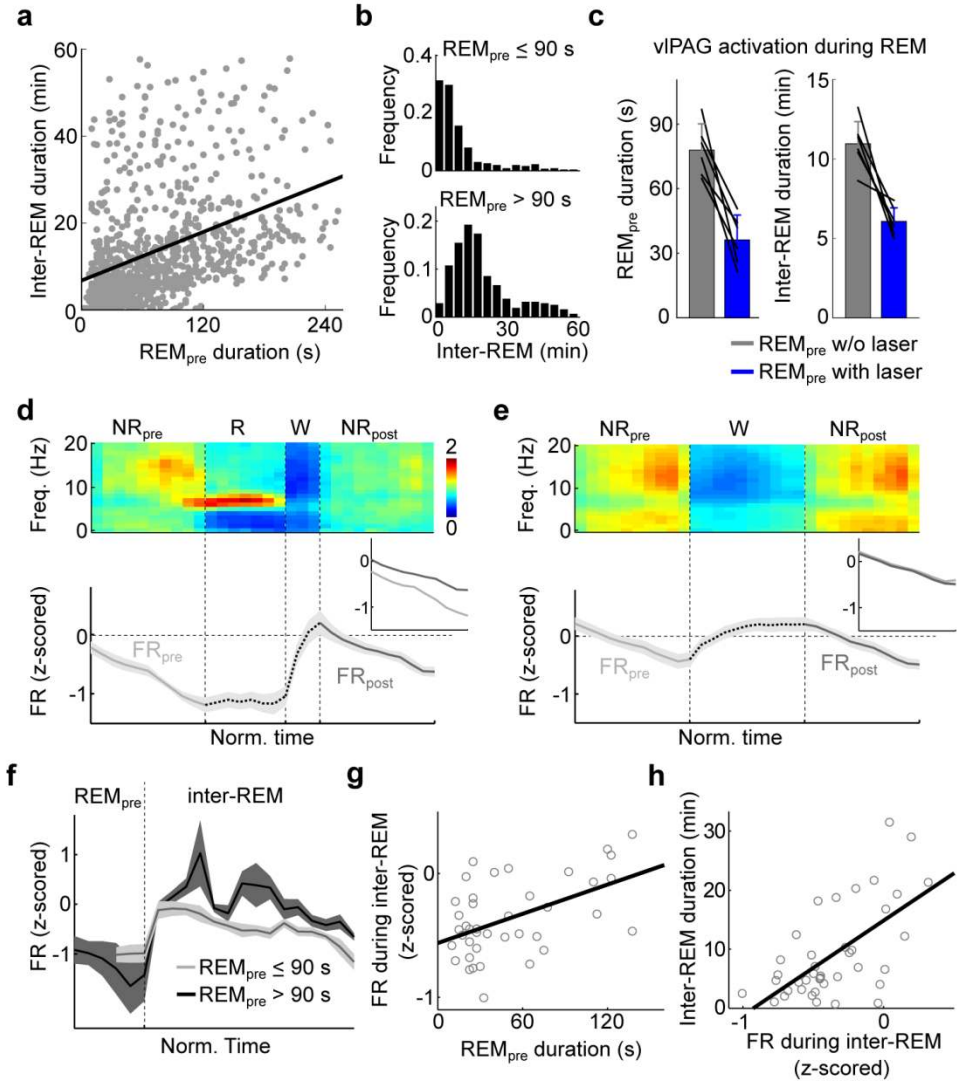
a
Inter-REM duration (min)
REMpre duration (s)
b
REMpre ≤ 90 s
REMpre > 90 s
Frequency
Inter-REM (min)
c
vlPAG activation during REM
REMpre duration (s)
Inter-REM duration (min)
REMpre w/o laser
REMpre with laser
d
NRpre
R
W
NRpost
Freq. (Hz)
FR (z-scored)
FRpre
FRpost
Norm. time
e
NRpre
W
NRpost
Freq. (Hz)
FR (z-scored)
FRpre
FRpost
Norm. time
f
REMpre
inter-REM
FR (z-scored)
REMpre ≤ 90 s
REMpre > 90 s
Norm. Time
g
FR during inter-REM (z-scored)
REMpre duration (s)
h
Inter-REM duration (min)
FR during inter-REM (z-scored)

Supplementary Figure Legends

Supplementary Figure 1. Effects of laser stimulation in vlPAG of GAD2-Cre mice expressing ChR2-eYFP or eYFP alone. (a) Effect of ChR2-mediated activation of GABAergic vlPAG neurons in additional mice (n = 6) that were not included in our previous study [1]. Top, average EEG spectrogram (normalized by the mean power in each frequency band). Bottom, percentage of REM, NREM or wake states before, during, and after laser stimulation. The changes in REM, NREM, and wake induced by laser stimulation were highly significant ($P < 0.0001$, bootstrap). Shading, 95% confidence intervals (CI). Blue stripe, laser stimulation period (20 Hz, 300 s). (b) Comparison of EEG power spectra during spontaneous NREM sleep outside of laser stimulation periods (grey) and NREM sleep overlapping with laser stimulation (blue), averaged across all ChR2-eYFP mice (n = 12). Gray shading, s.e.m. for spontaneous NREM sleep. (c) Effect of laser stimulation on brain states in eYFP control mice (n = 5). Laser stimulation did not significantly change the percentage of any brain state ($P > 0.33$, bootstrap).

Supplementary Figure 2. Optogenetic activation of glutamatergic neurons in the vlPAG induces wakefulness. (a) Top, average EEG spectrogram (normalized by the mean power in each frequency band), averaged across all VGLUT2-Cre mice (n = 4). Bottom, average EMG amplitude. Scale bar 20 µV. Shading, +/- s.e.m. (b) Bottom, percentage of REM, NREM or wake states before, during, and after laser stimulation. Optogenetic activation of the glutamatergic neurons induced a strong increase in wakefulness ($P < 0.0001$, bootstrap), while suppressing NREM sleep ($P < 0.0001$). Blue stripe, laser stimulation period (20 Hz, 120 s).

Supplementary Figure 3. Selective ablation of vlPAG GABAergic neurons increases REM sleep. (a) Top, fluorescence image from a control mouse showing the PAG. Red, FISH for mRNA encoding GAD2. Scale bar, 250 µm. Bottom, fluorescence image from an experimental animal injected with AAV expressing pro-Caspase 3 (Casp3). Note the reduced number of GAD2 neurons in the vlPAG compared to the control (top). (b) Number of GAD2 cells per section (30 µm thick) in the vlPAG of control mice (n = 5) and mice expressing Caps3 (n = 6). On average, Casp3 expression reduced the number of GAD2 cells by 54.3% ($P = 0:01$, $T(9) = -3.24$; t-test). Each circle, data from one mouse. Error bar, +/- s.d. (c) Top, 3 hr long hypnogram from a control mouse expressing eYFP recorded during the light cycle. Bottom, hypnogram recorded from a mouse expressing Casp3. (d-f) Percentage (d), average duration (e), and frequency (f) of REM, NREM, or wake states during the light cycle in control mice (n = 5, gray) and mice expressing Casp3 (n = 6, blue). In mice expressing Casp3, the percentage of REM sleep was significantly increased ($P = 0.009$, $z = 50.0$; Wilcoxon rank-sum test), due to an increased frequency of REM sleep episodes ($P = 0.02$, $z = 49.0$). In contrast, the amount of NREM sleep was significantly reduced ($P = 0.02$, $z = 23.0$). Each circle, data from one mouse. *$P < 0.05$, __$P < 0.01$, Wilcoxon rank-sum test. Error bar, +/- s.d. (g-i) Percentage, average duration, and frequency of each brain state during the dark 5 cycle in control mice (n = 4) and mice expressing Casp3 (n = 4). During the dark cycle, the percentage of REM sleep in mice expressing Casp3 was significantly increased ($P = 0.03$, $z = 26.0$), due to an increased frequency of REM sleep episodes ($P = 0.03$, $z = 26.0$).

Supplementary Figure 4. Optogenetic identification of vlPAG GABAergic neurons. (a) Distribution of the reliability of laser-evoked spikes for the 19 identified GABAergic neurons,

with 15 Hz or 200 ms step pulse stimulation (left, 6/19 neurons were tested with step pulse and 13/19 with 15 Hz stimulation) or 30 Hz stimulation (right). The reliability was defined as the fraction of laser pulses followed by a spike. (b) Right, distribution of the latency of laser-evoked spikes for identified GABAergic neurons. Latency was defined as the timing of the first spike after the onset of each laser pulse. (c) Relative firing rates of vlPAG GABAergic neurons during different wakeful behaviors. Most vlPAG GABAergic neurons showed the highest wake activity during moving or running. Only neurons from recording sessions in which the animal was engaged in all four behaviors are shown (n = 12). (d) Positions of the 19 identified vlPAG GABAergic neurons from 6 mice. Each dot indicates one neuron. Blue, REM-off neurons; red, REM-on neurons; gray other neurons.

Supplementary Figure 5. Sleep-wake activity of unidentified vlPAG neurons. (a) Firing rates of laser-unmodulated units from 6 mice. Unmodulated units include all neurons that were not significantly modulated by laser stimulation, as quantified by SALT (see Methods). W, wake; R, REM; N, NREM. Blue, significant REM-on neurons ($P < 0.05$, Wilcoxon rank-sum test, post-hoc Bonferroni correction); red, significant REM-on neurons; gray, other neurons. (b) Firing rates of laser-unmodulated REM-off (left) and REM-on (red) neurons during different brain states. Each line shows firing rates of one unit; gray bar, average across units. (c) Firing rate of laser-inhibited units. Inhibited units include neurons that were significantly modulated by laser stimulation, as quantified by SALT, and whose firing rate was significantly decreased during the 30 Hz laser stimulation period. (d) Firing rates of laser-inhibited REM-off (left) and REM-on (red) neurons during different brain states (n = 12). (e) Average EEG spectrogram (upper, normalized by the mean power in each frequency band) and mean firing rate (z-scored) of unidentified REM-on neurons (lower) at brain state transitions. The REM-on neurons include both laser-unmodulated (a,b) and laser-inhibited neurons (c,d). Shading, +/- s.e.m. (f) The firing rates of REM-on neurons during NREM episodes preceding wake or REM episodes were not significantly different (n = 12, P = 0.31, T(11) = 1.06, paired t-test).

Supplementary Figure 6. Slow modulation of vlPAG GABAergic neuron activity measured with calcium imaging. (a) Average normalized EEG spectrogram (upper) and mean calcium activity ($\Delta F/F$, z-scored) of significant REM-off ROIs (lower) during two successive REM episodes and the inter-REM interval. Each REM episode and inter- REM interval was temporally compressed to unit length before the calcium traces were averaged over multiple episodes/intervals and across ROIs (n = 23). Shading, +/- s.e.m. (b) Calcium activity ($\Delta F/F$, z-scored) during NREM (left) and wake (right) episodes within different segments of the inter-REM interval. Each inter-REM interval was divided into 5 equally sized bins, and NREM or wake activities were averaged for each bin. Each symbol represents the average NREM or wake activity of an ROI. The average NREM activity decreased during the inter-REM period (R = -0.36, $P = 7.3 \times 10^{-5}$, T(21) = -1.77, linear regression), while the wake activity showed no significant trend (R = 0.04, P = 0.76, T(23) = -0.18). Black line, average calcium activity of each bin. (c) Mean calcium activity during the first (light gray) and last (dark gray) NREM episodes of each inter-REM interval. Each NREM episode was temporally compressed to unit duration before the z-scored calcium activity was averaged over episodes and across ROIs. The activity during the first NREM period was significantly higher than during the last period (n = 23 ROIs, P = 0.00015, T(22) = 4.41, paired t-test). Shading, +/- s.e.m. (d) Mean calcium activity during the first (light purple) and last (dark purple) wake episodes of each inter-REM interval. Each wake

episode was temporally compressed to unit duration before averaging (P = 0.25, T(22) = -1.17). (e) Mean calcium activity during all NREM (gray) and wake (purple) episodes. Note that the calcium activity decreased during NREM (R = -0.36, P = 2.9 x 10^{-24}, T(21) = -1.77) but increased during wake episodes (R = 0.27, P = 1.7 x 10^{-13}, T(21) = 1.29).

Supplementary Figure 7. Firing rates of vlPAG REM-on neurons during inter-REM interval. (a) Average normalized EEG spectrogram (upper) and mean firing rate (z-scored) of significant REM-on vlPAG neurons (lower) during two successive REM episodes and the inter-REM interval. The REM-on neurons include both laser-unmodulated and laser-inhibited neurons (n = 12, red units in Supplementary Fig. 5a-d). Each REM episode and inter-REM interval was temporally compressed to unit length before the firing rates were averaged over multiple episodes/intervals and across REM-on neurons. Shading, +/- s.e.m. (b) Firing rate (FR, z-scored) during NREM (left) and wake (right) episodes within different segments of the inter-REM interval. Each inter-REM interval was divided into 5 equally sized bins, and NREM or wake firing rates were averaged for each bin. Each symbol represents the average NREM or wake firing rate of a unit. Neither the NREM nor wake activity showed a consistent change across the inter-REM period (NREM, R = 0.13, P = 0.33, T(58) = 0.10; wake, R = -0.17, P = 0.19, T(58) = -1.32; linear regression). Black line, average firing rate of each bin. (c) Mean firing rates of vlPAG REM-on neurons during the first (light gray) and last (dark gray) NREM episodes of each inter-REM interval. Each NREM episode was temporally compressed to unit duration before the z-scored firing rate was averaged over episodes and across cells. The firing rates during the last and first NREM episode were not significantly different (P = 0:19, T = T(11) = -1.39, paired t-test). Shading, +/- s.e.m. (d) Mean firing rates of REM-on units during the first (light purple) and last (dark purple) wake episodes of each inter-REM interval. Each wake episode was temporally compressed to unit duration before averaging. The firing rate during the first wake period was significantly higher than during the last one (P = 0.04, T(11) = 2.36, paired t-test). (e) Mean firing rates of REM-on units during all NREM (gray) and wake (purple) episodes. The firing rate showed no systematic change during each NREM episode (R = 0.18, P = 0.063, T(108) = 1.88, linear regression) and a slight decrease during the wake episode (R = -0.24, P = 0.01, T(108) = -2.61, linear regression).

Supplementary Figure 8. Homeostatic modulation of vlPAG GABAergic neuron activity measured with calcium imaging. (a) Average normalized EEG spectrogram (upper) and mean calcium activity (ΔF/F, z-scored) of significant REM-off ROIs (lower, n = 23) during the NREM → REM → wake → NREM transition sequence. Each REM, NREM, or wake episode was temporally compressed to unit length before the calcium activity was averaged over multiple sequences and across ROIs. Shading, +/- s.e.m. Inset, the calcium activity during the NREM episodes preceding REM (NR_{pre}) was significantly higher than during NREM episodes following REM (NR_{post}; P = 0.025, T(22) = -2.39, paired t-test). (b) Similar to (a), but for the NREM → wake → NREM transition sequence. Note that without the intervening REM episode, the calcium activities were not significantly different during NR_{pre} and NR_{post} (P = 0.085, T(22) = -1.81). (c) The calcium activity of REM-off ROIs during the inter-REM interval following a long (> 90 s) REM episode was higher than that following a short (≤ 90 s) REM episode (P = 0:028, T(22) = -2.38, paired t-test). (d) Correlation between REM episode duration and calcium activity during the subsequent inter-REM interval. Each dot represents the activity of an ROI during a single inter-REM interval (n = 189). Line, linear fit (R = 0.18, P = 0.016, T(187) = 2.50, linear

regression). (e) Correlation between calcium activity during inter-REM interval and duration of the interval. Each dot represents the activity of an ROI during a single inter-REM interval (n = 189). Line, linear fit (R = 0.35, P = 1.2 x 10^{-6}, T(187) = 5.11).

Supplementary Figure 9. Firing rates of REM-on neurons are not modulated by homeostatic REM sleep pressure. (a) Average normalized EEG spectrogram (upper) and mean firing rate (z-scored) of significant REM-on neurons (lower) during the NREM→REM→wake→NREM transition sequence. REM-on neurons include both laser-unmodulated and laser-inhibited units (n = 12). Each REM, NREM, or wake episode was temporally compressed to unit length before the firing rates were averaged over multiple sequences and across neurons. Shading, +/- s.e.m. Inset, the firing rates during the NREM periods preceding (NR_{pre}) and following REM (NR_{post}) were not significantly different (P = 0.51, T(11) = 0.68, paired t-test). (b) Similar to (a), but for the NREM→wake→NREM transition sequence. The mean firing rates of the REM-on neurons during NR_{pre} and NR_{post} were similar (P = 0.06, T(11) = -2.11, paired t-test). (c) The firing rate of REM-on neurons during the inter-REM interval following a short (≤ 90 s) REM episode were similar to that following a long (> 90 s) REM episode (P = 0.18, T(6) = -1.51, paired t-test). (d) The firing rates of REM-on neurons during the subsequent inter-REM interval showed no significant correlation with REM episode duration. Each dot represents the activity of a unit during a single inter-REM interval (n = 56). Line, linear fit (R = 0.07, P = 0.60, T(54) = 0.52, linear regression). (e) The duration of an inter-REM interval was not significantly correlated with the firing rate of REM-on neurons during the interval. Each dot represents the activity of a unit during a single inter-REM interval (n = 56). Line, linear fit (R = 0.05, P = 0.70, T(54) = 0.39).

Supplemental Figures

Supplementary Figure 1.

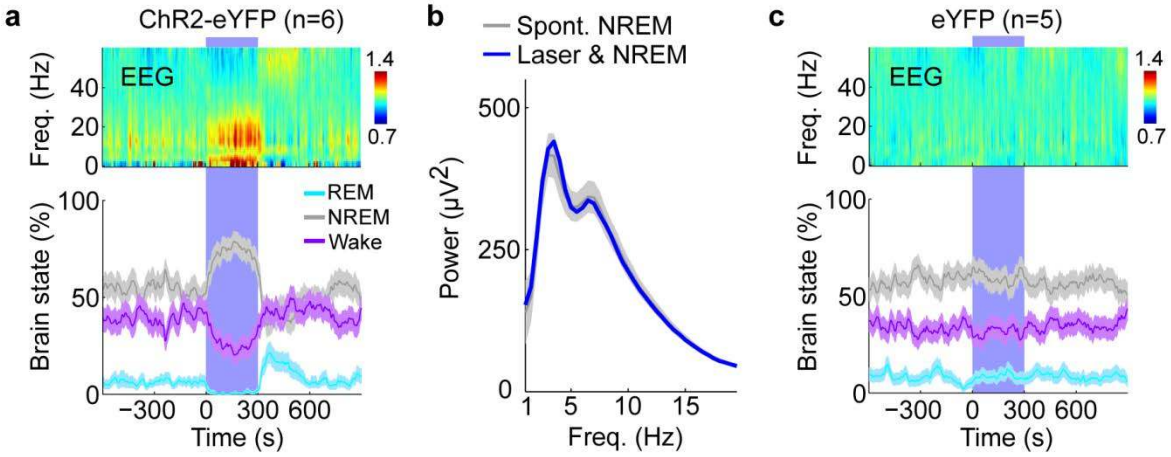

Supplementary Figure 2.

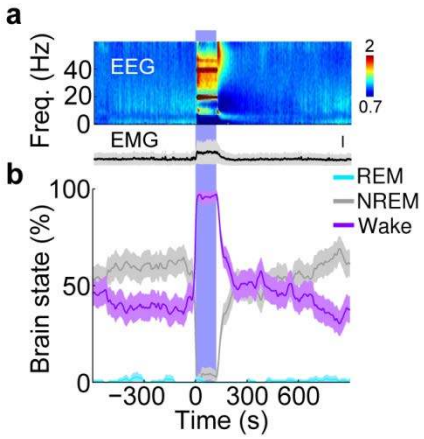

Supplementary Figure 3.

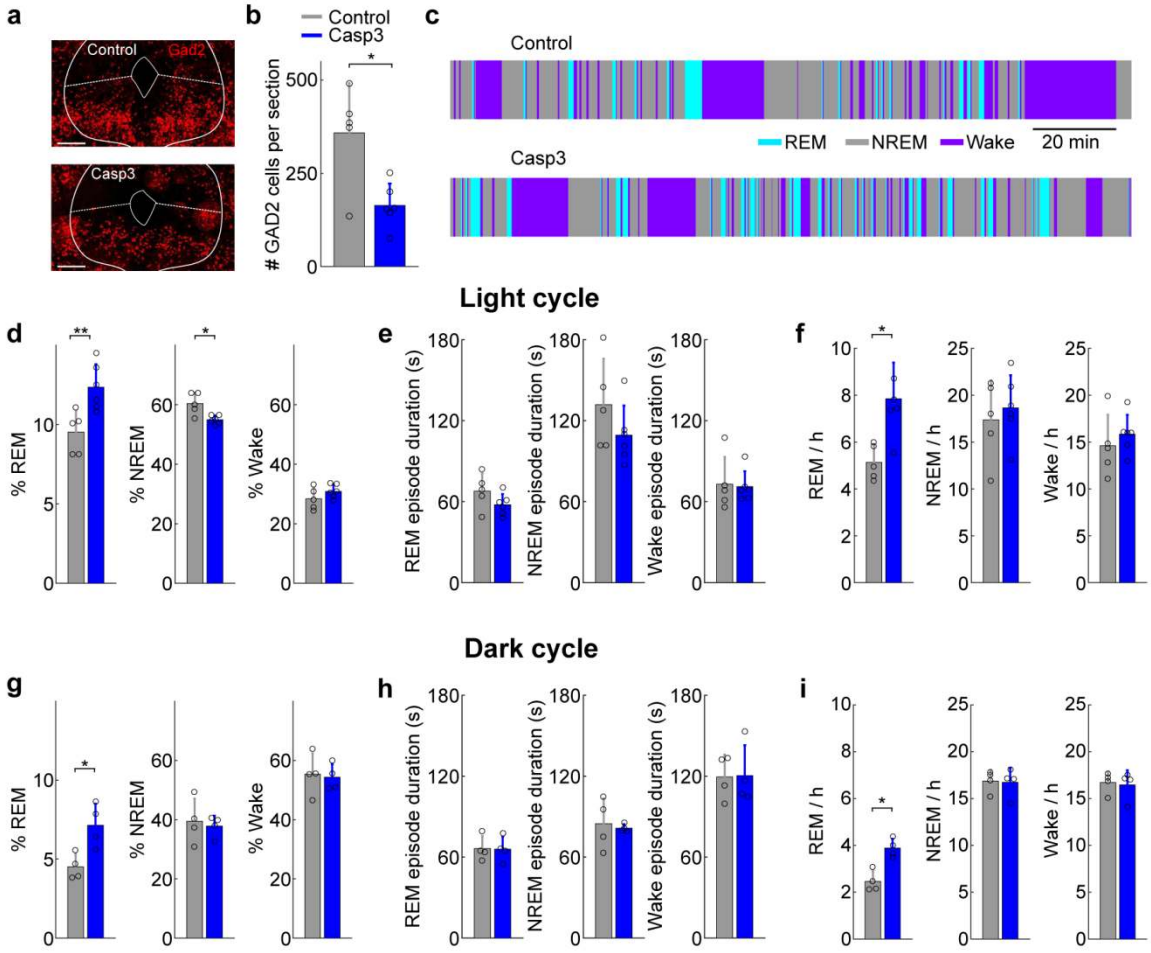

Supplementary Figure 4.

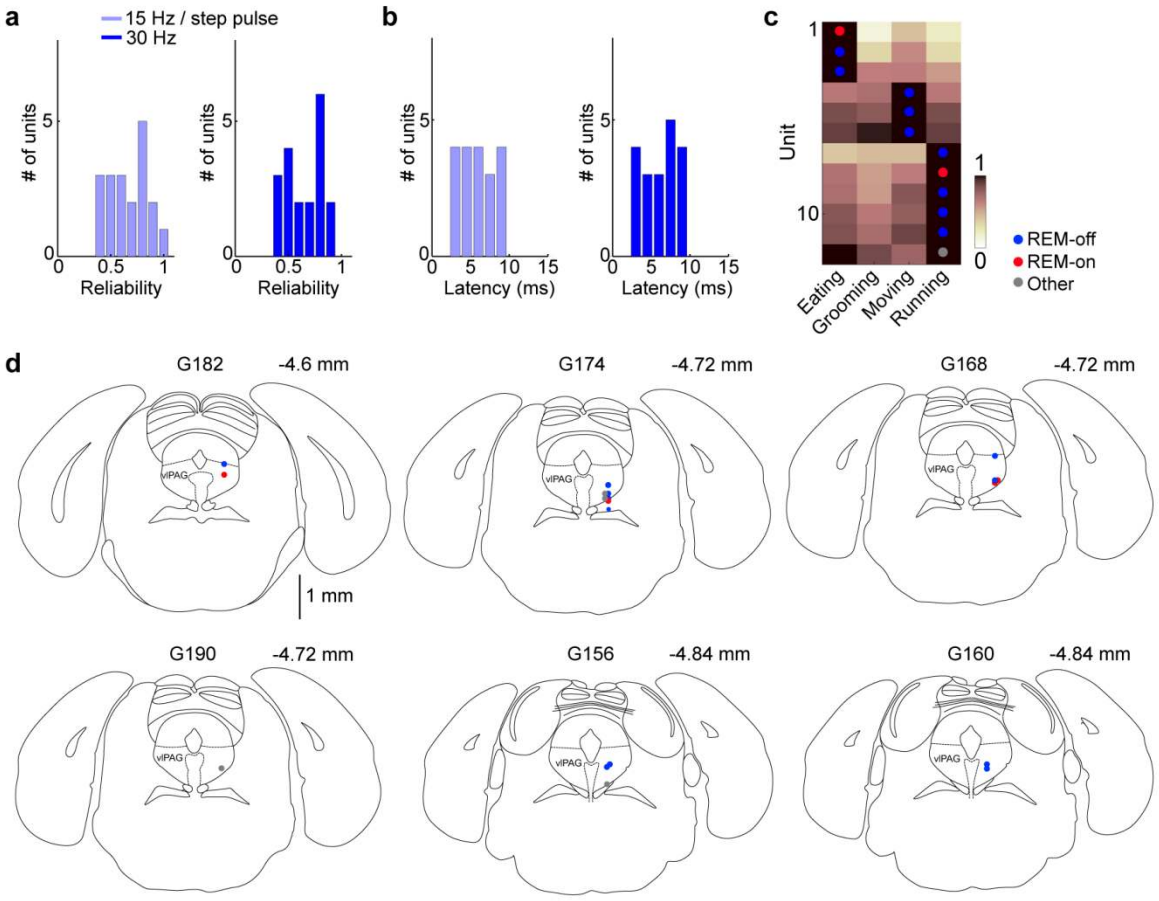

Supplementary Figure 5.

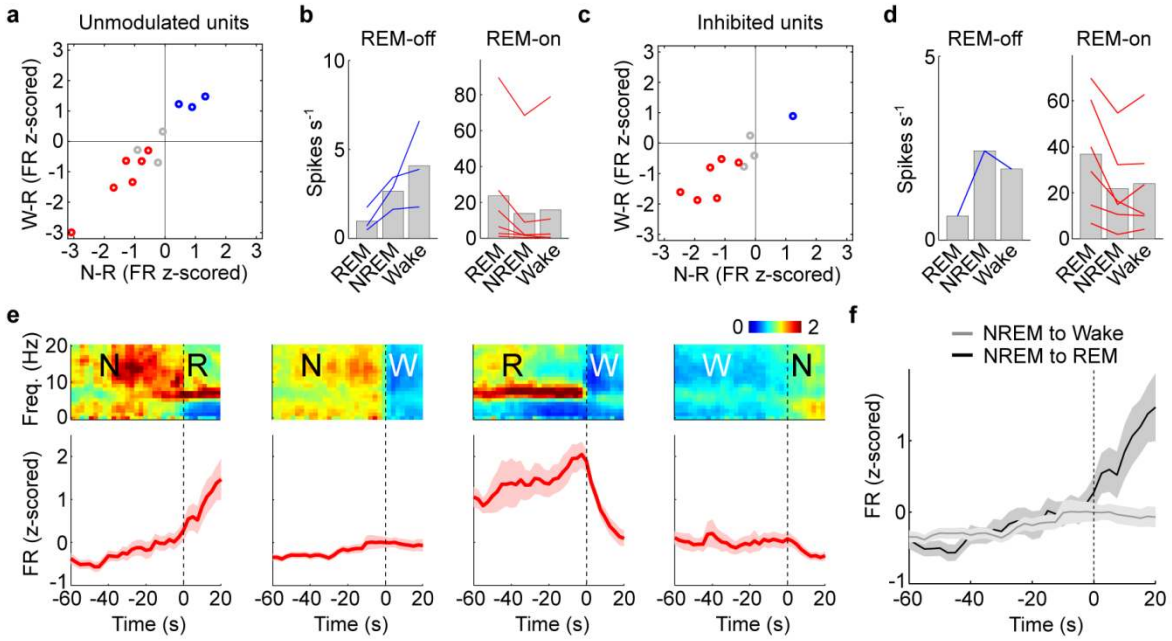

Supplementary Figure 6

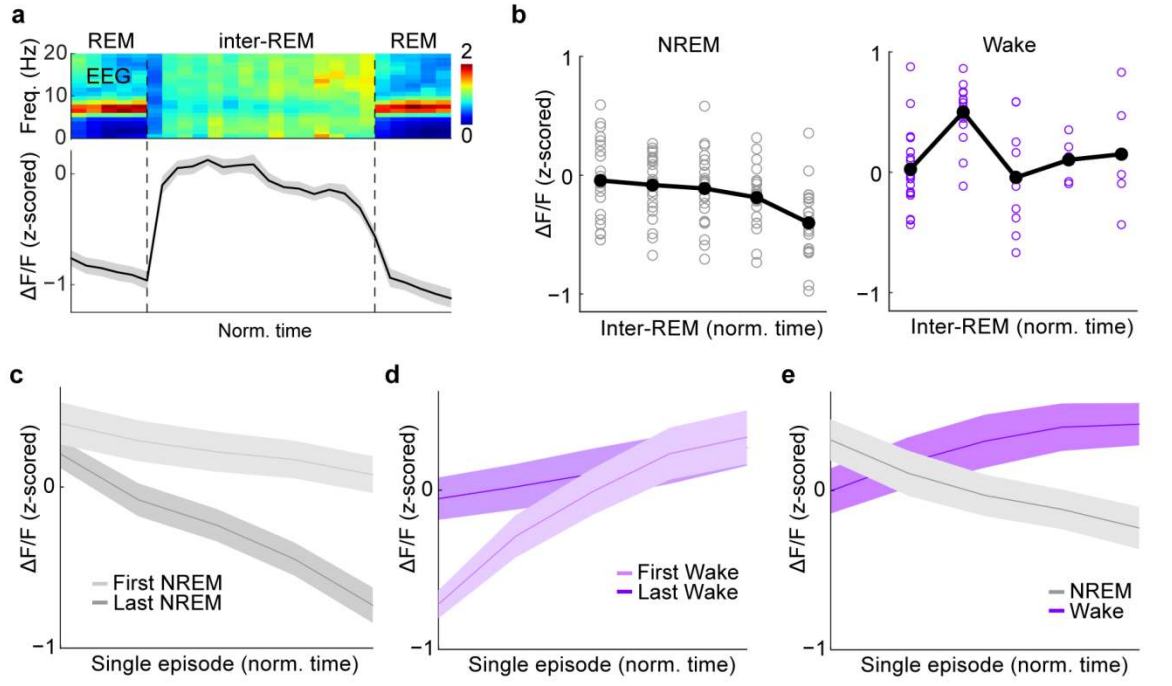

Supplementary Figure 7

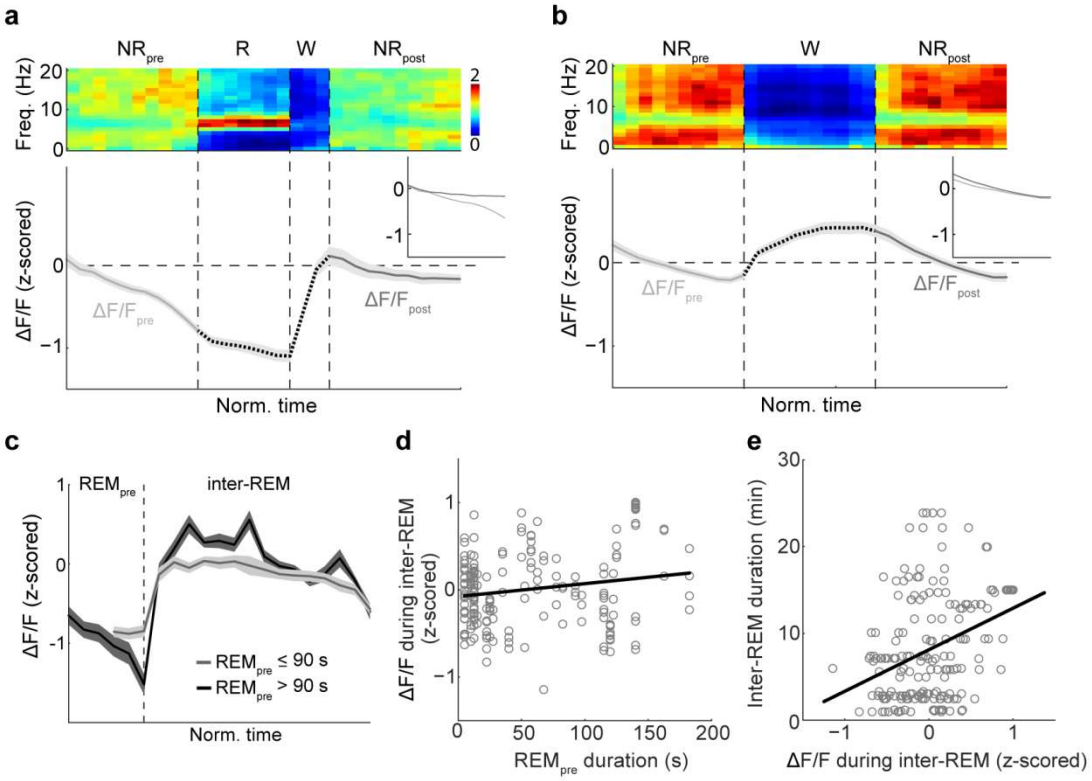

Supplementary Figure 8.

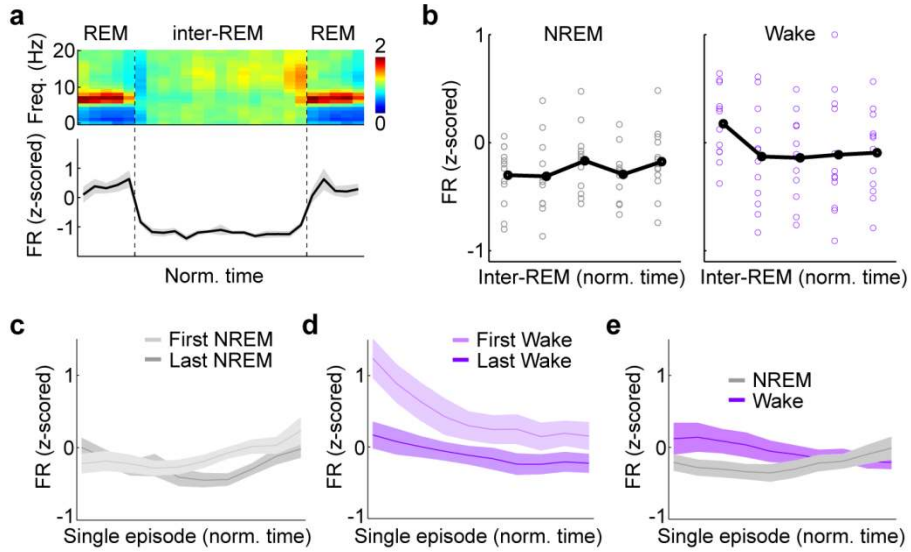

Supplementary Figure 9.

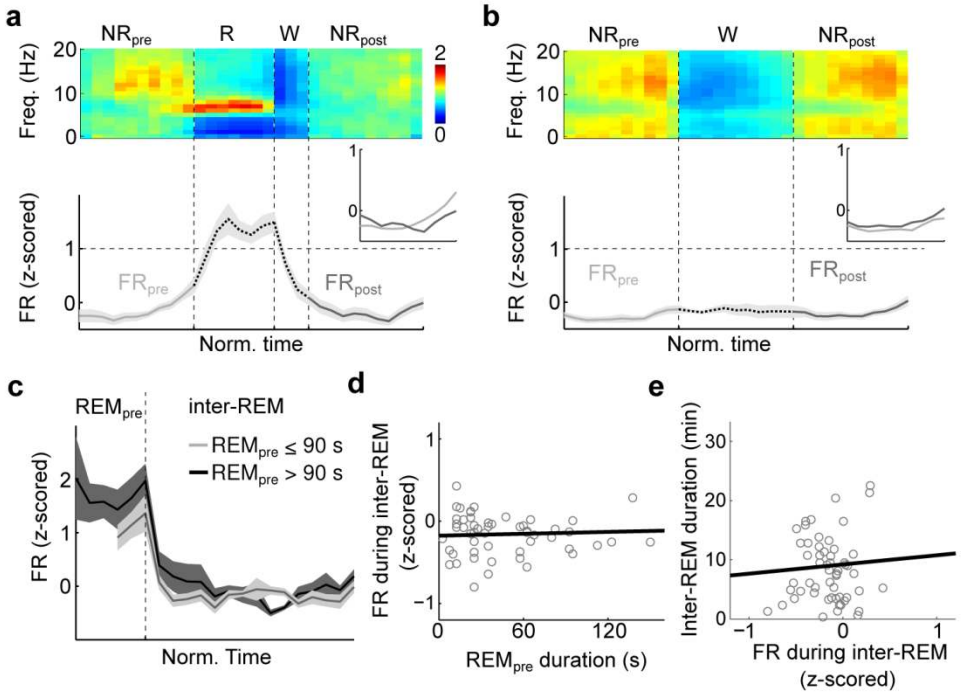

References

1. Shein-Idelson, M., Ondracek, J. M., Liaw, H., Reiter, S. & Laurent, G. Slow waves, sharp waves, ripples, and REM in sleeping dragons. *Science* **352,** 590–595 (2016).
2. Cirelli, C. & Bushey, D. Sleep and wakefulness in Drosophila melanogaster. *Ann. N. Y. Acad. Sci.* **1129,** 323–329 (2008).
3. Lu, J., Greco, M. a, Shiromani, P. & Saper, C. B. Effect of lesions of the ventrolateral preoptic nucleus on NREM and REM sleep. *J. Neurosci.* **20,** 3830–42 (2000).
4. Lorenzo, I., Ramos, J., Arce, C. & Guevara, M. A. Effect of total sleep deprivation on reaction time and waking EEG activity in man. *Sleep J. Sleep Res. Sleep Med.* **18,** 346–354 (1995).
5. Maddox, W. T. *et al.* The effects of sleep deprivation on information-integration categorization performance. *Sleep* **32,** 1439–1448 (2009).
6. Havekes, R. & Abel, T. The tired hippocampus: the molecular impact of sleep deprivation on hippocampal function. *Curr. Opin. Neurobiol.* **44,** 13–19 (2017).
7. Scott, J. P. R., McNaughton, L. R. & Polman, R. C. J. Effects of sleep deprivation and exercise on cognitive, motor performance and mood. *Physiol. Behav.* **87,** 396–408 (2006).
8. Leproult, R. & Copinschi, G. Sleep Loss Results in an Elevation of Cortisol Levels the Next Evening. *Sleep* (1997). doi:10.1093/sleep/20.10.865
9. Horne, J. & Reyner, L. Vehicle accidents related to sleep: a review. *Occup Env. Med* **56,** 289–294 (1999).
10. R. Wolk, A.S. Gami, A. Garcia-Touchard, V. K. S. Sleep and Cardiovascular Disease. *Psychiatry Hear. Dis. Mind, Brain, Hear.* 135–152 (2012). doi:10.1002/9780470975138.ch11
11. Mullington, M. J., Haack, M., Toth, M., Serrador, M., Meier-Ewert, H. Cardiovascular,Inflammatory and Metabolic Consequences of Sleep Deprivation. *Prog Cardiovasc Dis.* **51,** 294–302 (2009).
12. Breslau, N., Roth, T., Rosenthal, L. & Andreski, P. Sleep disturbance and psychiatric disorders: A longitudinal epidemiological study of young adults. *Biol. Psychiatry* **39,** 411–418 (1996).
13. Everson, C. A., Bergmann, B. M. & Rechtschaffen, A. Sleep deprivation in the rat: III. Total sleep deprivation. *Sleep* **12,** 13–21 (1989).
14. Xie, L. *et al.* Sleep Drives Metabolite Clearance from the Adult Brain. *Science* **342,** 373–377 (2013).
15. O'Callaghan, E. K., Ballester Roig, M. N. & Mongrain, V. Cell Adhesion Molecules and Sleep. *Neurosci. Res.* **116,** 29–38 (2016).
16. de Vivo, L. *et al.* Ultrastructural evidence for synaptic scaling across the wake/sleep cycle. *Science* **355,** 507–510 (2017).
17. Besedovsky, L., Lange, T. & Born, J. Sleep and immune function. *Pflugers Arch. Eur. J. Physiol.* **463,** 121–137 (2012).
18. Irwin, M. R. & Opp, M. R. Sleep-Health: Reciprocal Regulation of Sleep and Innate Immunity. *Neuropsychopharmacology* **42,** 1–96 (2016).
19. Buzsáki, G., Anastassiou, C. A. & Koch, C. The origin of extracellular fields and currents — EEG, ECoG, LFP and spikes. *Nat. Rev. Neurosci.* **13,** 407–420 (2012).
20. Brown, R. E., Basheer, R., McKenna, J. T., Strecker, R. E. & McCarley, R. W. Control of sleep and wakefulness. *Physiol. Rev.* **92,** 1087–187 (2012).

21. von Economo, C. Sleep as a Problem of Localization. *J. Nerv. Ment. Dis.* **71,** 1–5 (1930).
22. Nauta, W. J. H. Hypothalamic Regulation of Sleep in Rats. An Experimental Study. *Sleep (Rochester)* 285–316 (1946).
23. In Vitro Identification of the Presumed Sleep-Promoting Neurons of the Ventrolateral Preoptic Nucleus (VLPO). *Sleep Circuits Funct.* (2005).
24. Saper, C. B., Scammell, T. E. & Lu, J. Hypothalamic regulation of sleep and circadian rhythms. *Nature* **437,** 1257–63 (2005).
25. Nitz, D. & Siegel, J. GABA release in the dorsal raphe nucleus: role in the control of REM sleep. *Am. J. Physiol.* **273,** R451-5 (1997).
26. Nitz, D. & Siegel, J. M. GABA release in the locus coeruleus as a function of sleep/wake state. *Neuroscience* **78,** 795–801 (1997).
27. Chou, T. C. *et al.* Afferents to the ventrolateral preoptic nucleus. *J. Neurosci.* **22,** 977–90 (2002).
28. Saper, C. B., Fuller, P. M., Pedersen, N. P., Lu, J. & Scammell, T. E. Sleep state switching. *Neuron* **68,** 1023–42 (2010).
29. Anaclet, C. *et al.* Identification and characterization of a sleep-active cell group in the rostral medullary brainstem. *J. Neurosci.* **32,** 17970–6 (2012).
30. Anaclet, C. *et al.* The GABAergic parafacial zone is a medullary slow wave sleep–promoting center. *Nat. Neurosci.* **17,** 1–10 (2014).
31. Weber, F. *et al.* Control of REM sleep by ventral medulla GABAergic neurons. *Nature* **526,** 435–8 (2015).
32. Hayashi, Y. *et al.* Cells of a common developmental origin regulate REM/non-REM sleep and wakefulness in mice. **350,** (2015).
33. Boissard, R. *et al.* The rat ponto-medullary network responsible for paradoxical sleep onset and maintenance: A combined microinjection and functional neuroanatomical study. *Eur. J. Neurosci.* **16,** 1959–1973 (2002).
34. Lu, J., Sherman, D., Devor, M. & Saper, C. B. A putative flip-flop switch for control of REM sleep. *Nature* **441,** 589–94 (2006).
35. Krenzer, M. *et al.* Brainstem and spinal cord circuitry regulating rem sleep and muscle atonia. *PLoS One* **6,** 1–10 (2011).
36. Cox, J., Pinto, L. & Dan, Y. Calcium imaging of sleep–wake related neuronal activity in the dorsal pons. *Nat. Commun.* **7,** 10763 (2016).
37. Jouvet, M. Recherches sur les structures nerveuses et les mechnismes responsables des differentes phases du sommeil physiologique. *Arch. Ital. Biol* 125–206 (1962).
38. Sapin, E. *et al.* Localization of the brainstem GABAergic neurons controlling Paradoxical (REM) sleep. *PLoS One* **4,** (2009).
39. Torterolo, P. *et al.* Melanin-concentrating hormone (MCH): Role in REM sleep and depression. *Front. Neurosci.* **9,** 1–13 (2015).
40. Jego, S. *et al.* Optogenetic identification of a rapid eye movement sleep modulatory circuit in the hypothalamus. *Nat. Neurosci.* **16,** 1637–43 (2013).
41. Van Dort, C. J. *et al.* Optogenetic activation of cholinergic neurons in the PPT or LDT induces REM sleep. *Proc. Natl. Acad. Sci.* **112,** 584–589 (2015).
42. Bremer, F. Cerveau isolé et physiologie du sommeil. *CR Soc. Biol.(Paris)* **118,** 1235–1241 (1935).
43. Moruzzi, G. & Magoun, H. W. Brain stem reticular formation and activation of the EEG. *Electroencephalogr Clin Neurophysiol* **1,** 455–473 (1949).

44. Carter, M. E. *et al.* Tuning arousal with optogenetic modulation of locus coeruleus neurons. *Nat. Neurosci.* **13,** 1526–33 (2010).
45. Venner, A., Anaclet, C., Broadhurst, R. Y., Saper, C. B. & Fuller, P. M. A Novel Population of Wake-Promoting GABAergic Neurons in the Ventral Lateral Hypothalamus. *Curr. Biol.* **26,** 2137–2143 (2016).
46. Welsh, D. K., Takahashi, J. S. & Kay, S. A. Suprachiasmatic nucleus: cell autonomy and network properties. *Annu. Rev. Physiol.* **72,** 551–77 (2010).
47. Daan, S., Beersma, D. G. & Borbély, A. A. Timing of human sleep: recovery process gated by a circadian pacemaker. *Am. J. Physiol.* **246,** R161–R183 (1984).
48. Eastman, C. I., Mistlberger, R. E. & Rechtschaffen, A. Suprachiasmatic nuclei lesions eliminate circadian temperature and sleep rhythms in the rat. *Physiol. Behav.* **32,** 357–368 (1984).
49. Chou, T. C. *et al.* Critical Role of Dorsomedial Hypothalamic Nucleus in a Wide Range of Behavioral Circadian Rhythms. *J. Neurosci.* **23,** 10691–10702 (2003).
50. Wurts, S. W. & Edgar, D. M. Circadian and Homeostatic Control of Rapid Eye Movement (REM) Sleep: Promotion of REM Tendency by the Suprachiasmatic Nucleus. *J. Neurosci.* **20,** 4300–4310 (2000).
51. Ishimori, K. True cause of sleep: a hypnogenic substance as evidenced in the brain of sleep-deprived animals. *Tokyo Igakkai Zasshi* **23,** 429–457 (1909).
52. Legendre, R. & Pieron, H. Recherches sur le besoin de sommeil consécutif à une veille prolongée. *Z allg Physiol* **14,** 235–262 (1913).
53. Chen, J.-F., Eltzschig, H. K. & Fredholm, B. B. Adenosine receptors as drug targets — what are the challenges? *Nat. Rev. Drug Discov.* **12,** 265–286 (2013).
54. Porkka-Heiskanen, T. *et al.* Adenosine: A Mediator of the Sleep-Inducing Effects of Prolonged Wakefulness. *Science* **276,** 1265–1268 (1997).
55. Porkka-Heiskanen, T., Strecker, R. E. & McCarley, R. W. Brain site-specificity of extracellular adenosine concentration changes during sleep deprivation and spontaneous sleep: An in vivo microdialysis study. *Neuroscience* **99,** 507–517 (2000).
56. Portas, C. M., Thakkar, M., Rainnie, D. G., Greene, R. W. & McCarley, R. W. Role of adenosine in behavioral state modulation: A microdialysis study in the freely moving cat. *Neuroscience* **79,** 225–235 (1997).
57. Oishi, Y., Huang, Z.-L., Fredholm, B. B., Urade, Y. & Hayaishi, O. Adenosine in the tuberomammillary nucleus inhibits the histaminergic system via A1 receptors and promotes non-rapid eye movement sleep. *Proc. Natl. Acad. Sci. U. S. A.* **105,** 19992–7 (2008).
58. Ding, F. *et al.* Changes in the composition of brain interstitial ions control the sleep-wake cycle. *Science* **352,** 550–5 (2016).
59. Bakin, J. S. & Weinberger, N. M. Induction of a physiological memory in the cerebral cortex by stimulation of the nucleus basalis. *Proc Natl Acad Sci U S A* **93,** 11219–11224 (1996).
60. Everitt, B. J. & Robbins, T. W. Central cholinergic systems and cognition. *Annu Rev Psychol* **48,** 649–684 (1997).
61. Froemke, R. C. *et al.* Long-term modification of cortical synapses improves sensory perception. *Nat Neurosci* **16,** 79–88 (2013).
62. Sarter, M., Hasselmo, M. E., Bruno, J. P. & Givens, B. Unraveling the attentional functions of cortical cholinergic inputs: interactions between signal-driven and cognitive

modulation of signal detection. *Brain Res Brain Res Rev* **48,** 98–111 (2005).
63. Jones, B. E. Neurobiology of waking and sleeping. *Handb Clin Neurol* **98,** 131–149 (2011).
64. Parikh, V. & Sarter, M. Cholinergic mediation of attention: Contributions of phasic and tonic increases in prefrontal cholinergic activity. *Ann. N. Y. Acad. Sci.* **1129,** 225–235 (2008).
65. Xu, M. *et al.* Basal forebrain circuit for sleep-wake control. *Nat. Neurosci.* **18,** 1641–1647 (2015).
66. Depaulis, A., Keay, K. A. & Bandler, R. Longitudinal neuronal organization of defensive reactions in the midbrain periaqueductal gray region of the rat. *Exp. Brain Res.* **90,** 307–318 (1992).
67. De Oca, B. M., DeCola, J. P., Maren, S. & Fanselow, M. S. Distinct regions of the periaqueductal gray are involved in the acquisition and expression of defensive responses. *J. Neurosci.* **18,** 3426–3432 (1998).
68. Bandler, R. & Shipley, M. T. Columnar organization in the midbrain periaqueductal gray: modules for emotional expression? *Trends Neurosci.* **17,** 379–389 (1994).
69. Bandler, R. & Depaulis, A. Midbrain periaqueductal grey control of defensive behaviour in the cat and the rat. *Plenum Press* 175–198 (1991).
70. Weber, F. & Dan, Y. Circuit-based interrogation of sleep control. *Nature* **538,** 51–59 (2016).
71. Boissard, R., Fort, P., Gervasoni, D., Barbagli, B. & Luppi, P. H. Localization of the GABAergic and non-GABAergic neurons projecting to the sublaterodorsal nucleus and potentially gating paradoxical sleep onset. *Eur. J. Neurosci.* **18,** 1627–1639 (2003).
72. Brown, R. E., Basheer, R., McKenna, J. T., Strecker, R. E. & McCarley, R. W. Control of Sleep and Wakefulness. *Physiol. Rev.* **92,** 1087–1187 (2012).
73. Hasselmo, M. E. & Sarter, M. Modes and models of forebrain cholinergic neuromodulation of cognition. *Neuropsychopharmacology* **36,** 52–73 (2011).
74. Lin, S., Brown, R. E., Hussain Shuler, M. G., Petersen, C. C. H. & Kepecs, A. Optogenetic Dissection of the Basal Forebrain Neuromodulatory Control of Cortical Activation, Plasticity, and Cognition. *J. Neurosci.* **35,** 13896–903 (2015).
75. Schliebs, R. & Arendt, T. The cholinergic system in aging and neuronal degeneration. *Behav. Brain Res.* **221,** 555–563 (2011).
76. Whitehouse, P. J. *et al.* Alzheimer's Disease and Senile Dementia: Loss of Neurons in the Basal Forebrain. *Science* **215,** 9–12 (1982).
77. Zaborszky, L. & Duque, A. Local synaptic connections of basal forebrain neurons. *Behav. Brain Res.* **115,** 143–58 (2000).
78. Yang, C. *et al.* Cholinergic Neurons Excite Cortically Projecting Basal Forebrain GABAergic Neurons. *J. Neurosci.* **34,** 2832–2844 (2014).
79. Asanuma, C. Axonal arborizations of a magnocellular basal nucleus input and their relation to the neurons in the thalamic reticular nucleus of rats. *Proc Natl Acad Sci U S A* **86,** 4746–4750 (1989).
80. Freund, T. F. & Meskenaite, V. gamma-Aminobutyric acid-containing basal forebrain neurons innervate inhibitory interneurons in the neocortex. *Proc Natl Acad Sci U S A* **89,** 738–742 (1992).
81. Grove, E. A. Efferent connections of the substantia innominata in the rat. *J. Comp. Neurol.* **277,** 347–364 (1988).

82. Henny, P. & Jones, B. E. Vesicular glutamate (VGlut), GABA (VGAT), and acetylcholine (VACht) transporters in basal forebrain axon terminals innervating the lateral hypothalamus. *J Comp Neurol* **496,** 453–467 (2006).
83. Manns, I. D., Mainville, L. & Jones, B. E. Evidence for glutamate, in addition to acetylcholine and GABA, neurotransmitter synthesis in basal forebrain neurons projecting to the entorhinal cortex. *Neuroscience* **107,** 249–263 (2001).
84. Parent, A., Pare, D., Smith, Y. & Steriade, M. Basal forebrain cholinergic and noncholinergic projections to the thalamus and brainstem in cats and monkeys. *J Comp Neurol* **277,** 281–301 (1988).
85. Rye, D. B., Wainer, B. H., Mesulam, M. M., Mufson, E. J. & Saper, C. B. Cortical projections arising from the basal forebrain: a study of cholinergic and noncholinergic components employing combined retrograde tracing and immunohistochemical localization of choline acetyltransferase. *Neuroscience* **13,** 627–643 (1984).
86. Semba, K., Reiner, P. B., McGeer, E. G. & Fibiger, H. C. Brainstem afferents to the magnocellular basal forebrain studied by axonal transport, immunohistochemistry, and electrophysiology in the rat. *J Comp Neurol* **267,** 433–453 (1988).
87. Záborszky, L. & Cullinan, W. E. Projections from the nucleus accumbens to cholinergic neurons of the ventral pallidum: a correlated light and electron microscopic double-immunolabeling study in rat. *Brain Res.* **570,** 92–101 (1992).
88. Cullinan, W. E. & Záborszky, L. Organization of ascending hypothalamic projections to the rostral forebrain with special reference to the innervation of cholinergic projection neurons. *J. Comp. Neurol.* **306,** 631–67 (1991).
89. Grove, E. A. Neural associations of the substantia innominata in the rat: Afferent connections. *J. Comp. Neurol.* **277,** 315–346 (1988).
90. Jones, B. E. & Cuello, A. C. Afferents to the basal forebrain cholinergic cell area from pontomesencephalic--catecholamine, serotonin, and acetylcholine--neurons. *Neuroscience* **31,** 37–61 (1989).
91. Pare, D. & Smith, Y. GABAergic projection from the intercalated cell masses of the amygdala to the basal forebrain in cats. *J Comp Neurol* **344,** 33–49 (1994).
92. Mesulam, M. M. & Mufson, E. J. Neural inputs into the nucleus basalis of the substantia innominata (ch4) in the rhesus monkey. *Brain* **107,** 253–274 (1984).
93. Steriade, M. & McCarley, R. W. *Brain control of wakefulness and sleep*. (Springer, 2005).
94. Zaborszky, L., van den Pol, A. & Gyengesi, E. in *The mouse nervous system* (eds. WATSON, C., Paxinos, G. & PUELLES, L.) 684–718 (Elsevier Inc., 2012).
95. Semba, K. Multiple output pathways of the basal forebrain: organization, chemical heterogeneity, and roles in vigilance. *Behav. Brain Res.* **115,** 117–41 (2000).
96. Wenk, G. L. The nucleus basalis magnocellularis cholinergic system: one hundred years of progress. *Neurobiol. Learn. Mem.* **67,** 85–95 (1997).
97. McGaughy, J., Kaiser, T. & Sarter, M. Behavioral vigilance following infusions of 192 IgG-saporin into the basal forebrain: selectivity of the behavioral impairment and relation to cortical AChE-positive fiber density. *Behav. Neurosci.* **110,** 247–265 (1996).
98. Conner, J. M., Culberson, A., Packowski, C., Chiba, A. A. & Tuszynski, M. H. Lesions of the basal forebrain cholinergic system impair task acquisition and abolish cortical plasticity associated with motor skill learning. *Neuron* **38,** 819–829 (2003).
99. Hangya, B., Ranade, S. P., Lorenc, M. & Kepecs, A. Central Cholinergic Neurons Are Rapidly Recruited by Reinforcement Feedback. *Cell* **162,** 1155–1168 (2015).

100. Avila, I. & Lin, S. Distinct neuronal populations in the basal forebrain encode motivational salience and movement. *Front. Behav. Neurosci.* **8,** 421 (2014).
101. Lin, S. C. & Nicolelis, M. A. L. Neuronal Ensemble Bursting in the Basal Forebrain Encodes Salience Irrespective of Valence. *Neuron* **59,** 138–149 (2008).
102. Nguyen, D. P. & Lin, S. A frontal cortex event-related potential driven by the basal forebrain. *Elife* **2014,** 1–17 (2014).
103. Kim, T. *et al.* Cortically projecting basal forebrain parvalbumin neurons regulate cortical gamma band oscillations. *Proc. Natl. Acad. Sci.* **112,** E2848–E2848 (2015).
104. Callaway, E. M. & Luo, L. Monosynaptic Circuit Tracing with Glycoprotein-Deleted Rabies Viruses. *J. Neurosci.* **35,** 8979–8985 (2015).
105. Huang, Z. J. & Zeng, H. Genetic Approaches to Neural Circuits in the Mouse. *Annu. Rev. Neurosci* **36,** 183–215 (2013).
106. Oh, S. W. *et al.* A mesoscale connectome of the mouse brain. *Nature* **508,** 207–214 (2014).
107. Osten, P. & Margrie, T. W. Mapping brain circuitry with a light microscope. *Nat. Methods* **10,** 515–23 (2013).
108. Miyamichi, K. *et al.* Cortical representations of olfactory input by trans-synaptic tracing. *Nature* **472,** 191–196 (2011).
109. Wall, N. R., De La Parra, M., Callaway, E. M. & Kreitzer, A. C. Differential innervation of direct- and indirect-pathway striatal projection neurons. *Neuron* **79,** 347–360 (2013).
110. Watabe-Uchida, M., Zhu, L., Ogawa, S. K., Vamanrao, A. & Uchida, N. Whole-brain mapping of direct inputs to midbrain dopamine neurons. *Neuron* **74,** 858–73 (2012).
111. Wickersham, I. R. *et al.* Monosynaptic restriction of transsynaptic tracing from single, genetically targeted neurons. *Neuron* **53,** 639–647 (2007).
112. Beier, K. T. *et al.* Circuit Architecture of Midbrain Dopamine Neurons Revealed by Systematic Input – Output Mapping. *Cell* 622–634 (2015).
113. Miyamichi, K. *et al.* Dissecting local circuits: parvalbumin interneurons underlie broad feedback control of olfactory bulb output. *Neuron* **80,** 1232–1245 (2013).
114. Ogawa, S. K., Cohen, J. Y., Hwang, D., Uchida, N. & Watabe-Uchida, M. Organization of monosynaptic inputs to the serotonin and dopamine neuromodulatory systems. *Cell Rep.* **8,** 1105–1118 (2014).
115. Pollak Dorocic, I. *et al.* A Whole-Brain Atlas of Inputs to Serotonergic Neurons of the Dorsal and Median Raphe Nuclei. *Neuron* **83,** 663–678 (2014).
116. Miyamichi, K. *et al.* Cortical representations of olfactory input by trans-synaptic tracing. *Nature* **472,** 191–6 (2011).
117. DeNardo, L. A., Berns, D. S., DeLoach, K. & Luo, L. Connectivity of mouse somatosensory and prefrontal cortex examined with trans-synaptic tracing. *Nat. Neurosci.* **84,** 778–789 (2015).
118. Cullinan, W. E. & Zaborszky, L. Organization of ascending hypothalamic projections to the rostral forebrain with special reference to the innervation of cholinergic projection neurons. *J Comp Neurol* **306,** 631–667 (1991).
119. Hikosaka, O. The habenula: from stress evasion to value-based decision-making. *Nat. Rev. Neurosci.* **11,** 503–513 (2010).
120. Zaborszky, L., Gaykema, R. P., Swanson, D. J. & Cullinan, W. E. Cortical input to the basal forebrain. *Neuroscience* **79,** 1051–1078 (1997).
121. Sarter, M., Givens, B. & Bruno, J. P. The cognitive neuroscience of sustained attention: Where top-down meets bottom-up. *Brain Res. Rev.* **35,** 146–160 (2001).

122. Zepelin, H., Siegel, J. M. & Tobler, I. Mammalian sleep. *Princ. Pract. sleep Med.* 91–100 (2005).
123. Sastre, J. P., Buda, C., Kitahama, K. & Jouvet, M. Importance of the ventrolateral region of the periaqueductal gray and adjacent tegmentum in the control of paradoxical sleep as studied by muscimol microinjections in the cat. *Neuroscience* **74,** 415–26 (1996).
124. Vanini, G., Torterolo, P., McGregor, R., Chase, M. H. & Morales, F. R. GABAergic processes in the mesencephalic tegmentum modulate the occurrence of active (rapid eye movement) sleep in guinea pigs. *Neuroscience* **145,** 1157–1167 (2007).
125. Crochet, S., Onoe, H. & Sakai, K. A potent non-monoaminergic paradoxical sleep inhibitory system: a reverse microdialysis and single-unit recording study. *Eur. J. Neurosci.* **24,** 1404–1412 (2006).
126. Petitjean, F., Sakai, K., Blondaux, C. & Jouvet, M. Hypersomnia by isthmic lesion in cat. II. Neurophysiological and pharmacological study. *Brain Res.* **88,** 439–53 (1975).
127. Kaur, S. *et al.* Hypocretin-2 Saporin Lesions of the Ventrolateral Periaquaductal Gray (vlPAG) Increase REM Sleep in Hypocretin Knockout Mice. *PLoS One* **4,** e6346 (2009).
128. Clément, O., Sapin, E., Bérod, A., Fort, P. & Luppi, P.-H. Evidence that neurons of the sublaterodorsal tegmental nucleus triggering paradoxical (REM) sleep are glutamatergic. *Sleep* **34,** 419–23 (2011).
129. Garcia, S. V. *et al.* Genetic inactivation of glutamate neurons in the rat sublaterodorsal tegmental nucleus recapitulates REM sleep behaviour disorder. *BRAIN* **140,** 414–428 (2017).
130. Yang, C. F. *et al.* Sexually Dimorphic Neurons in the Ventromedial Hypothalamus Govern Mating in Both Sexes and Aggression in Males. *Cell* **153,** 896–909 (2013).
131. Thankachan, S., Kaur, S. & Shiromani, P. J. Activity of Pontine Neurons during Sleep and Cataplexy in Hypocretin Knock-Out Mice. *J. Neurosci.* **29,** 1580–1585 (2009).
132. Thakkar, M. M., Strecker, R. E. & McCarley, R. W. Phasic but not tonic REM-selective discharge of periaqueductal gray neurons in freely behaving animals: relevance to postulates of GABAergic inhibition of monoaminergic neurons. *Brain Res.* **945,** 276–80 (2002).
133. Anikeeva, P. *et al.* Optetrode: a multichannel readout for optogenetic control in freely moving mice. *Nat. Neurosci.* **15,** (2011).
134. Chen, T.-W. *et al.* Ultrasensitive fluorescent proteins for imaging neuronal activity. *Nature* **499,** 295–302 (2013).
135. Ghosh, K. K. *et al.* Miniaturized integration of a fluorescence microscope. *Nat. Methods* **8,** 871–878 (2011).
136. Benington, J. H. & Heller, H. C. Does the function of REM sleep concern non-REM sleep or waking? *Prog. Neurobiol.* **44,** 433–449 (1994).
137. Benington, J. H. & Heller, H. C. REM-sleep timing is controlled homeostatically by accumulation of REM-sleep propensity in non-REM sleep. *Am. J. Physiol.* **266,** R1992-2000 (1994).
138. Hassani, O. K., Lee, M. G. & Jones, B. E. Melanin-concentrating hormone neurons discharge in a reciprocal manner to orexin neurons across the sleep-wake cycle. *Proc. Natl. Acad. Sci. U. S. A.* **106,** 2418–22 (2009).
139. RW McCarley, J. H. Neuronal Excitability Modulation over the Sleep Cycle : A Structural and Mathematical Model. *Science* **189,** 58–60 (1975).
140. Clement, O. *et al.* The Lateral Hypothalamic Area Controls Paradoxical (REM) Sleep by

Means of Descending Projections to Brainstem GABAergic Neurons. *J. Neurosci.* **32,** 16763–16774 (2012).
141. Diniz Behn, C. G., Ananthasubramaniam, A. & Booth, V. Contrasting Existence and Robustness of REM/Non-REM Cycling in Physiologically Based Models of REM Sleep Regulatory Networks. *SIAM J. Appl. Dyn. Syst.* **12,** 279–314 (2013).
142. Dunmyre, J. R., Mashour, G. A. & Booth, V. Coupled flip-flop model for REM sleep regulation in the rat. *PLoS One* **9,** (2014).
143. Franken, P. Long-term vs. short-term processes regulating REM sleep. *J. Sleep Res.* **11,** 17–28 (2002).
144. Mallick, B. N., Siegel, J. M. & Fahringer, H. Changes in pontine unit activity with REM sleep deprivation. *Brain Res.* **515,** 94–98 (1990).
145. Barnes, A. K., Koul-Tiwari, R., Garner, J. M., Geist, P. A. & Datta, S. Activation of brain-derived neurotrophic factor-tropomyosin receptor kinase B signaling in the pedunculopontine tegmental nucleus: a novel mechanism for the homeostatic regulation of rapid eye movement sleep. *J. Neurochem.* **141,** 111–123 (2017).
146. Datta, S., Knapp, C. M., Koul-Tiwari, R. & Barnes, A. The homeostatic regulation of REM sleep: A role for localized expression of brain-derived neurotrophic factor in the brainstem. *Behav. Brain Res.* **292,** 381–92 (2015).
147. Kvitsiani, D. *et al.* Distinct behavioural and network correlates of two interneuron types in prefrontal cortex. *Nature* **498,** 363–366 (2013).
148. Ziv, Y. *et al.* Long-term dynamics of CA1 hippocampal place codes. *Nat. Neurosci.* **16,** 264–6 (2013).